FLOW BEHAVIOR OF GAS-CONDENSATE WELLS

A DISSERTATION
SUBMITTED TO THE DEPARTMENT OF ENERGY
RESOURCES ENGINEERING
AND THE COMMITTEE ON GRADUATE STUDIES
OF STANFORD UNIVERSITY
IN PARTIAL FULFILLMENT OF THE REQUIREMENTS
FOR THE DEGREE OF
DOCTOR OF PHILOSOPHY

Chunmei Shi

March 2009

I certify that I have read this dissertation and that, in my opinion, it is fully adequate in scope and quality as a dissertation for the degree of Doctor of Philosophy.

_____

(Roland N. Horne)　　Principal Adviser

I certify that I have read this dissertation and that, in my opinion, it is fully adequate in scope and quality as a dissertation for the degree of Doctor of Philosophy.

_____

(Anthony R. Kovscek)

I certify that I have read this dissertation and that, in my opinion, it is fully adequate in scope and quality as a dissertation for the degree of Doctor of Philosophy.

_____

(Franklin M. Orr, Jr.)

Approved for the University Committee on Graduate Studies.

Abstract

The objective of this work was to develop a methodology to increase the productivity of gas/condensate from gas-condensate reservoirs. Presently, gas-condensate reservoirs experience reductions in productivity by as much as a factor of 10 due to the dropout of liquid close to the wellbore. The liquid dropout blocks the flow of gas to the well and lowers the overall energy output by a very substantial degree. The combination of condensate phase behavior and rock relative permeability results in a composition change of the reservoir fluid, as heavier components separate into the dropped-out liquid while the flowing gas phase becomes lighter in composition. This effect has been sparsely recognized in the literature, although there is clear evidence of it in field observations. This work quantified the effect, developed a scientific understanding of the phenomena, and used the results to investigate ways to enhance the productivity by controlling the liquid composition that drops out close to the well. By optimizing the producing pressure strategy, it should be possible to cause a lighter liquid to be condensed in the reservoir, after which the productivity loss would be more easily remedied. The research made use of experimental measurements of gas-condensate flow, as well as compositional numerical simulations. Different strategies have been compared, and the optimum producing sequences are suggested for maximum condensate recovery. Results show that composition varies significantly as a function of fluid phase behavior and producing sequence; condensate recovery can be improved with proper producing strategy, and productivity loss can be reduced by changing the producing sequence. This study can be used to determine the optimum producing strategy when the well is brought into production and reduce the productivity loss caused by the condensate banking effect.

Acknowledgements

During the last six and a half years, I have been assisted by many people. Most credit is due to my advisor, Professor Roland N. Horne, for his patience, encouragement and guidance throughout my research. All this work would not have come to fruition had it not been for his support.

My sincere thanks are also extended to Professor Franklin M. Orr and Professor Anthony R. Kovscek for reading my dissertation, providing valuable comments, and serving on my defense committee. Many thanks to Professor Jennifer Wilcox for being a member of my examination committee.

A large portion of this work has depended on the extensive use of Gas Chromatography from SUPRI-C laboratory and the financial aid of SUPRI-D Affiliates, Saudi Aramco and RPSEA are appreciated.

I would also like to thank Dr. Tom Tang and Qing Chen for various helpful discussions I have had with each of them.

To my parents, Yufang Zhou and Zhenghuang Shi, for their love and support. Especially my mother, she is such a great one. Although she did not receive any formal education, and could not read and write, she encouraged me to leave our small village to get better formal education. I thank my brother, ZhiYong Shi, for taking part of my responsibility to take care of our parents while I was far away and for making me realize other important things in life. Their unconditional support and love have guided me through each and every step along the way.

I am especially thankful to my husband Yulin Jin who has been a colleague for two years, and is a constant source for help and great ideas. He is always closest to my joys and sorrows and always standing by me.

Contents

List of Tables

List of Figures

xviii

Chapter 1

Introduction

Gas-condensate reservoirs represent an important source of hydrocarbon reserves and have long been recognized as a reservoir type, possessing the most intricate flow and complex thermodynamic behaviors. Gas-condensate reservoirs are characterized by producing both gas and condensate liquid at surface. Typical retrograde condensate reservoirs produce gas/liquid ratios of approximately 3-150 MCF/STB (McCain, 1990), or condensate surface yields ranging from 7 to 333 $STB/MMCF$. The added economic value of produced condensate liquid, in addition to gas production, makes the recovery of condensate a key consideration in the development of gas-condensate reservoirs.

The phase diagram of a gas-condensate system has a critical temperature less than the reservoir temperature and a cricondentherm greater than the reservoir temperature (see Figure 1.1). The gas-condensate reservoir is initially gas at the reservoir condition, point 1, and as the reservoir pressure decreases below the dewpoint, point 2, liquid condenses from gas and forms a "ring" or "bank" around the producing well in the near-well region. Normally this liquid will not flow until the accumulated condensate saturation exceeds the critical condensate saturation (S_{cc}) due to the relative permeability and capillary pressure effects in the porous medium. Once the reservoir pressure drops below the dewpoint, a pressure-drop occurs during production which tends to form condensate banking (also known as the condensate blockage effect) around the well. This causes a loss in productivity. As the reservoir pressure further
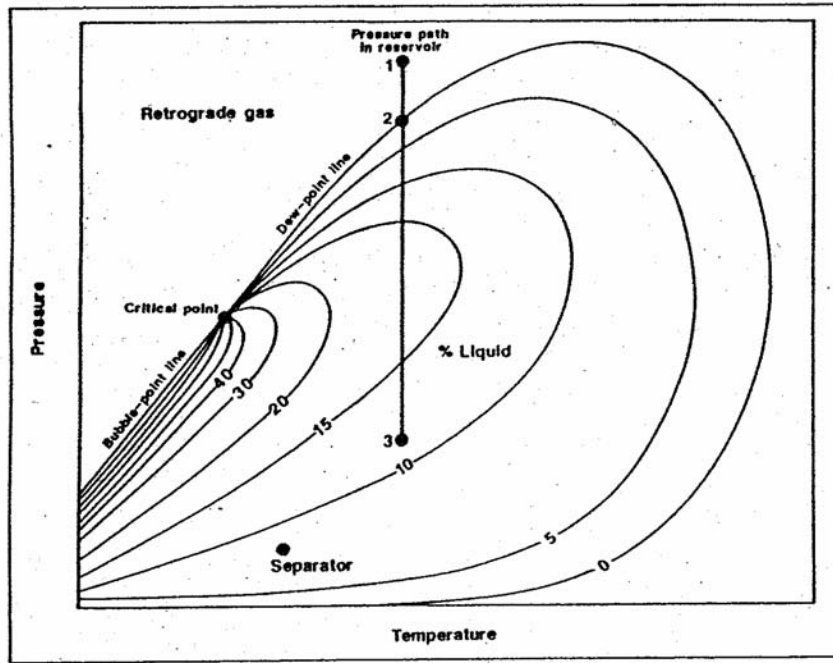
Figure 1.1: Phase diagram of a typical retrograde (McCain, 1990).

draws down to lower pressure, point 3, the liquid begins to revaporize in a PVT cell experiment. However, the revaporization may not take place in the reservoir because the overall composition of the reservoir fluid changed during production. As a consequence of the composition variation, the total concentration of the heavy component in the reservoir fluid will be higher than that of the original reservoir fluid. This leads to the recovery problem associated with the heavier components, which are usually not easy to recover once stuck in the reservoir.

Condensate blockage near the well may cause a significant loss in well productivity for low-to-moderate permeability high-yield condensate reservoirs since the main source for pressure loss in the tight reservoir depends primarily on reservoir permeability. Several other factors, including initial productivity, amount of near wellbore liquid saturation due to condensation, phase behavior of well block fluid and how the well is being produced (different producing pressure schemes) appear to influence the observed level of productivity decline. A better understanding of how the condensate accumulation influences the productivity and the composition configuration in the

liquid phase is very important to optimize the producing strategy for gas-condensate reservoirs, to reduce the impact of condensate banking, and to improve the ultimate gas and condensate recovery.

1.1 Problem Statement

This research studied the well deliverability (productivity) issue associated with condensate blockage effect with an emphasis on flow behavior analysis. Although extensive research and development have been performed in this general area, there still exist many important and outstanding issues. Specifically, this work focused on the following aspects:

- Composition variation. The objective of this work was to study how the compositions of heavy components of a gas condensate system change with time around production wells during depletion, and how the rate of the composition variation influences the fluid thermodynamic properties, and hence, defines the dynamic phase diagram of the fluid in the reservoir. It should be noted that the extent or even the existence of compositional changes has been noted in the literature rather infrequently, which is an indication that the importance of this phenomenon has not been fully recognized.

- Dynamic condensate saturation build-up. Due to compositional variation and relative permeability constraints, the condensate saturation build-up is a dynamic process and varies as a function of time, place (distance to wellbore) and phase behavior. In this work, we conducted CT experiments to investigate how the liquid accumulates and distributes in a core.

- Producing schemes. Different producing strategies may impact the composition configuration for both flowing and static phases and the amount of the liquid trapped in the reservoir, which in turn may influence the well productivity and hence the ultimate gas and liquid recovery from the reservoir. Changing the manner in which the well is brought into flowing condition can affect the liquid

dropout composition and can therefore change the degree of productivity loss. In this study, we conducted parametric studies to identify the most influential reservoir and fluid characteristics in the establishment of optimum gas production and condensate recovery for the exploitation of gas-condensate reservoirs.

1.2 Dissertation Outline

This dissertation proceeds as follows. Chapter 2 presents a literature review on condensate blockage effect around the well and the associated impairment in gas productivity and condensate recovery. The chapter includes advantages and limitations of existing techniques and some outstanding issues are discussed.

Chapter 3 describes a core flooding experiment with two-component synthetic gas-condensate, designed and constructed to model gas-condensate production behavior from pressure above the dew-point to below. This experimental equipment was constructed to allow detailed and accurate measurements of real time pressure and in situ composition of the flowing fluid along the core.

Experimental observations are discussed in Chapter 4. Five example experiments on the binary gas-condensate system demonstrate and confirm the compositional variation in the gas-condensate flow, even in the constant pressure-drop flow case.

In the first part of Chapter 5, a general form of material balance equation for condensate flow in porous media was developed for both one-dimensional linear flow and three-dimensional radial flow of two-phase gas-condensate fluid through porous media, with the effect of interfacial tension. The compositional variation of the reservoir fluid, especially the heavier component of the fluid, around the well during condensate dropout was analyzed. Key parameters that influence the compositional behavior were also discussed in detail. The theoretical models provide tools to better understand the momentary compositional variation in the reservoir. In the second part of this chapter, compositional simulations of binary-component and multicomponent gas-condensate fluids were designed and conducted at field scale to investigate the composition and condensate saturation variations. Different producing strategies

were tested to fathom the optimum producing sequences for maximum gas and condensate recovery. By taking into account the new understanding of the impact of compositional changes, the composition of the liquid dropout can be "controlled" by the production strategy (for example by dropping a lighter liquid in preference to a heavier one). Hence the recovery from gas reservoirs, especially tight ones, with condensate fluids can be improved.

Chapter 6 summarizes the results of this work and provides some insight into possible future research in experimental study for gas-condensate flow.

Chapter 2

Concepts and Literature Review

The flow behavior of a gas-condensate system depends on both the phase envelope of the fluid and the conditions of the reservoir (such as pressure, temperature and rock properties etc.). Due to compositional variation and relative permeability constraints, the build-up of condensate saturation around the well is a dynamic process and varies as a function of time, place (distance to wellbore) and phase behavior. In this chapter, we explore several key concepts about the flow behavior of the gas-condensate system and define the prospective issues for this study. Previous research on these issues will be reviewed.

2.1 Flow Behavior of Gas-Condensate Systems

To analyze the flow behavior of a gas-condensate system, we first need to understand the difference between the values of static and flowing properties. The static values are for in-situ fluid properties defined at a specific reservoir location at a given time, while the flowing values are associated with the properties of the flowing fluids. In reservoir simulations static values will refer to the property values of a given grid block at a given time, while in laboratory experiments and field sampling cases, the sample collected at the wellhead only comes from the flowing phase. Hence, compositions of the wellhead samples will not be the same as the overall compositions in the reservoir or the static values in reservoir simulations, although they can indicate the changes

of flow property variations in the reservoir.

2.1.1   Constant Volume Depletion (CVD) and Constant Composition Expansion (CCE)

Gas-condensate fluid is investigated primarily using Constant Composition (Mass) Expansion (CCE/CME) to obtain the dewpoint and Constant Volume Depletion (CVD) to simulate reservoir production behavior. CCE is also called flash vaporization and is simulated by expansion of a mixture with a fixed composition (z_i) in a series of pressure steps. During the CCE experiment, no gas or liquid is removed from the cell, and at each step, the pressure and total volume of the reservoir fluid (oil and gas) are measured. As the name CCE implies, the reservoir fluid composition does not change during the production process. However,in a reservoir the heavier component drops out to the reservoir during production as condensation develops in the reservoir and this will definitely alter the configuration of the fluid composition in the reservoir.

In the CVD procedure (as shown in Figure 2.1), the sample of reservoir liquid in the laboratory cell is brought to the dewpoint pressure, and the temperature is set to the reservoir temperature. Pressure is reduced by increasing the cell volume. Part of the gas is expelled from the cell until the volume of the cell equals the volume at the dewpoint. The process is repeated for several pressure steps and the liquid volume at each pressure(V_T^L) is recorded and liquid dropout(V_T^L/V_T^{dew}) is calculated. The CVD experiment is a good representation of the reservoir depletion only if the condensate phase is totally immobile, which is not true if condensate saturation exceeds the critical condensate saturation (S_{CC}) and part of the condensate can flow in the porous medium. At the same time, the liquid dropout estimation from the CVD experiment does not account for the condensate buildup in the reservoir; hence it cannot indicate the maximum possible condensate accumulation in the reservoir. Taking a binary system C_1/C_4 for example, the maximum liquid dropout is less than 10% from the CVD experiment (Figure 2.2), however, reservoir simulation shows that the condensate saturation can be as high as 57.5%, as will be discussed in more
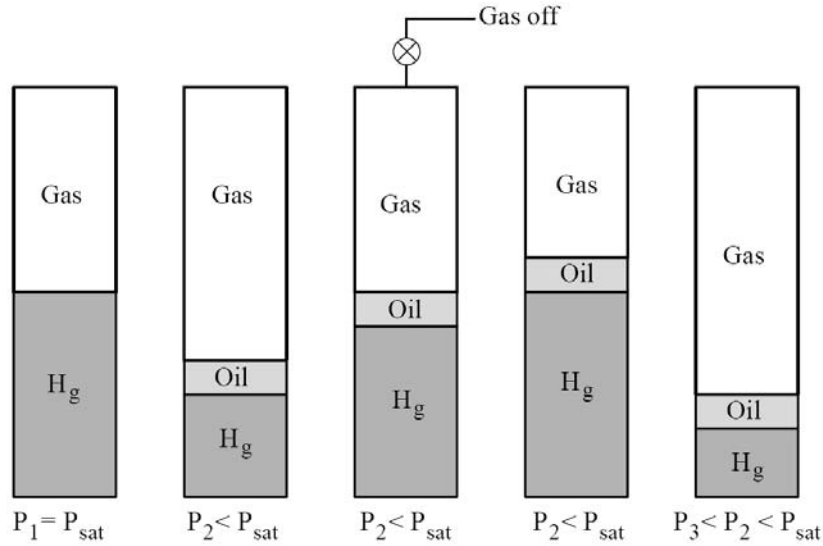
Figure 2.1: A schematic of Constant Volume Depletion (CVD) process.

detail in Chapter 3.

2.1.2 Differential Condensation (DC)

Heavier components separate into the dropped-out liquid while the flowing gas phase becomes lighter in composition. By checking the wellhead fluid sample, we can investigate how the composition change with time. Differential Condensation (DC) is a procedure assumed in this study to investigate the composition variation at the wellhead. In the DC experiment (as shown in Figure 2.3), the sample of reservoir gas in the laboratory cell is first brought to the dewpoint pressure, and the temperature is set to the reservoir temperature. Next, pressure is reduced by increasing the cell volume. Then all the liquid is expelled from the cell while pressure is held constant by reducing the cell volume. The process is repeated in steps until atmospheric pressure is reached. Liquid and vapor compositions are analyzed at each pressure step. In this procedure no condensate is mobile during production, which may underestimate the heavy component recovery at the surface since in reality part of the condensate phase can flow once the accumulated condensate saturation exceeds the critical condensate

(a) PT diagram for system $C_1/C_4 = 0.85/0.15$

(b) Liquid dropout curve at T = 60 deg F
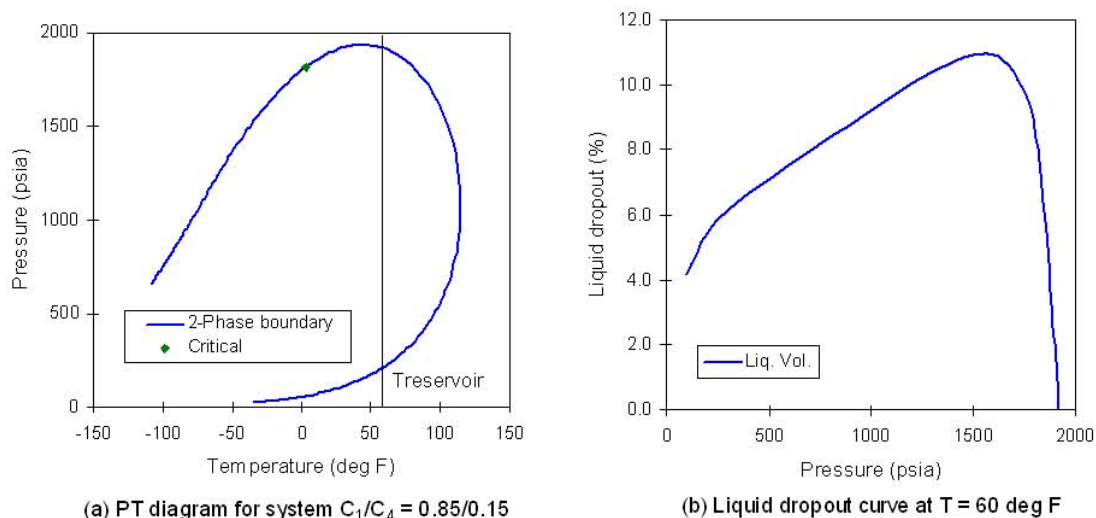
Figure 2.2: PT diagram and liquid drop curve for system $C_1/nC_4 = 0.85/0.15$.

saturation. However, this experiment can tell us how much of the heavier component would be trapped in the reservoir in the worst case. Different from CCE (or flash vaporization), the overall fluid composition in the DC procedure varies as we keep removing the liquid phase from the mixture.

Comparing the regular flash vaporization and the DC procedure (Figure 2.4), in the example fluid 0.85 C_1 and 0.15 C_4 we can find that as much as 7.6% (over 15% original) of the heavy component butane can fail to reach the surface if no condensate is brought to flow. Similarly, also about 6.4% (over 40% original) butane (Figure 2.5) can be lost from a richer gas-condensate system $C_1/nC_4 = 0.60/0.40$ (Figure 2.6). The extent of heavy component lost seems less severe in the rich gas-condensate case in this example.

Figure 2.7 shows the comparison of the DC and flash results for a rich three-component gas-condensate system, with the PT diagram and liquid drop-out curve shown in Figure 2.8. Similar to the simple binary system, both heavy component decane and intermediate component butane are lost to production in the DC procedure. In terms of liquid dropout, the richer three-component system $C_1/nC_4/C_{10} = 0.60/0.25/0.15$ has the least heavy component loss given no condensate flow in the
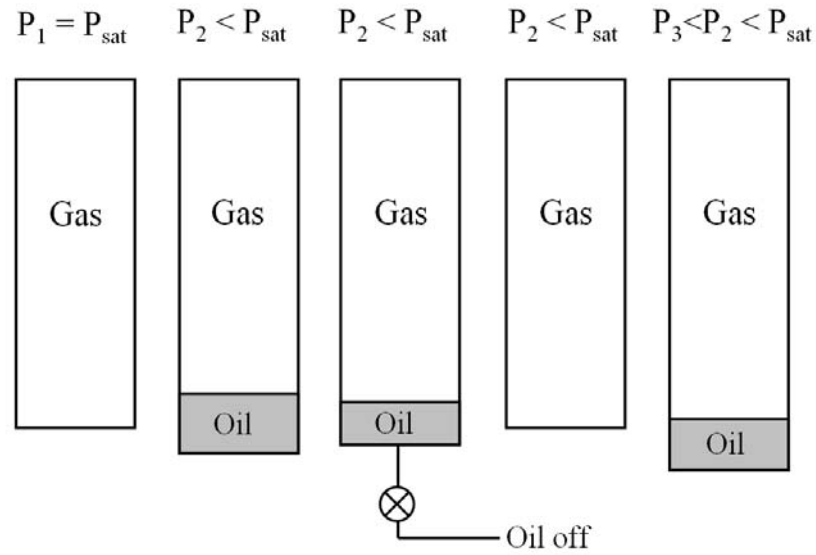
Figure 2.3: A schematic of Differential Condensation (DC) process.
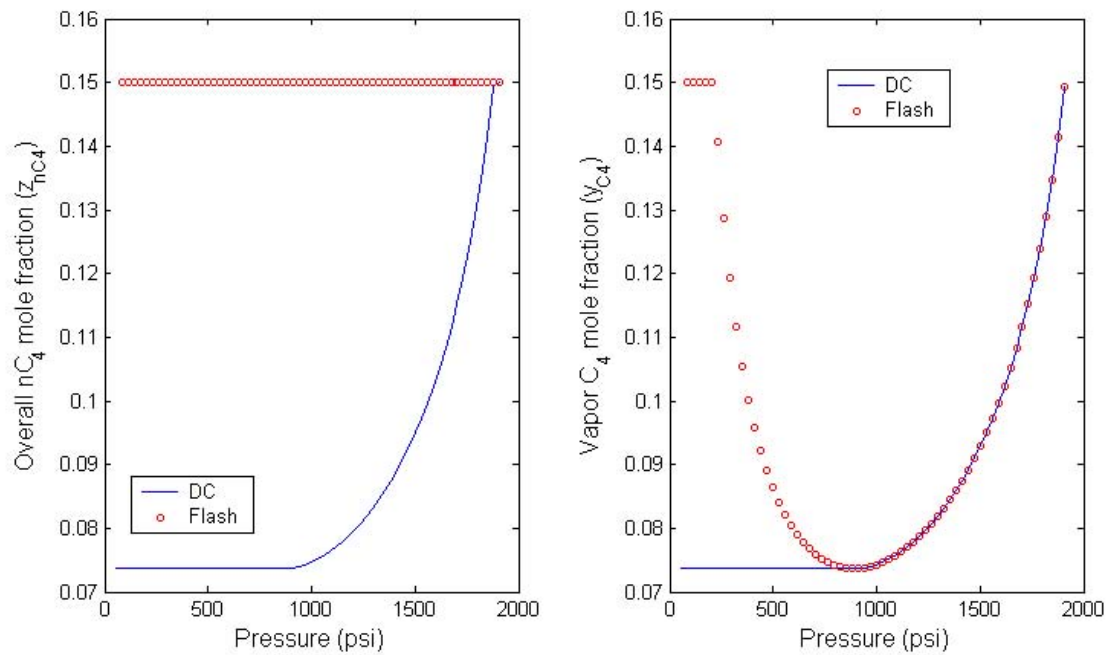
Figure 2.4: Total composition z_{nC_4} and gas composition y_{nC_4} profiles at $T = 60^o F$ for system $C_1/nC_4 = 0.85/0.15$.
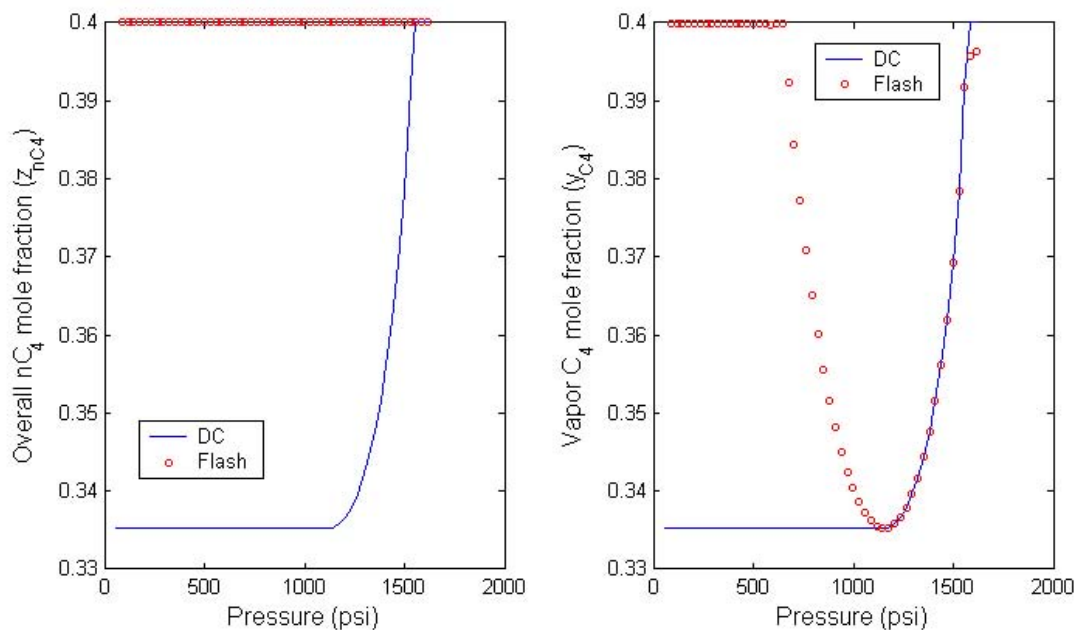
Figure 2.5: Total composition z_{nC_4} and gas composition y_{nC_4} profiles at $T = 190^oF$ for system $C_1/nC_4 = 0.60/0.40$.

(a) PT diagram for system $C_1/nC_4 = 0.60/0.40$

(b) Liquid dropout curve for system $C_1/nC_4 = 0.60/0.40$ at T = 190F
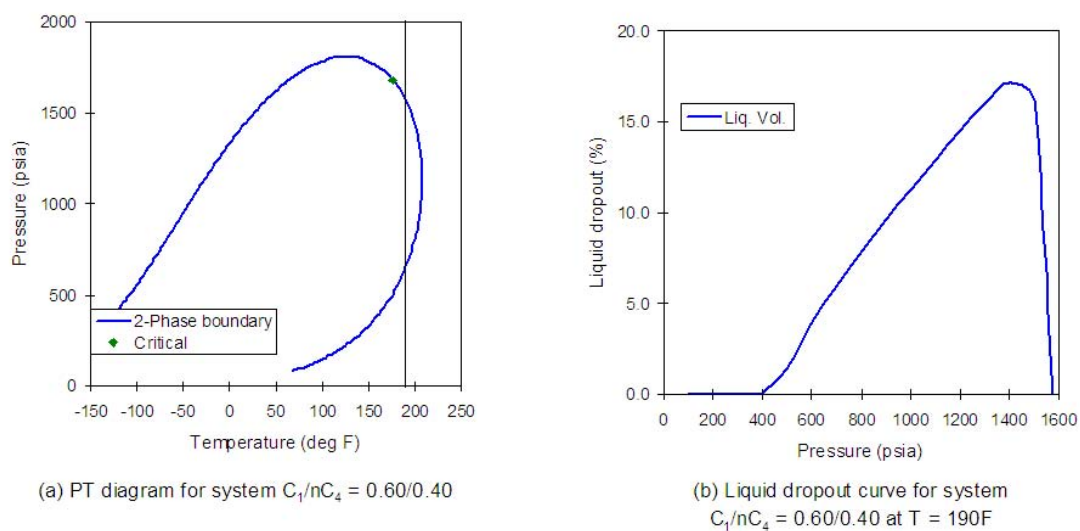
Figure 2.6: PT diagram and liquid dropout curve for system $C_1/nC_4 = 0.60/0.40$.
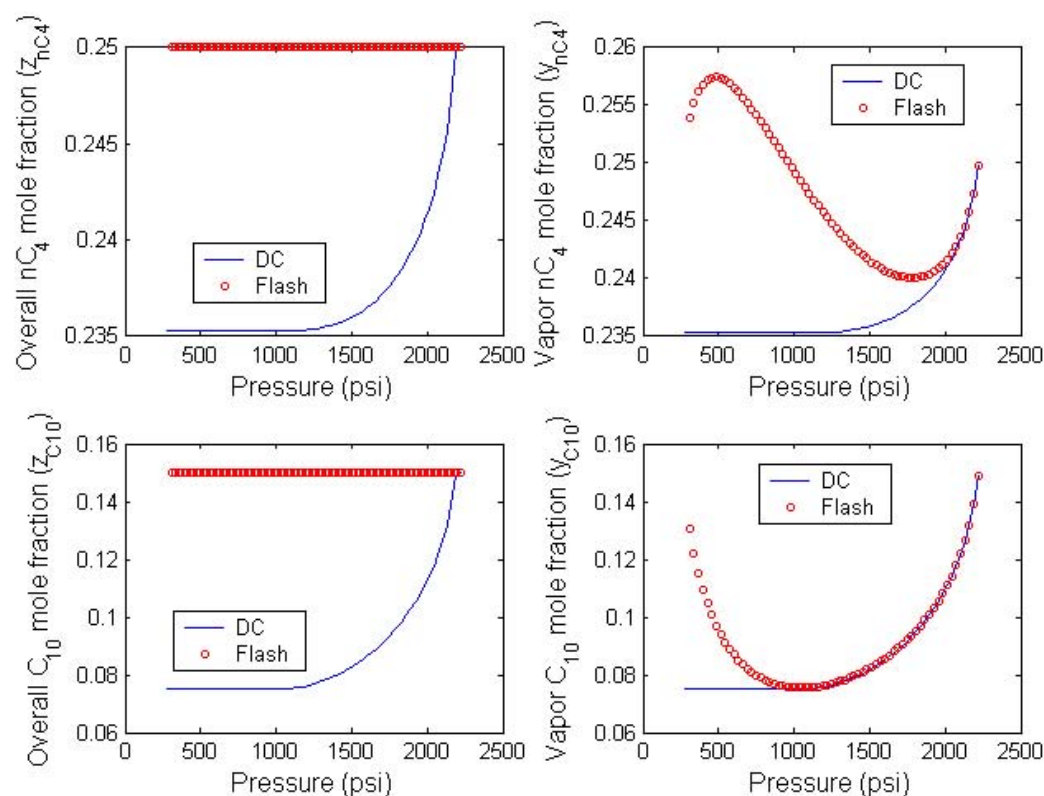
Figure 2.7: Heavy and intermediate components profiles at $T = 190^{o}F$ for system $C_1/nC_4/C_{10} = 0.60/0.25/0.15$.

reservoir.

2.1.3   Three Flow Regions

According to Fevang (1995), fluids flowing toward a producing well in a gas-condensate reservoir during depletion can be divided into three main flow regions, as shown in Figure 2.9:

- Single-phase gas region 3: A region that is far away from the well and has reservoir pressure higher than the dewpoint, and hence only contains single-phase gas.

- Condensate buildup region 2: A region where reservoir pressure drops below the

(a) PT diagram for system $C_1/nC_4/C_{10}$ = 0.60/0.25/0.15

(b) Liquid dropout curve at T = 398.93 F for system $C_1/nC_4/C_{10}$ = 0.60/0.25/0.15
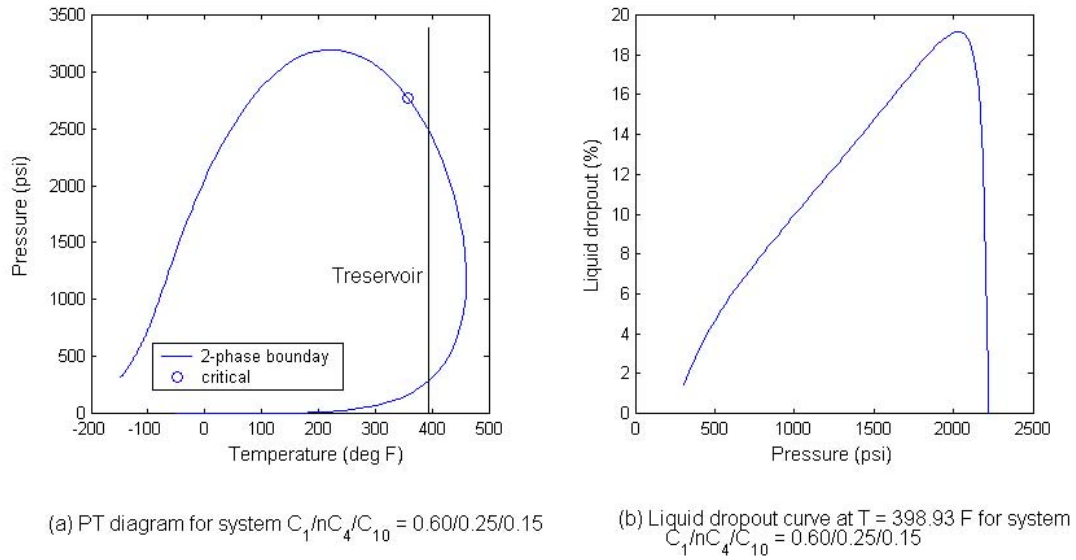
Figure 2.8: PT diagram and liquid dropout curve for system $C_1/nC_4/C_{10}$ = 0.60/0.25/0.15.
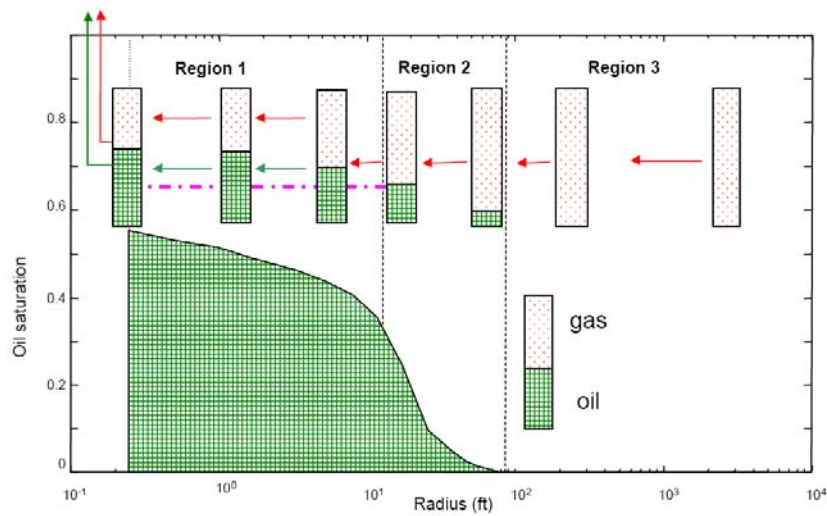
Figure 2.9: Schematic gas-condensate flow behavior in three regions (Roussennac, 2001).

dewpoint, and condensate drops out in the reservoir. However, the accumulated condensate saturation is not high enough for the liquid phase to flow. Therefore, the flowing phase in this region still contains only the single gas phase, and the flowing gas becomes leaner as the heavier component drops into the reservoir.

- Near well region 1: An inner near-well region where reservoir pressure drops further below the dewpoint, the critical condensate saturation is exceeded, and part of the condensate buildup becomes mobile. The mobility of the gas phase is greatly impaired due to the existence of the liquid phase.

Both the CVD and DC procedures assume that the accumulated condensate is totally immobile in the reservoir. However, as we can infer from Figure 2.9, the condensate buildup in region 1 can flow if the accumulated condensate in this region is sufficient to overcome the relative permeability constraint (immobile liquid saturation). The liquid-phase flow alleviates the heavy component loss at the surface to some extent, but because of the coexistence of gas and liquid phases, the gas mobility is greatly impaired. The composition of reservoir fluid becomes complex as part of the liquid participates in the flow. Figure 2.10 shows four different composition scenarios in a reservoir as reservoir pressure drops below dewpoint. Compositions 1, 2, 3 and 4 (Table 2.1) correspond to reservoir pressures p_1, p_2, p_3 and p_4 respectively. As the reservoir pressure drops, the PT diagram changes significantly from a relatively lean gas-condensate system (Composition 1), to a richer system (Composition 2) and then finally to a volatile oil system (Composition 3). The CVD experiment estimation (Figure 2.11) shows a great increase of the liquid volume percentage as the reservoir depletes. Figure 2.12 shows the vapor phase composition profile for light component C_1, intermediate component C_{4-6} and heavy component C_7^{+2} and C_7^{+3} for scenarios of different fluid configurations in the reservoir. Note that although there are dramatic changes in the PT diagram, the heavy components C_7^{+2} and C_7^{+3} in the vapor phase vary little as the reservoir pressure drops below 2200 psi.
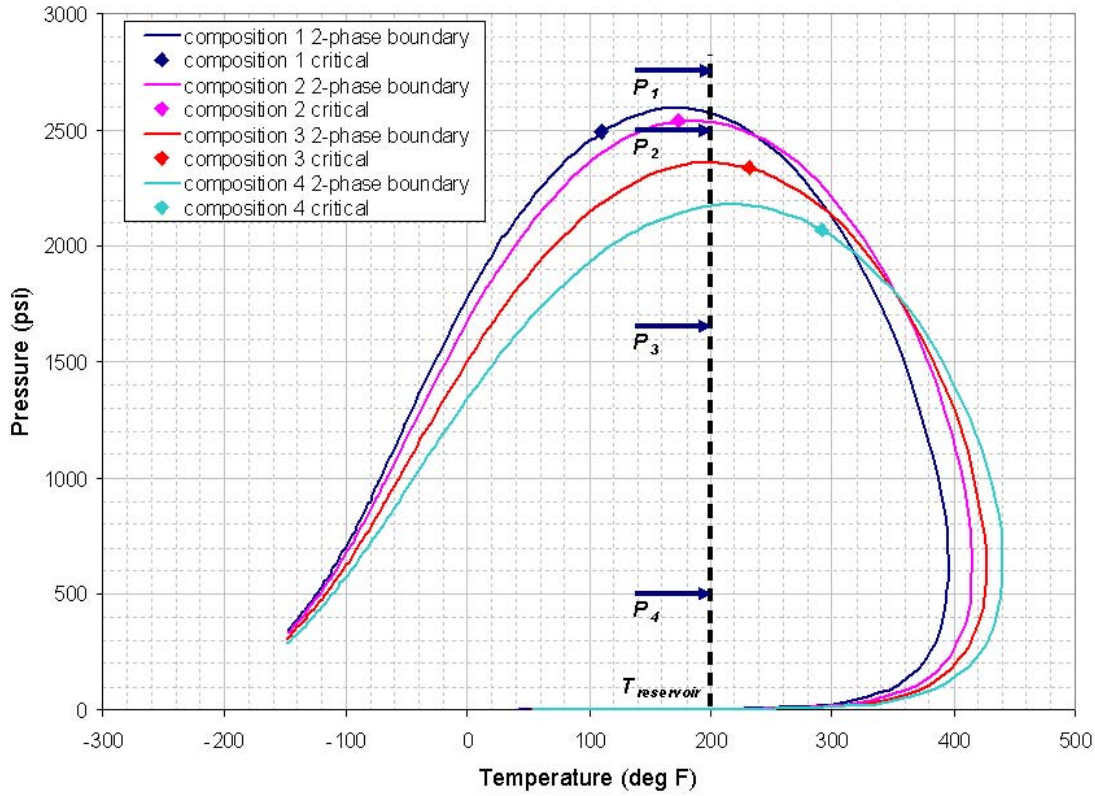
Figure 2.10: PT diagrams for four gas-condensate systems.

2.2   Literature Review

In this section, we review previous work on the issue of condensate buildup, since it is the primary factor causing the decrease in the relative permeabilities and thus reducing the well-deliverability in gas-condensate reservoirs. Factors controlling condensate blockage can be classified in different ways. As will be discussed later, among many contributing parameters, the phase behavior, the relative permeability and the well producing scheme are three of the most important aspects for both understanding the dynamic condensate banking and developing the optimum strategies for the recovery of both gas and condensate. We therefore present this literature review primarily based on these three factors.

Table 2.1: Four gas-condensate systems with different compositions.

Component	Composition 1	Composition 2	Composition 3	Composition 4
N_2	1.210	1.174	1.103	0.977
CO_2	1.940	1.752	1.558	1.438
C_1	65.990	61.577	56.161	50.645
C_2	8.690	8.694	8.511	7.598
C_3	5.910	6.217	6.534	6.130
C_{4-6}	9.670	11.228	13.385	14.804
C_7^{+1}	4.745	6.306	8.628	12.370
C_7^{+2}	1.515	2.588	3.556	5.339
C_7^{+3}	0.330	0.463	0.565	0.698
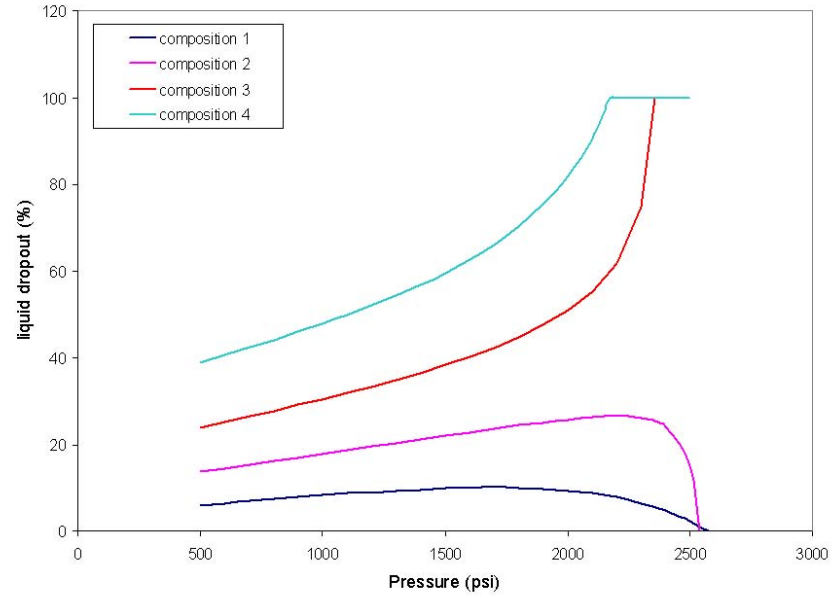
Figure 2.11: Liquid dropout curves for four gas-condensate systems at $T = 200^o F$.
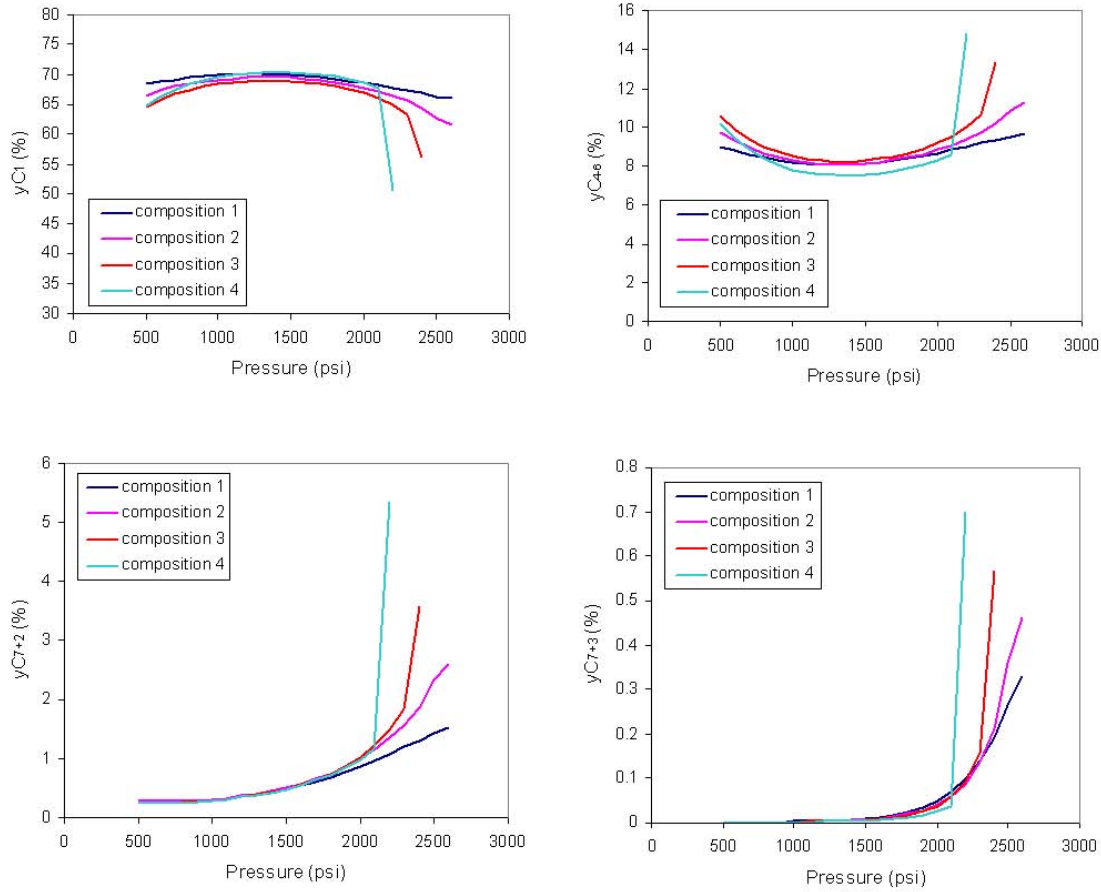
Figure 2.12: Vapor composition y_{C_1}, $y_{C_{4-6}}$, $y_{C_7^{+2}}$ and $y_{C_7^{+3}}$ for four gas-condensate systems at $T = 200^o F$.

The effect of condensate blocking on well productivity is a broad and active research area that has attracted many researchers, including Fussell (1973), Hinchman and Barree (1985), Aziz (1985), Clark (1985) and Vo *et al.* (1989). The productivity loss caused by condensate buildup is striking. According to Whitson (2005), in some cases, the decline can be as high as a factor of 30. Several examples of severe productivity decline are available in the literature such as Engineer (1985), Duggan (1972), Allen and Roe (1950), Abel *et al.* (1970) and Afidick *et al.* (1994) etc. Even in very lean gas-condensate reservoirs with a maximum liquid dropout of only 1%, the
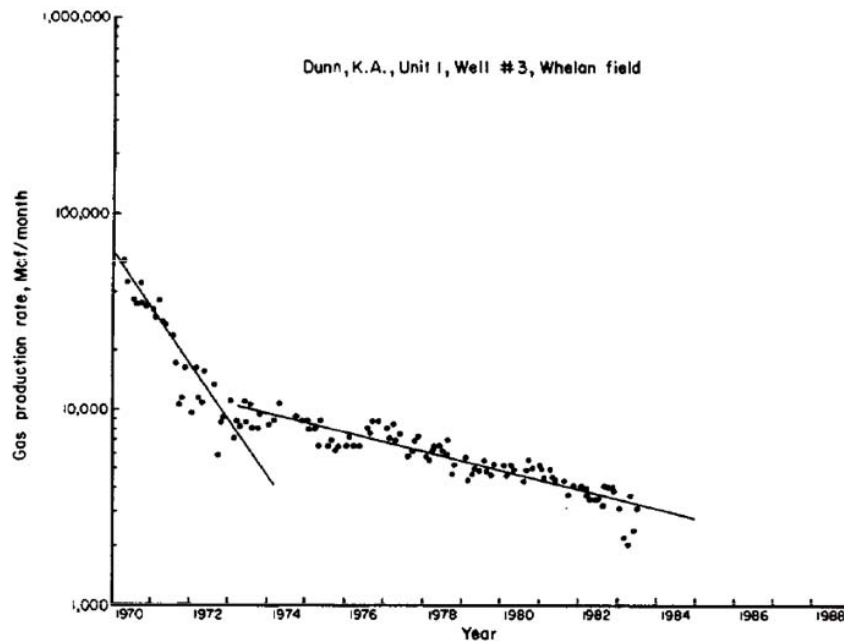
Figure 2.13: A typical production decline curve in the Whelan field (Lin and Finley, 1985).

productivity may be reduced by a factor of about two as the pressure drops below the dewpoint pressure (Fevang and Whitson, 1996). Barnum *et al.* (1995) reviewed data from 17 fields, conducted a survey on field examples from Exxon and other published industrial cases, and concluded that a severe drop in gas recovery occurs primarily in low productivity reservoirs with a permeability-thickness below 1000 $md - ft$. In a tight gas reservoir, Figure 2.13 shows the typical production decline line curve in the Whelan field (Lin and Finley, 1985), which has an average permeability of 0.153md and 70 percent of the producing wells have permeabilities less than 0.1md. The gas productivity of this tight gas field is reduced by a factor of about 10. In contrast, there are no reported examples of severe decline from high productivity formations. Similarly, most wells producing from gas caps below the saturation pressures do not experience significant declines, perhaps because of the relatively low liquid content of the gas in most associated gas caps.

It has been recognized in the literature that the relative permeability does impact the degree of productivity loss below the dewpoint. Hinchman and Barree (1985)

showed how the choice between the imbibition and the drainage relative permeability curves used in the numerical reservoir simulations could dramatically alter the productivity forecast for gas-condensate reservoirs below the dewpoint pressure.

Fevang and Whitson (1996) addressed the well deliverability problem in their gas-condensate modeling, in which they observed that the impairment of the well deliverability resulting from the near well-bore condensate blockage effect depends on the phase behavior, absolute and relative permeabilities, and how the well is being produced. According to Fevang and Whitson (1996), the well deliverability impairment resulting from the near well-bore condensate blockage depends on the relative permeability, especially for gas and oil relative permeability ratios (k_{rg}/k_{ro}) ranging from 0.05 to 0.3. In their well deliverability calculations, Fevang and Whitson (1996) approximated the condensate saturation in Region 2 with the liquid dropout curve from a CVD experiment. This approximation, however, did not account for the condensate accumulation and the variations of the overall compositions in the reservoir caused by the liquid build-up, hence it can not accurately estimate the well deliverability for the condensate blockage effect.

Unfortunately, at this time we do not have a demonstrated capability in the industry to measure the relative permeabilities at reservoir conditions for gas-condensate systems. Most of the available work has concentrated on the measurement of the endpoints of the relative permeability curves. A variety of laboratory work is still underway in both academia and the industry to try to understand the nature of the relative permeability relationships for gas-condensate systems.

Variations of the fluid flow properties at the time of discovery have also been observed and discussed for many reservoirs around the world (examples include Riemens and de Jong (1985) for Middle Eastern reservoirs and Schulte (1980) for North Sea reservoirs). Lee (1989) also presented an example to show the variation of the composition and the saturation of a gas-condensate system due to the influences of the capillary and gravitational forces. The composition change has also been observed in the field (Yuan *et al.*, 2003). Table 2.2 shows fluid samples for Well $K401$ and Well $K233$, from the Kekeya gas field in China. These two wells are from the same reservoir and close in location. Three fluid samples were collected in this reservoir: one

Table 2.2: Component composition variations for a Chinese field. (Yuan *et al.*, 2003)

Compononent	Well $K401$ @ initial reservoir condition (mol%)	Well $K233(mol\%)$ Year 1995	Well $K233(mol\%)$ Year 1999
$C_1 + N_2$	77.280	83.86	86.08
C_2	7.935	7.78	9.30
C_3	3.126	2.38	2.60
C_4	2.505	1.52	0.65
C_{5+}	8.909	4.40	1.31

from well $K401$, showing the initial reservoir condition, and the other two from Well $K233$, collected four years apart. We can see clearly that as the reservoir pressure drops, the produced fluid become leaner and leaner. Two other observations from the same field are shown in Figure 2.14. Before the gas cycling, the fluid samples from both wells grow leaner in heavy components. Furthermore, because the flowing fluid becomes lighter, the liquid trapped in the reservoir ends up being richer in the heavy components and therefore the blockage is more difficult to remedy because it will not revaporize.

Roussennac (2001) illustrated the compositional change during the depletion in his numerical simulation. According to Roussennac (2001), during the drawdown period, the overall mixture close to the well becomes richer in heavy components as the liquid builds up in the well grid cell, and the fluid behavior changes from the initial gas-condensate reservoir to that of a volatile/black oil reservoir.

To characterize the condensate banking dynamics, Wheaton and Zhang (2000) presented a general theoretical model to show how the compositions of the heavy components in a gas-condensate system change with time around the production wells during depletion. According to Wheaton and Zhang's model, the rate of change in heavy component composition is higher for a rich gas-condensate system than for a lean gas-condensate system for the same reservoir, and the condensate banking problem is particularly acute for low-permeability high-yield condensate systems.
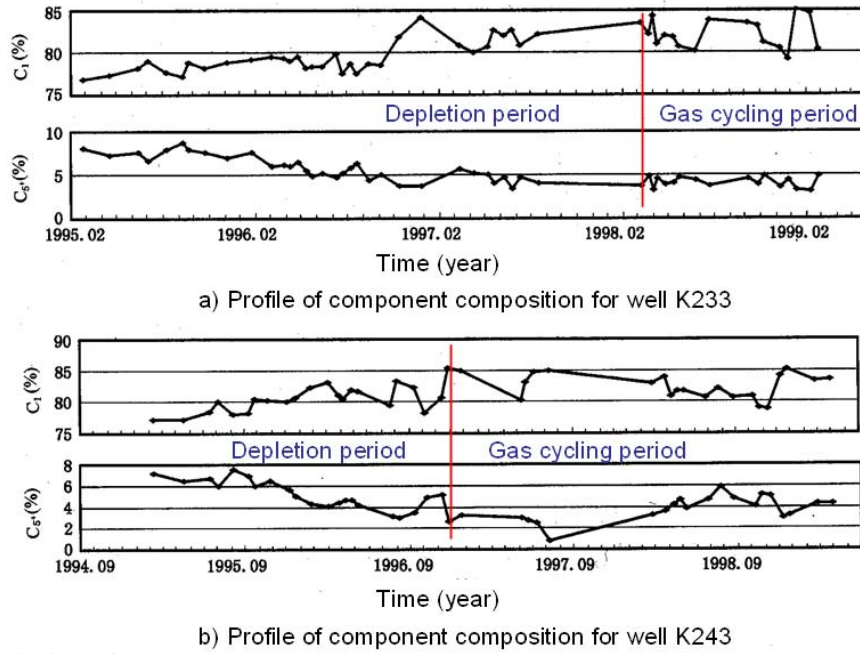
Figure 2.14: Profiles of component compositions for a Chinese field, (Yuan *et al.*, 2003).

Bengherbia and Tiab (2002) also demonstrated in their study that both the production history and the simulation prediction show an increase in lighter components in the flowing phase once the pressure drops below the dewpoint, but it is still not clear how the compositions vary with time and space and how the composition change affects the gas production and the condensate recovery.

The well producing scheme may impose significant impacts on the phase behavior. However, the manner by which the producing scheme influences the phase behavior has not yet been sufficiently addressed. Recently, the work of Ayala *et al.* (2007) shows major progress in tackling problems related to the production optimization. Ayala *et al.* (2007) conducted parametric studies with the neurosimulation technique to identify the most influential reservoir and fluid characteristics in the establishment of the optimum production strategies for a gas-condensate system. Eight different input variables investigated in their study were: permeability, porosity, drainage area, thickness, pressure ratio of p_{wf}/p_i, bottomhole pressure, initial drawdown and initial

reservoir pressure. The advantage of the artificial-neural-network (ANN) is that it provides a screening tool for a variety of gas-condensate reservoirs. With the aid of such a tool, the engineer would be able to evaluate the viability of profitable production without resorting to costly full-scale simulations. In addition, once the possibility of the profitable production has been confirmed, the expert system could be used to establish the best production scheme to be implemented for the field development.

Other parameters, such as the relative permeability and the phase behavior, are also key to the production strategy and have not yet been investigated so far; hence they need to be addressed in future parametric studies. In spite of the numerous methods proposed for measuring the relative permeability, investigating the phase behavior and optimizing the condensate recovery for gas-condensate systems, there is still no completely general approach for phase behavior analysis, especially for the effect of compositional variations on gas-condensate systems. The flowing phase behavior is influenced directly by the relative permeability and defines the condensate recovery schemes of gas-condensate systems. Accordingly, this work focused on flowing phase behavior and the impact of flowing composition changes.

Chapter 3

Experimental Investigation

In this chapter, we present our work on the experimental study of a synthetic binary gas-condensate flow in a Berea sandstone core. The core-flooding experiment is directly analogous to the flow in a reservoir. The compositional behavior during the core flow and the factors that influencing the compositional distribution are studied and discussed.

It is important to keep in mind that the experiment has been designed to simulate reservoir conditions using a synthetic gas-condensate fluid. Gas-condensate fluids from real reservoirs are much more complicated than the binary fluids used here, so the analogy here is only a simplified one. However, the apparatus is useful for indicating compositional features of a gas-condensate flow in porous media.

3.1 Experimental Design

3.1.1 Design Principles

To investigate the composition change resulting from condensation due to the pressure variation and the condensate hold-up due to relative permeability effect, we needed to select an appropriate gas-condensate mixture to conduct the core flooding experiment. In this study, we chose a binary component gas-condensate mixture based on the following principles:

- The mixture should be easy to handle in the laboratory, thus two to four components are preferred;

- The critical temperature of the mixture should be below 20 ^oC, which makes the experiment easy to perform at room temperature, and the critical pressure should be relatively low, so it can be conducted within a safe pressure range;

- A broad condensate region is desirable in order to achieve considerable condensate dropout during the experiment;

- Gas and liquid should show large discrepancies in density so as to be easily distinguished by X-ray CT imaging.

Figure 3.1 shows the phase envelope for a binary gas-condensate mixture which satisfies the four principles mentioned above. This system is composed of a mix of 85% methane and 15% butane. At a temperature of 20 ^oC and a pressure from 130 atm to 70 atm, this phase diagram has a good retrograde region.

3.1.2   Difference Between Static Values and Flowing Values

Numerical simulation models can provide relatively fast and inexpensive estimates of the performance of alternative system configurations and/or alternative operating procedures. Hence, some preliminary numerical simulations were performed prior to the experiment to investigate possible operating schemes. To use the simulation results properly, it is important to understand the difference between simulation and experiment outputs, especially the static and flowing parameter values in each setting. The static values are properties, such as saturation and compositions of each component, at a given reservoir location, while the flowing values are only associated with the property of the flowing fluid at this given location and a given time. In the reservoir simulation, static values will refer to the property values of a given grid block at a given time, while in experiment and field cases, samples collected come from the flowing phase only. Due to the constraints of relative permeability and interfacial tension, only the gas and some part of the liquid is mobile, hence the component
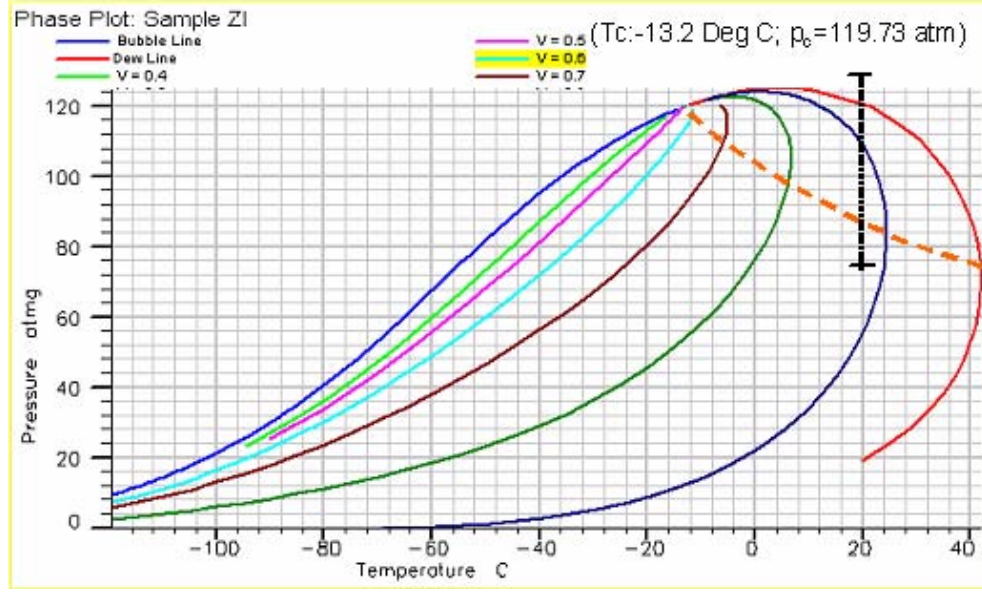
Figure 3.1: Phase diagram for a two-component methane-butane gas-condensate system (PVTi, 2003a, PR(1978) EoS). For this system, the critical temperature and the critical pressure are $T_c = 6.3\ ^oC$ and $p_c = 128.5\ atm$ respectively. At room temperature, the system produces a moderate retrograde region.

composition of the flowing phase is generally different from the static values in the two-phase region. The discrepancy between the static values and flowing values depends on the flow region, as shown in Figure 3.2. In *Region*1, the flow pressure is still above the dewpoint pressure, only the single-phase gas flow is present, hence the static values and flowing values in *Region*1 will be the same. In *Region*2, the flow pressure drops below the dewpoint pressure, liquid forms, drops out from the gas phase and accumulates in the reservoir. However, the accumulated liquid saturation is not sufficient to overcome the constraint of relative permeability, the liquid remains immobile. Thus unlike *Region*1, the property values in the flowing phase in this region will differ from the static values. In *Region*3, the accumulated liquid saturation exceeds the critical liquid saturation, part of the liquid starts to join the flowing gas phase and would be produced at the wellhead (Figure 3.3). Thus in *Region*3, the

static and flowing phase fluid properties will differ. In the simulation, the overall hydrocarbon component mole fractions at the separator are calculated based on the mass balance, as given by Eq. 3.1, then a flash calculation is performed at separator condition and fixed z_c to determine the hydrocarbon component mole fraction in the liquid phase (x_c) and in the vapor phase (y_c) respectively.

$$z_c = \frac{Q_c^{WH}/Mw_c}{\sum_{i=1}^{n_h} Q_i^{WH}/Mw_i} \tag{3.1}$$

Mw_c is the component molecular weight, and Q_c^{WH} is the component well head mass flow rate, is calculated as Eq. 3.2:

$$Q_i^{WH} = WI^{WH} \cdot \sum_p \left[\lambda_p \rho_p X_{ip}(p_p - p^{WH})\right] \tag{3.2}$$

WI^{WH} is the well index (Peaceman, 1996), a constant defined by the geometry property of the well blocks; p_p is the phase pressure of the well block and p^{WH} is the wellbore pressure for the well in the well block; X_{cp} is the mole fraction of component c in phase p; λ_p is mobility of phase p, and ρ_p is the density of phase p. The phase mobility is determined by Eq. 3.3:

$$\lambda_p = \frac{k_{rp}}{\mu_p} \tag{3.3}$$

Because of the liquid build-up around the well and in the reservoir, the overall component mole fractions (the static values) at a given location and a given time also changes with time, and can be very different from the original reservoir fluid configuration. The overall hydrocarbon component mole fractions in the reservoir is given by Eq. 3.4 in two-phase scenario:

$$z_c = x_c L + y_c V \tag{3.4}$$

or Eq. 3.5 given the saturation and component molar density information known.
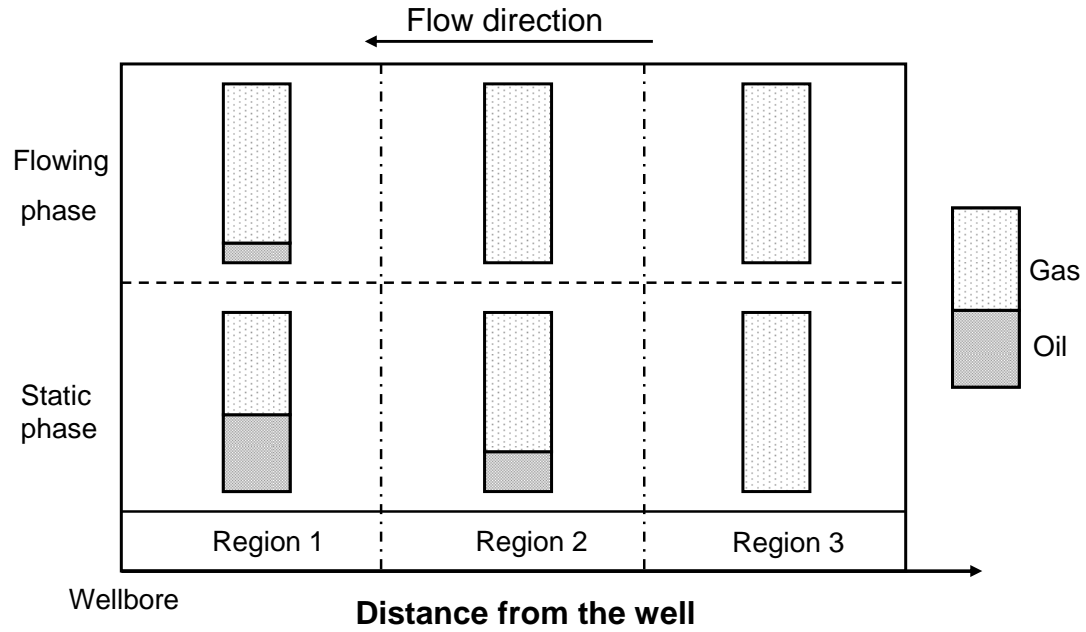
Figure 3.2: The difference of static values and flowing values in three regions.
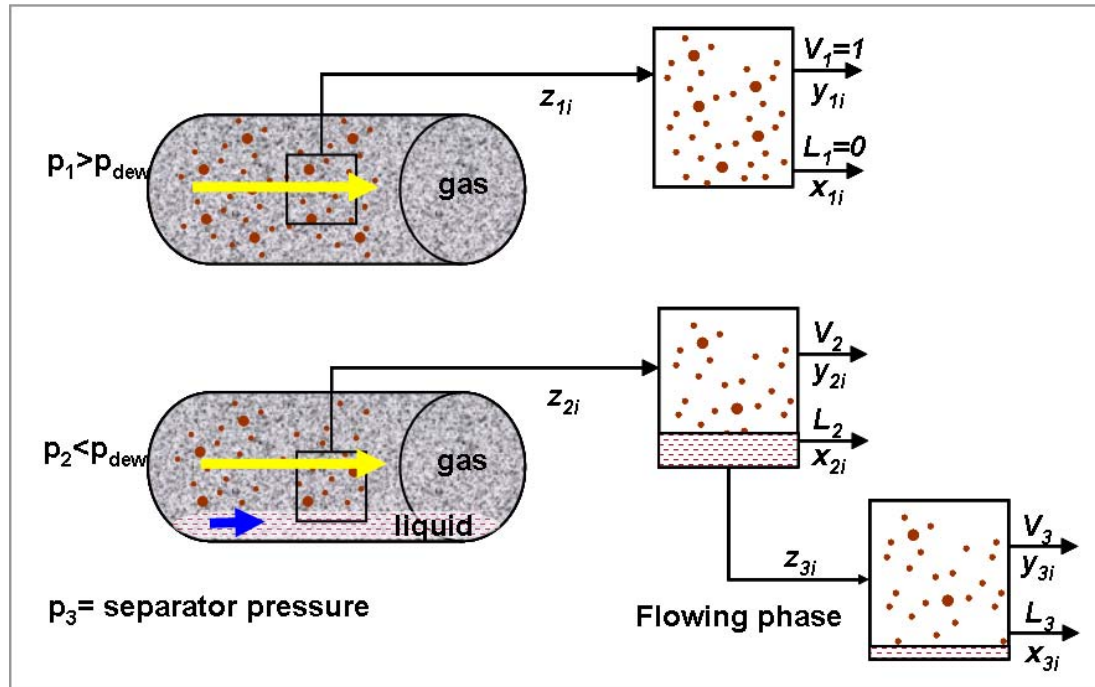
Figure 3.3: Schematic of composition variation in the reservoir under different pressures and at different conditions.

$$z_c = x_c S_l \rho_l + y_c S_g \rho_g \qquad\qquad (3.5)$$

Where, L and V are liquid and vapor mole fraction respectively, S_l and S_g are the liquid and gas phase saturation respectively and ρ_l and ρ_g, the component molar density of liquid and gas phase respectively.

3.1.3   Preexperiment Numerical Simulation

In this study, several preexperiment numerical simulations at core scale were conducted to define the experimental parameters, such as flow pressures and experiment duration, and to examine the range of the liquid buildup and the extent of the compositional variation. Two wells, one gas injector and one producer, were used in these simulation models. Both wells were controlled by bottom-hole pressures (BHP). The BHP of the upstream injector was set above the reservoir dewpoint pressure while the downstream producer has BHP below the dewpoint pressure, such that the fluid from the injection well was always in gas phase, and the fluid around the producing well was always in two-phase. The flow in the core flooding simulation was manipulated under the condition of constant pressure drop.

To investigate the experimental duration, we first set the BHP control for injector at 130 atm and for producer at 70 atm, thus a constant pressure drop of 60 atm is maintained. Figure 3.4 (a) illustrates that in the preexperimental simulation the mole fraction of the heavier component C_4 in the flowing phase drops to about 8% and then within one minute it stabilizes to the upstream C_4 composition of 15% as the flow reaches steady-state; meanwhile, liquid saturation (Figure 3.4 (b)) builds up quickly once the pressure drops below the dewpoint pressure and the maximum condensate accumulation reaches as high as 53% in one minute, although the critical condensate saturation (S_{cc}) is only 25% based on the input relative permeability curve and the maximum liquid dropout from the CVD experiment is only 9%. A wide range of saturation change occurs within one minute, and after two minutes, the saturation has a slight drop from the maximum value and stabilizes around 52% near the producer region. The saturation around the injector remains zero as two phases

do not develop in regions with high reservoir pressure.

The composition of butane component in the liquid phase (Figure 3.5 (*a*)) and the overall in-situ composition of butane component (Figure 3.5 (*b*)) also show dramatic changes within the first two minutes of flow. Due to the relative permeability effect, the liquid dropout accumulates in the reservoir, and causes a major change in the in-situ composition configuration. The overall butane composition changed from the original 15% to 45% around the producer.

Composition varies little in the flowing phase under constant pressure control, as we just illustrated. Only the flowing phase can be collected in the lab/field through the producing fluid, so in addition to the fluid sampled during the constant pressure drop flow, we needed to develop a methodology by which we can collect samples to investigate the composition variation that occurred in the reservoir. In the simulation, both the injector and the producer are open, and the flow is maintained under constant pressure drop, then after 60 minutes both wells are shut down. Figure 3.6 shows profiles for both x_{C_4} and z_{C_4} history before and after the buildup test. From the simulation results, we can conclude that both the static overall butane mole fraction (z_{C_4}) and the liquid butane composition x_i vary immediately after the shutdown of injector and producer. The greatest variation of component mole fraction occurs within six seconds after the shutdown and around the producer. After six seconds, the composition profiles stabilize as depicted the curves at $t = 60.0997$ minutes in Figure 3.6. The saturation profiles (Figure 3.7) also show dramatic changes before and after the shutdown. Different from the saturation profiles, the composition profile keeps changing after $t = 60.0997$ minutes as the saturation dispersion proceeds in the core.

Besides the buildup test, we also looked into the behavior of flow under different bottom hole pressure (BHP) controls. These simulations were performed with the same BHP control on the upstream injector ($BHP = 130\ atm$), but different BHP controls on the downstream producer. The downstream BHP ranged from 30 atm to 110 atm, which gives a range of pressure drop from 100 atm to 20 atm. Figure 3.8 shows that the lower the bottom-hole pressure (BHP), the more the butane accumulates in both liquid phase and the heavier the overall composition configuration.
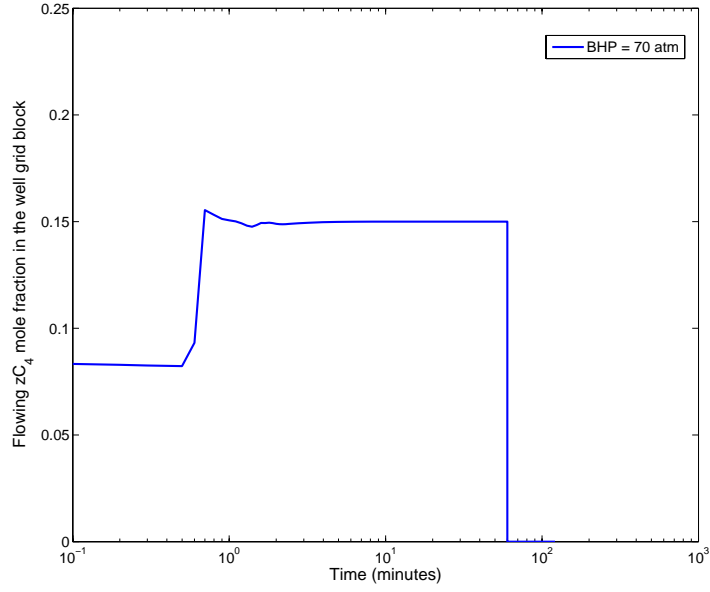
(a) C_4 mole percentage in the flowing phase.
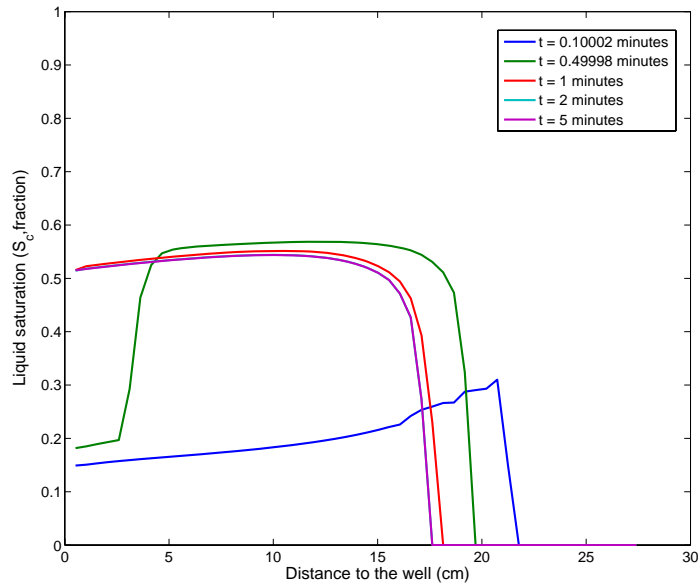
(b) Saturation distribution profiles.

Figure 3.4: Simulation results for $BHP = 70\ atm$ scenario. (a) C_4 mole fraction profile in the flowing phase (b) Saturation distribution profiles at different flow times.
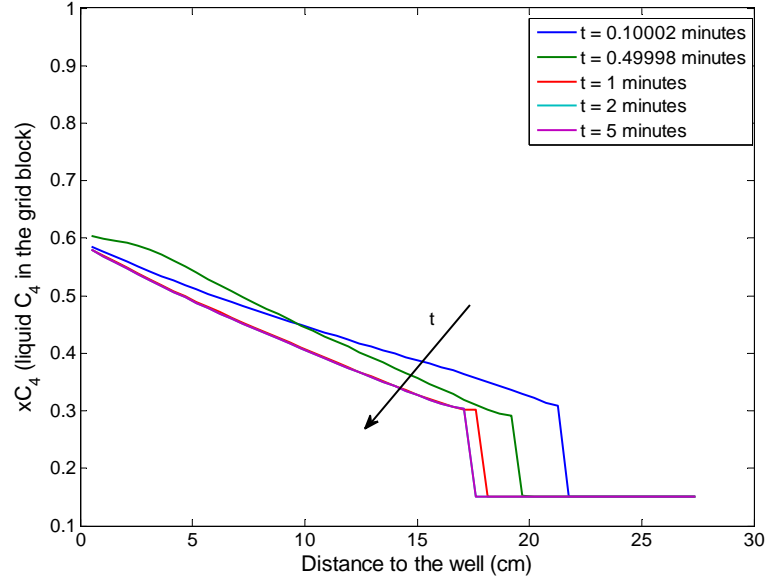
(a) x_{C_4} distribution.
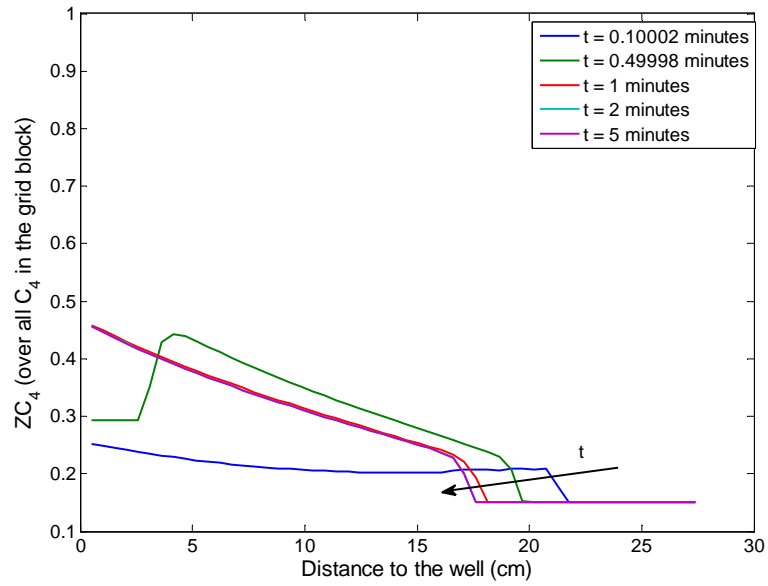
(b) z_{C_4} distribution.

Figure 3.5: In-situ composition history of butane component in (a) Liquid phase and (b) The overall composition configuration.
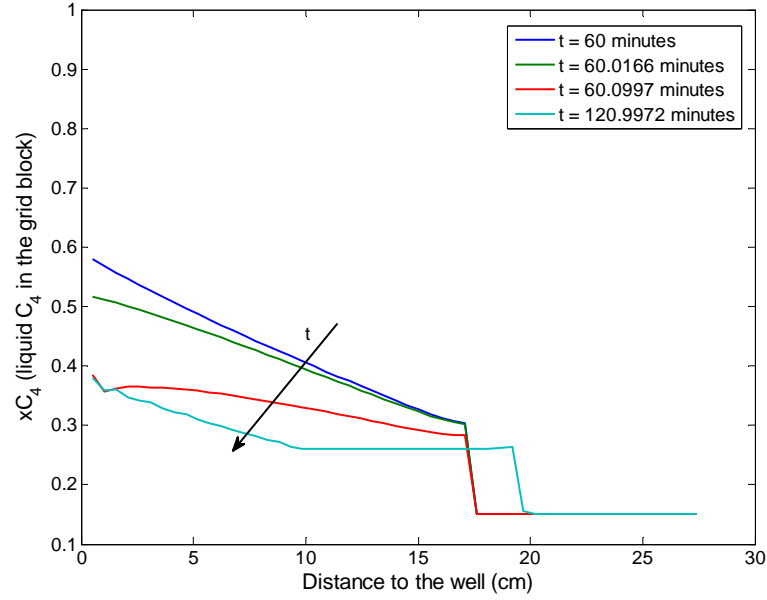
(a) x_{C_4} distribution.
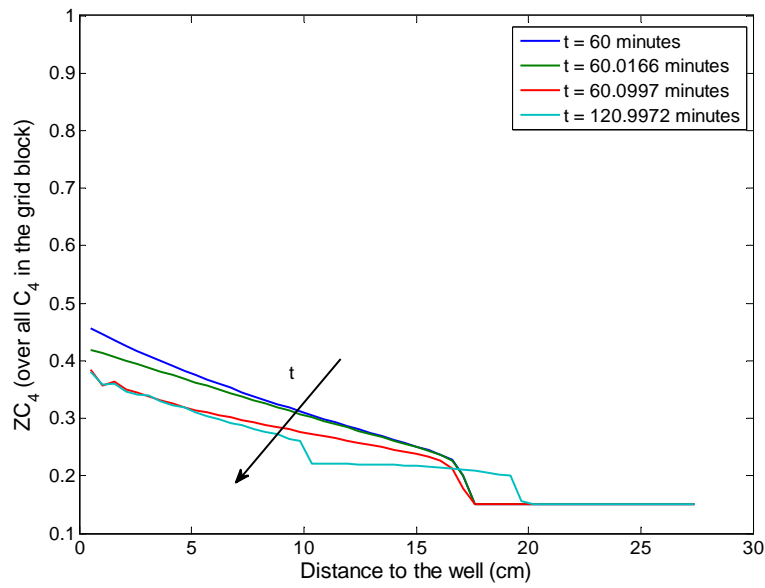
(b) z_{C_4} distribution.

Figure 3.6: In-situ composition history for butane component during buildup test in (*a*) Liquid phase and (*b*) The overall composition configuration.
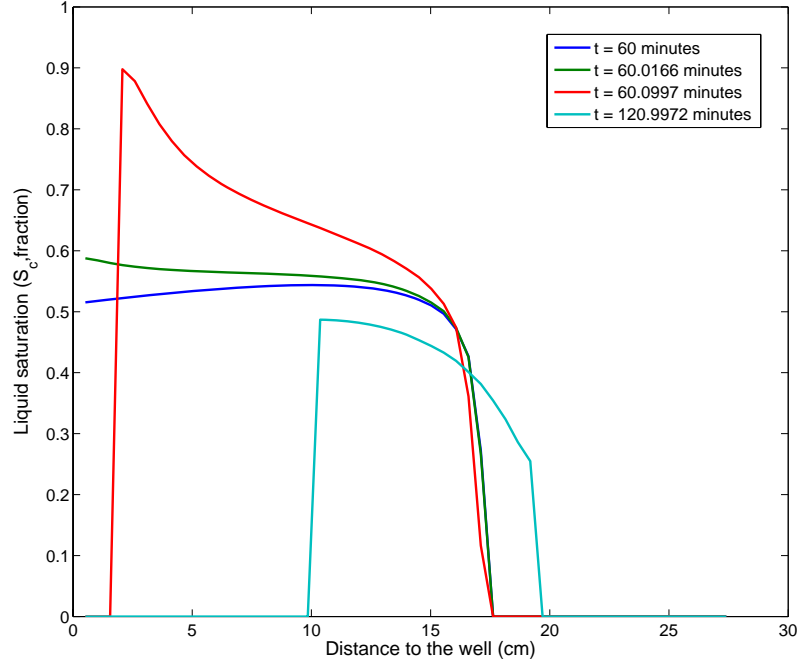
Figure 3.7: Saturation distribution in the core during buildup.

At and around the producer region the accumulation of the heavier component C_4 in the liquid phase can vary from 40% to as high as 75%, and even for the overall static composition in this region the mole fraction can vary from 30% to 63%. The different BHP scenarios produce different pressure distributions in the core. The higher the BHP at the producer, the larger the single-phase region, hence the liquid accumulates in a smaller region around the well.

Figure 3.9(a) illustrates that the component mole fractions in the flowing phase at the wellbore do not vary linearly with BHP. When the producer is under the BHP control of 50 atm, the mole fraction of the heavier component butane in the flowing phase experiences the greatest lost in the first 40 $seconds$ of flow, and then stabilizes back to 15% as the flow reaches steady state. However in the $BHP = 30$ atm case, instead of losing more butane in the reservoir, there is about 0.43% increase in the concentration of butane in the produced fluid. This may be due to the fact that part
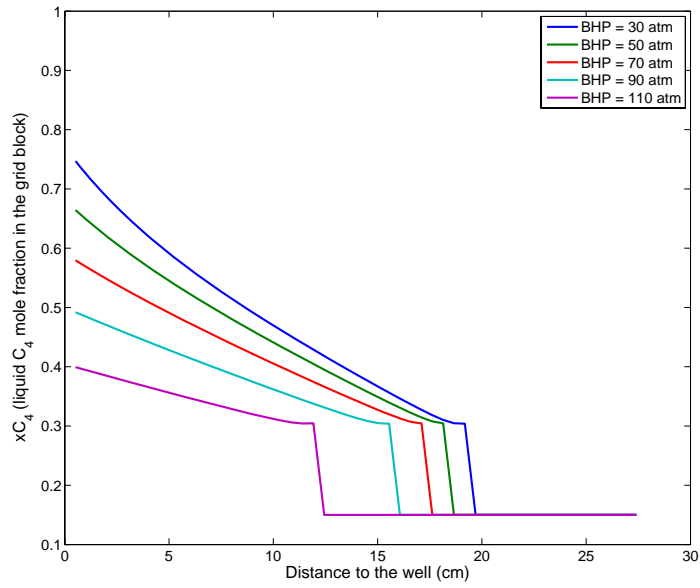
(a) x_{C_4} distribution.
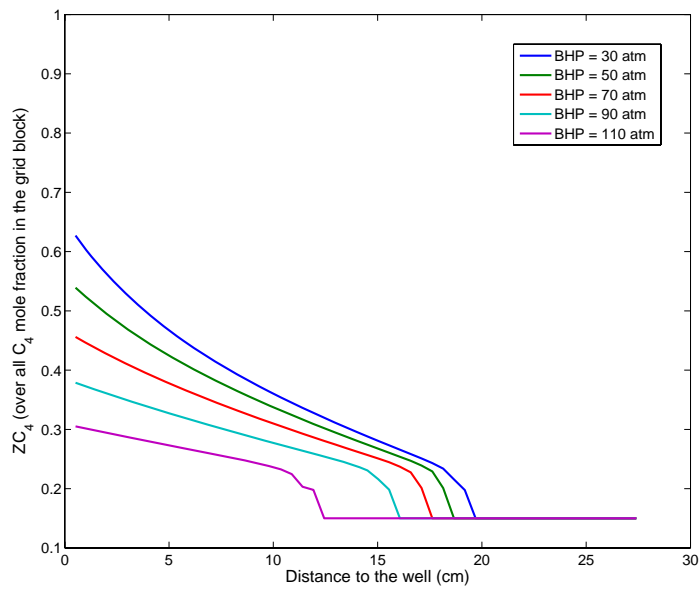
(b) z_{C_4} distribution.

Figure 3.8: In-situ composition history for butane component with different BHP control scenarios in (a) Liquid phase and (b) The overall composition configuration.

of the reservoir liquid revaporizes at lower BHP, such as $BHP = 30$ atm, hence more butane is produced in the well. When the producer BHP is greater than 50 atm, the higher the BHP, the more butane produced from the well in the first one minute, then after the first one minute, the butane mole fraction stays at 15%.

Figure 3.9(b) shows the distribution profiles of the liquid saturation at $t = 5$ minutes for different BHP scenarios. From these profiles, we can conclude that the lower the bottom-hole pressure at the producer, the shorter the range of the liquid accumulation in the near-well region. Contrary to the overall and liquid composition distribution in Figure 3.8, the lower the BHP, the greater the liquid accumulation in the well. Away from the well, the liquid accumulation increases slightly or remains constant in the two-phase region for all BHP controls except $BHP = 110$ atm. When $BHP = 110$ atm, the pressure drop along the core is only 20 atm, and under pressures greater than 110 atm, the reservoir fluid forms less liquid dropout than the maximum liquid dropout, hence, at $t = 5$ minutes, the accumulation rate of the liquid saturation is greater than liquid flow rate, hence more liquid accumulates in the wellblock.

The preexperiment numerical simulation gave us a rough idea of how the binary gas-condensate system performs under a constant pressure drop condition and how fast the composition and saturation redistributes during a buildup. In the subsequent experiments, we used the conditions as learned from the numerical simulations and investigated the flow behavior of the selected gas-condensate system by physical observations.

3.2 Experimental Apparatus

The experimental apparatus was modified from an earlier design of Shi *et al.* (2006). The experiment system is illustrated in Figure 3.10. This system is comprised of four subsystems: the gas supply and exhaust system, the core flow system, fluid sampling and data acquisition system. A photograph of the whole system is shown in Figure 3.11. The details of each component in the four subsystems, the major measuring techniques associated with composition and saturation measurements are presented
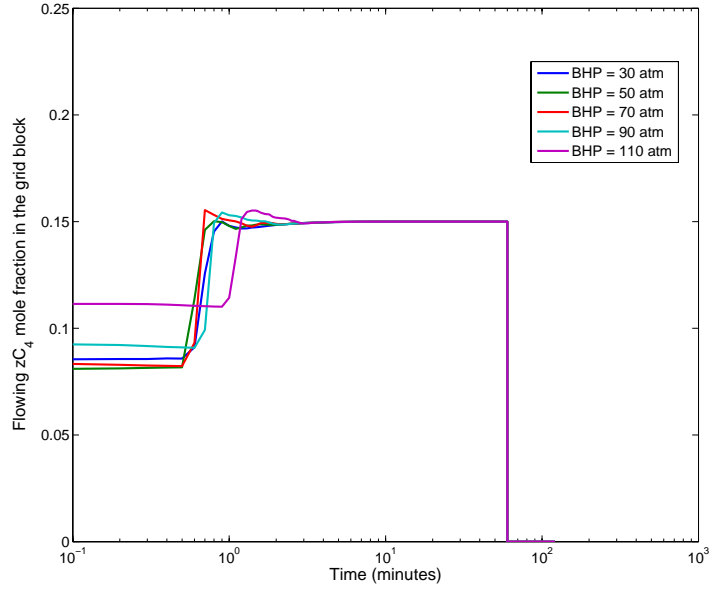
(a) C_4 in the flowing phase.
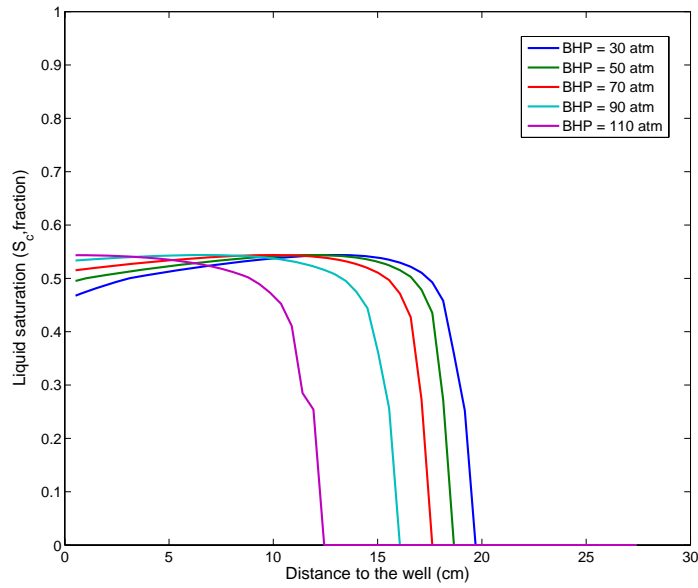
(b) Saturation distribution.

Figure 3.9: Simulation results for different BHP control scenarios. $(a)C_4$ mole fraction profiles in the flowing phase (b) Saturation distribution in the core.
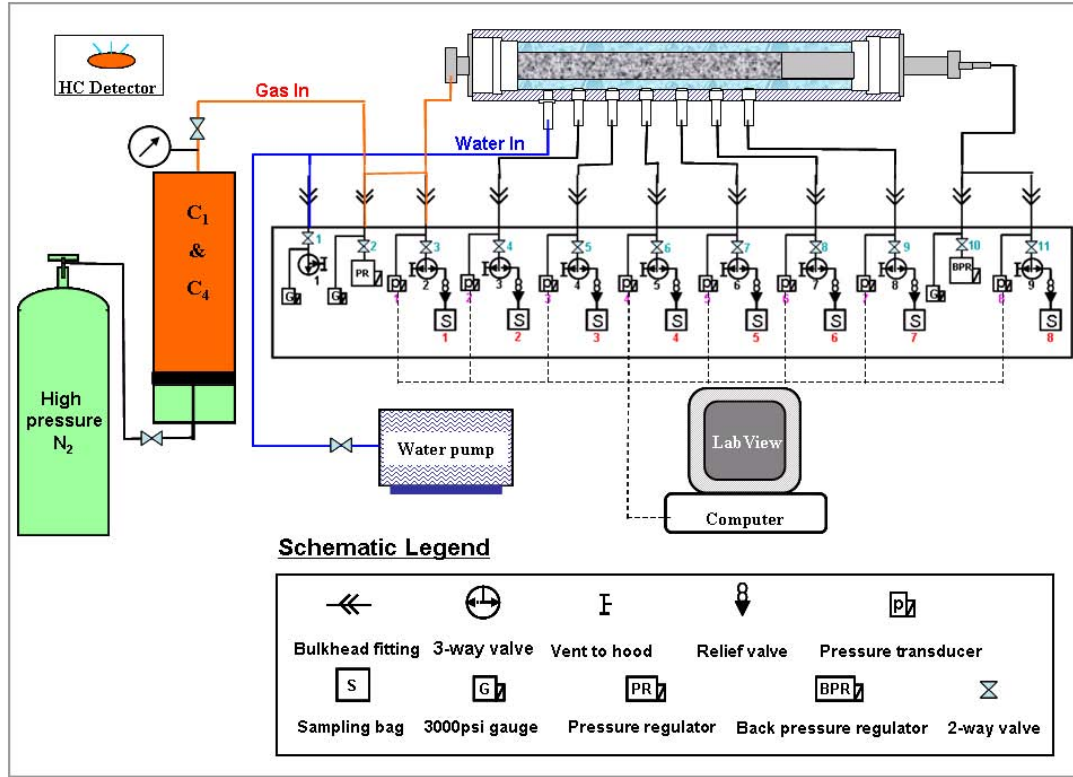
Figure 3.10: Schematic diagram of the gas-condensate flow system. The confining pressure is provided by a high pressure water pump and the gas-condensate mixture is stored in a piston cylinder, which is supported by a high pressure nitrogen cylinder to maintain the mixture pressure at $2200psi$. Pressures along the core are monitored by the high pressure transducers and fluid samples are collected from the six ports along the core for composition analysis.

in the following sections.

3.2.1 Gas Supply and Exhaust

The upstream gas mixture is stored in a piston cylinder ($HaiAn, China$, capacity 4,000 ml, pressure range 0-4641 psi), and the cylinder pressure is controlled by a high pressure nitrogen cylinder (6000 psi). The downstream gas exhaust was discharged to a fume hood directly in the constant pressure drop experiment since the total volume of the exhaust is very small and safe to dilute into the atmosphere. After the buildup
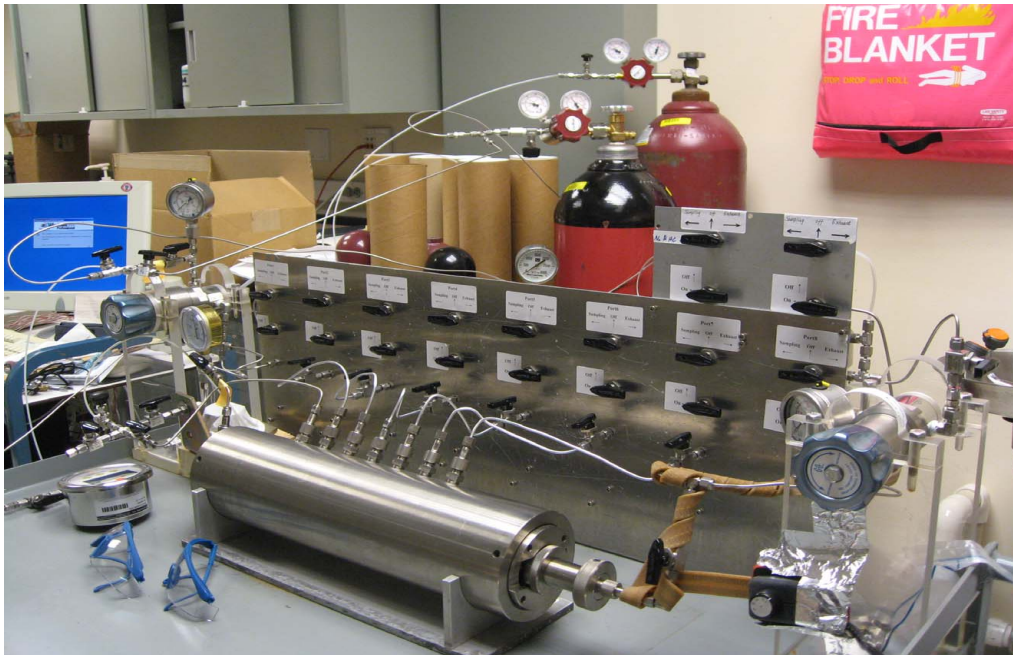
(a) Front view.
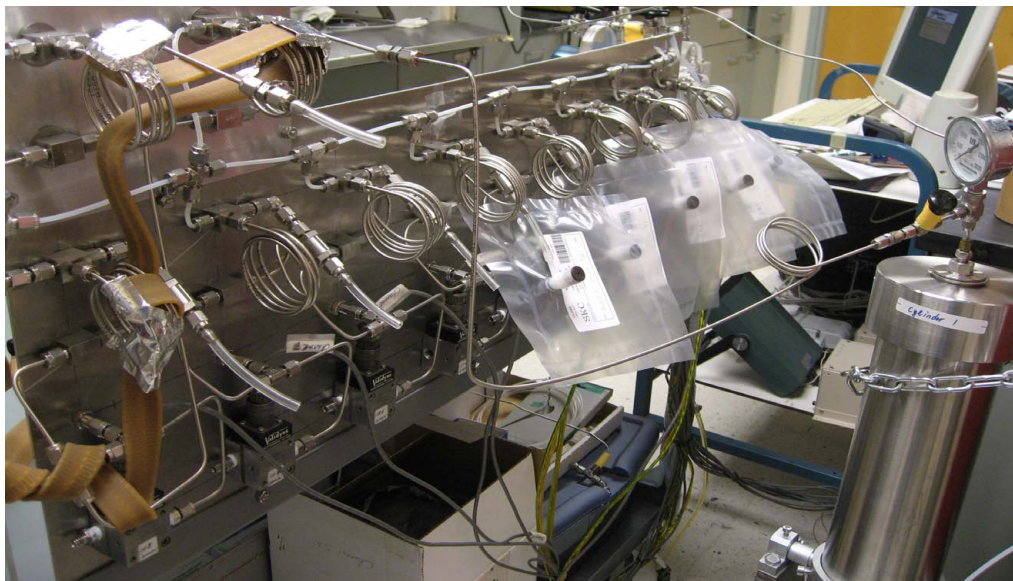
(b) Rear view.

Figure 3.11: Images of the experiment apparatus for the gas-condensate flow system. (*a*) Front view, the high pressure titanium core holder is in the foreground, this core holder has six ports along the core to allow for pressure monitoring and fluid sampling (*b*) Rear view, the sampling system and the pressure transducers are in the foreground.

test, the core was discharged into another empty piston cylinder, so that the collected fluid could be analyzed to determine the total composition.

3.2.2 Core Flow System

The core flow system consists of a titanium core-holder (*Shiyi Science and Technology*, model J300-01), which can support a maximum confining pressure 5800 *psi*), while maintaining the pore pressure at 5366 *psi*. A photograph of the core holder is shown in Figure 3.11(*a*). The high pressure titanium core holder has six ports along its length to allow for pressure monitoring and fluid sampling. A homogeneous Berea sandstone core was selected for this experiment. The core has a length of 25.04 *cm* and a diameter of 5.06 *cm* with an average porosity around 15% and an average absolute permeability about 5 *md*. The choice of permeability was intentional, as it was necessary to produce pressure drops of suitable magnitude to create the desired condensation region during flow.

3.2.3 Fluid Sampling System

One of the unusual aspects of this experiment is the ability to measure the in-place composition, as well as the usual pressure data along the length of the core. The in-place composition samples are collected with Tedlar gas sampling bags (*SKCwest*, model 232-02) attached to the six sampling ports along the core-holder. In order to protect the gas samples from being polluted by other gases, the gas sampling bags are connected to the system in a way such that the bags can be vacuumed before the experiment. The sampling pressure is regulated by the 25 *psi* relief valves to ensure the sampling pressure lower than the pressure limits of the sampling bags. Collecting the fluid samples directly from the flow system is challenging. Both the sample size and the sampling duration need to be carefully manipulated. To reduce the error involved in the sampling process and also to ensure all samples are collected at roughly the same time, the sampling system is specially designed as shown in Figure 3.12. A one-meter long stainless steel coil is installed prior to the relief valve to capture and temporarily store the fluid sample. During the sampling process, we
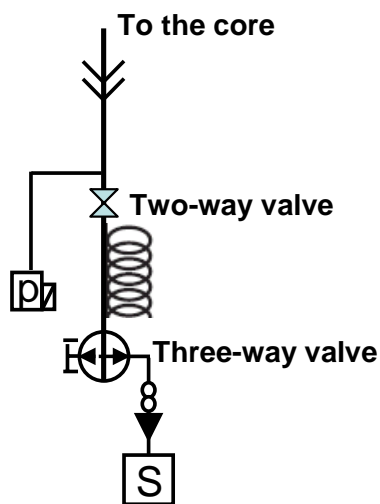
Figure 3.12: Schematic and photograph of the gas sampling system. (*a*) Schematic diagram. The fluid sample is first stored in the one-meter long coil, then released to the sampling bag. (*b*) Photograph of the sampling system.

first opened the two-valve valve (as depicted in Figure 3.12 (*a*)) connected to the pressure port in the core holder and captured the fluid sample in the coil, this sample could then be released later to the sampling bag. At atmospheric pressure, the one-meter long coil can store as much as 7.91 cm^3 of gas, which is sufficient for one gas chromatography analysis. Fluid samples coming from the core are usually at high pressure, hence the volume of the fluid stored in the coil is normally expanded to larger volume in the sampling bag. By experience, at core pressure higher than 1500 *psi*, opening the two-way valve in Figure 3.12 (*a*) for 2 seconds, the amount of fluid stored in the coil will be ideal for gas chromatographic analysis, while at core pressure within the range of 1000 *psi* to 1500 *psi*, 3 to 5 seconds is required. For fluid pressure lower than 1000 *psi*, longer sampling time is needed. The collected gas samples were sent to an *Agilent* 6820 series gas chromatograph to analyze the compositions. The gas chromatograph configuration will be discussed in detail in the next section.

3.2.4 Data Acquisition System

All pressure measurements were electronic and digitized by using a high-speed data acquisition system (DAQ; National Instrument, SCSI-1000 with PCI 6023E A/D board). In the original design of Shi *et al.* (2006), the in-place pressures were measured by pressure transducers with different capacities, chosen according to the pressure range and the requirement of the measurement resolution. The absolute pressures on both upstream and downstream were measured with high pressure range 2,000 *psi* transducers , and the differential pressures between each pair of sampling ports were measured with low range 320 *psi* transducers. Several issues arose from this design. First, the pressure transducers along the core did not generate reliable differential pressure data in the earlier experiment due to the escalated zero shifting problems and the dependency of each sampling port on its neighbors; secondly, the low pressure transducers were prone to damage in case of leaks in the system. Pressure differences between each pair of sampling ports are small when the flow system is under constant pressure drop and reaches steady-state flow, and can become very large under nonsteady state conditions. In the redesigned experiment, we replaced all the low pressure transducers with high pressure ones and measured the absolute pressure at each sampling port instead of differential pressure between sampling ports. This removed the pressure dependency on the neighboring ports and prevented over-pressurizing the transducers along the core. The absolute inlet and outlet core pressures were also monitored. All pressure data from the eight transducers were logged by the data acquisition system for analysis.

3.2.5 Gas Chromatography (GC) System

Chromatography is a separation technique used to separate and analyze a mixture of compounds which are comprised of individual components. A mixture of various components enters a chromatography process together with the carrier gas, an inert gaseous mobile phase, and the different components are flushed through the system at different rates. These differential rates of migration as the mixture moves over adsorptive materials provide separation, and the rates are determined by the repeated
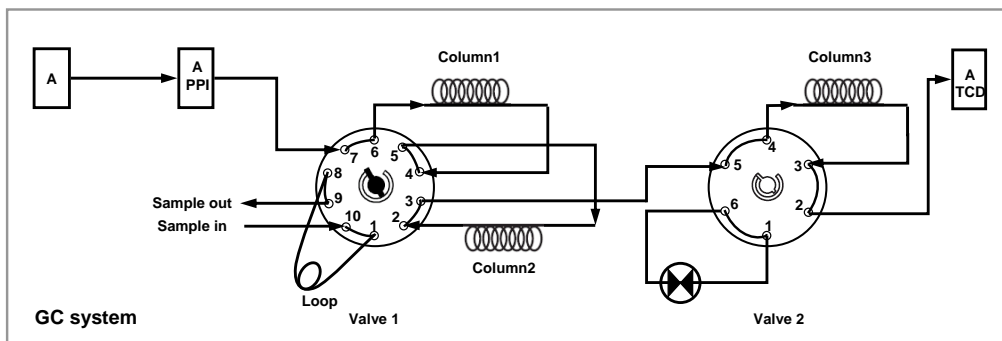
Figure 3.13: Schematic diagram of the valve and column configuration in the GC (Parakh, 2007).

sorption/desorption activities that take place during the movement of the sample over the stationary bed. The smaller the affinity a molecule has for the stationary phase, the shorter the time spent in a column. In Gas Chromatography (GC), the sample is vaporized and injected onto chromatographic columns and then separated into many components.

In this study, GC analysis for component composition were performed on the Agilent 6890N series GC, this GC is equipped with a purged packed inlet and single filament Thermal Conductivity Detector (TCD). The configuration for the valves and the columns designed inside the GC chamber are shown in Figure 3.13. This valve and column configuration was designed originally for permanent gas analysis (Zhou *et al.* (2003). Valve 1 in this system is a 10-port valve for automatic gas sampling and backflush of the precolumn to the detector. Two columns can be associated with the 10-port valve. A 6-port switch valve (Valve 2), with adjustable restrictor, is used to switch the column in and out of the carrier stream. Column 3 is isolated when Valve 2 is on. The purged packed inlet is interfaced directly to the valve to provide a source of carrier gas. Since there are only two light hydrocarbon components, methane and butane, in our gas-condensate system, hence one column (Agilent GasPro, $15m \times 0.53\ mm \times 40\ \mu m$) was installed in the position of column 1, column 2 was replaced directly by a by-pass stainless steel tubing, and column 3 was isolated from the system by switching valve 2 on. The detailed GC setup is listed in Table 3.1:

Table 3.1: Gas Chromatographic Conditions.

GC	Agilent 6820 Gas Chromatograph
Data system	ChemStation
EPC Purged packed inlet (Heater temperature)	$200°C$
EPC Purged packed inlet (Heater pressure)	$22.64psi$
Valve temperature	$150°C$
Carrier flow(Helium)	$3.2mL/min$
Column	GS-GasPro (part number: J&W 113-4362)
Oven	$50°C$ initial, hold for 3.00 minutes; increase from $50°C$ to $200°C$ at the rate of $25°C/min$; then hold at $200°C$ for 3 minutes.
Detector	TCD, $250°C$
Reference flow	$30.00mL/min$
Make up flow	$10.00mL/min$

The thermal conductivity detector (TCD) used in this study is a concentration sensitive detector. It is simple and easy to use and suitable for the analysis of permanent gases, hydrocarbons, and many other gases. The single-filament flow-switching design eliminates the need for a reference column. Since TCD is based on the principle of thermal conductivity, it depends upon the composition of the gas. The difference in thermal conductivity between the column effluent flow (sample components in carrier gas) and the reference flow of carrier gas alone, produces a voltage signal proportional to this difference. The signal is proportional to the concentration of the sample components. Different components in the sample gas produce different signals due to the difference of the thermal conductivity between the pair of the sample component and the carrier gas. Thus gas chromatography is a relative method, so calibration with a
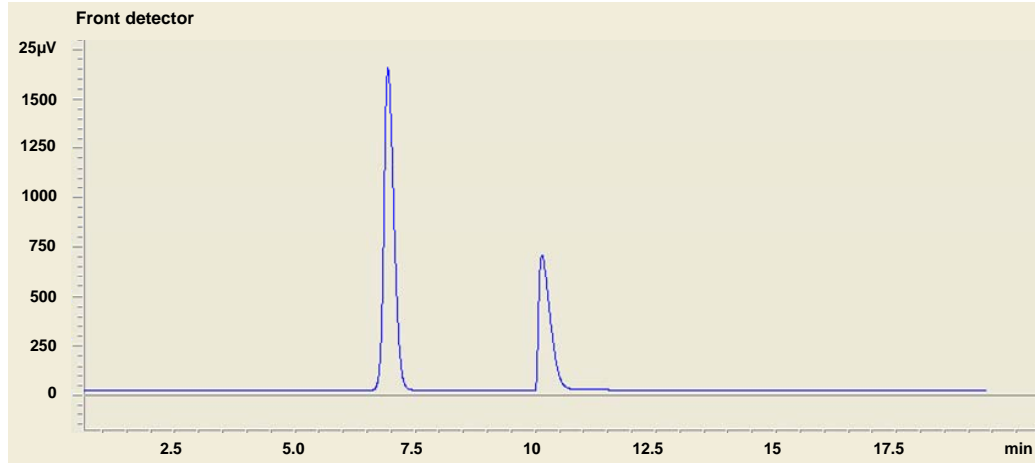
Figure 3.14: GC curve for a methane and butane mixture. The measurement shows good signal-to-noise ratio, and the baseline is also very stable.

standard mixture is required for mixtures having components with different thermal conductivities.

Figure 3.14 shows the chromatogram of a mixture with a volume of 10 ml, the methane and butane were easily detected at a good signal-to-noise ratio. The baseline was also very stable.

Because the difference of the thermal conductivity between methane and helium is smaller than that of butane and helium, the butane peak is prone to be wider and hence the apparent butane mole percentage is elevated to a higher than true value. Therefore, the measurement is calibrated with mixtures of fixed methane and butane percentage. Figure 3.15 shows the calibrated curve for butane. The actual butane percentage in the following experiment is calculated based on the calibration Eq. 3.6:

$$z_{C_4\_}c = 0.0084z_{C_4\_}m^2 + 0.198z_{C_4\_}m \tag{3.6}$$

Where, $z_{C_4\_}c$ and $z_{C_4\_}m$ are the calibrated butane mole percentage and measured butane mole percentage respectively.
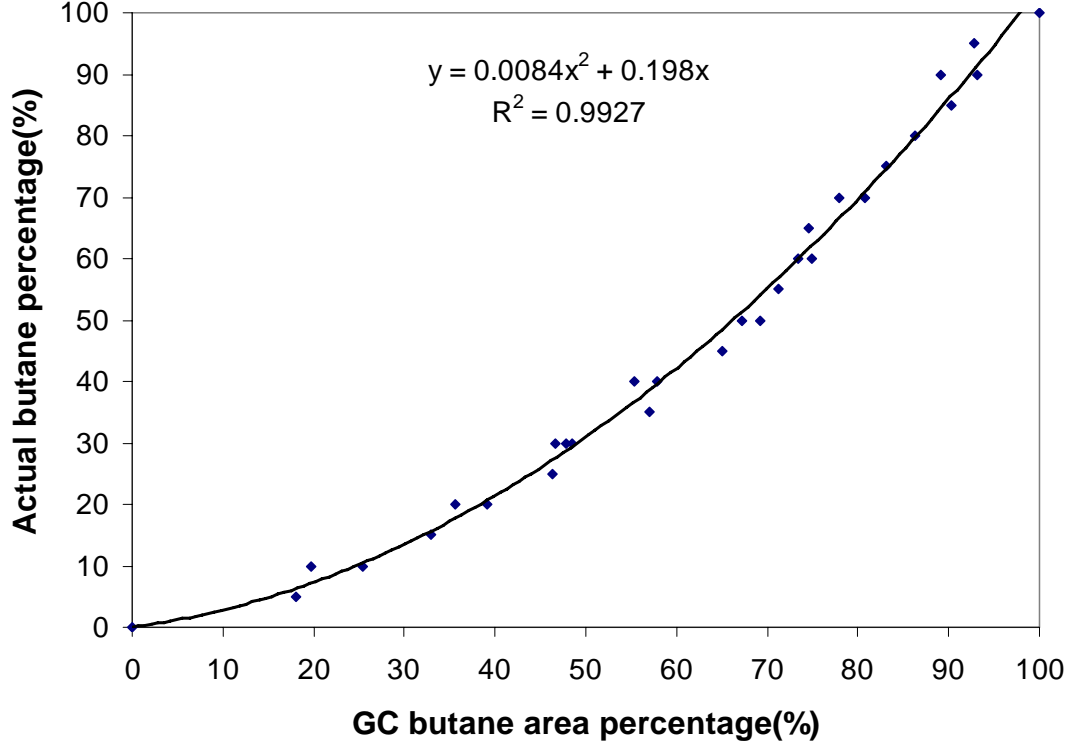
Figure 3.15: The calibration curve for C_4 measurements. The calibrated butane mole percentage is calculated by: $z_{C_4\_}c = 0.0084z_{C_4\_}m^2 + 0.198z_{C_4\_}m$.

3.2.6 CT system

An X-ray computed tomography (CT) scanner (GE HiSpeed CT/i) was used in this study to measure the static saturation in the core. The scanner can also be used to monitor dynamic experiments, such as core floods as the two phases develop in the core. Because the CT number is directly proportional to the density of the object, so we can observe changes in CT numbers as two phases develop in the core.

Measurements with X-ray CT are subject to image artifacts, such as beam harding, positioning errors and X-artifacts etc. Special care and treatment are needed to improve the resolution of CT images. According to Akin and Kovscek (2003), object shape can lead to artifacts, the cross-sectional geometry of the scanner gantry is circular and the machine delivers the best images of objects that are also circular and symmetrical in cross-section. Beam hardening can be reduced by simply moving to
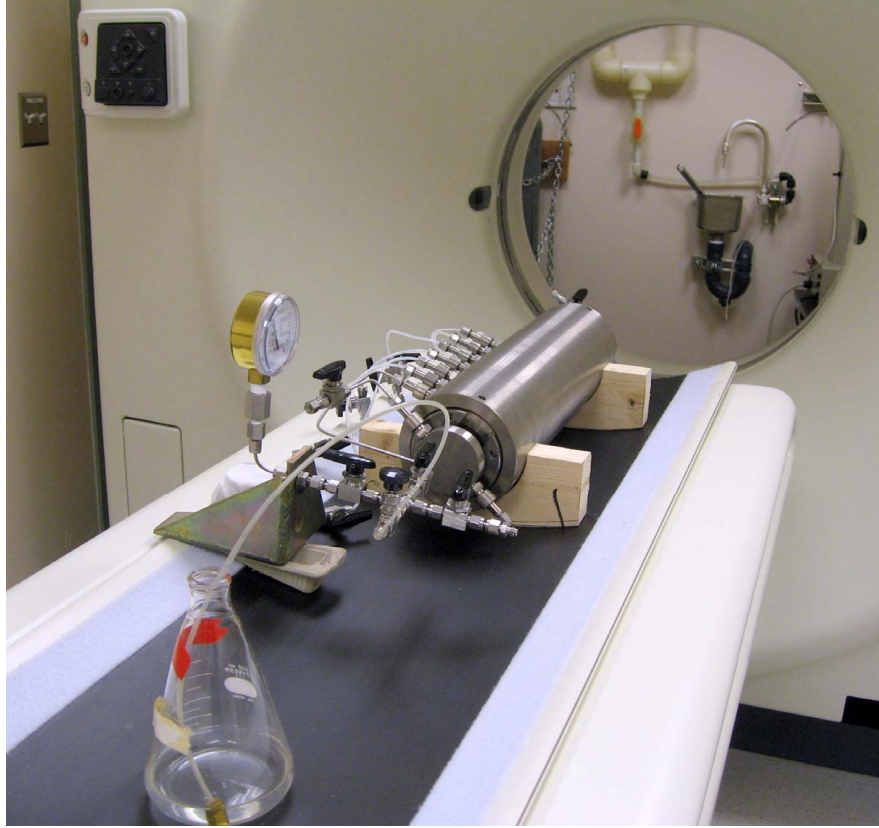
Figure 3.16: Apparatus for x-ray CT scanning.

higher energy X-ray sources. Positioning errors can be minimized by setting the scan object in a fixed position on the patient table. Figure 3.16 shows a photograph of the CT setup for this experiment. In this setup, positioning is accomplished electronically with $\pm$ 0.01 mm accuracy. An arc-shaped mounting bracket attaches to the core holder, the inside of the mounting bracket fits the core holder and holds the core holder tightly, and the outside the mounting bracket fits the patient table, and eliminates possible slippage between the core holder and the moving patient table. Thus the core holder is in a fixed position relative to the table.

By trial and error, the best quality resolution was made by selecting the optimum machine parameters. Table 3.2 shows the scanner settings used in this study.

Table 3.2: CT scanner settings.

Parameter	Setting
Field of View (DFOV)	15 cm
SFOV	Ped Head
Image Matrix	512 x 512
Sampling	512
Scan Speed	3 sec
Slice Thickness	$3mm$
Resolution	High
Kv	140
MA	200

The tubing system that connects the sample ports to the valve panel was specially designed to further reduce the influence of beam hardening. In the early stage of the experiment, Halar Tubing with 2500 psi pressure rating was adopted, the advantage of Halar tubing is that it is transparent in the CT scanning, but this type of tubing tends to become brittle and easy to break in the case of high pressure hydrocarbon flow, especially when the hydrocarbon flow undergoes phase changes. In the later stages of the experiment, aluminum tubing was adopted. Aluminum tubing has less beam hardening effect in the scanning system than stainless steel tubing and can also sustain high flow pressure without rupturing.

3.3 Experimental Procedures

3.3.1 Gas Mixing

According to the preexperiment simulation, 5.5847 $moles$ butane and 31.6465 $moles$ methane were required to fill the piston cylinder with size of 3,920 ml at 2000 psi and give the component mole percentage of 85% methane and 15% butane. Butane is
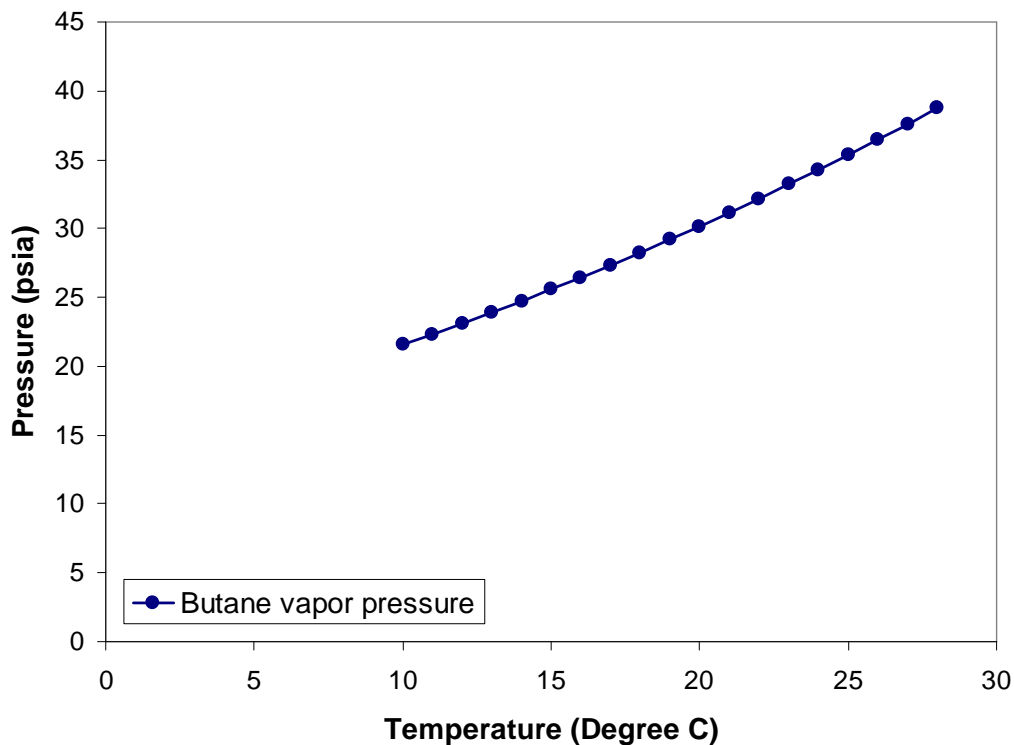
Figure 3.17: Butane vapor pressure curve.

usually stored in liquid state with the butane tank pressure around 60 psi. According to Figure 3.17, at room temperature, butane is in liquid phase as long as the fluid pressure is above 23 psi. The liquid butane can thus be transferred to an empty piston cylinder by gravity and small pressure difference between the butane tank and the piston cylinder. Methane usually is supplied in high pressure cylinders, so methane can be directly transferred to the piston cylinder by the high pressure difference.

Figure 3.18 shows a schematic of the whole process of mixing the liquid butane with gaseous methane. Firstly, the piston cylinder was vacuumed from the lower end as shown in Figure 3.18(a), thus the piston was pulled down to the bottom of the piston cylinder. At the same time, the tubing connecting to the water pump was also vacuumed to eliminate the air in the piston and tubing line. Water was then pumped to the vacuumed cylinder. The water can be delivered to the piston cylinder at a rate ranging from 0.01 ml/min to 9.9 ml/min. Low to intermediate injection rate

was adopted to minimize the air dissolved in the injection water. The piston cylinder was positioned horizontally after it was filled with water, and the tubing connecting the piston cylinder and the water pump was pulled vertically, with water head in the tubing high above that in the piston cylinder. The water-filled piston cylinder stayed horizontally for half a day to allow the dissolved air to evolve into the higher end of the tubing. The next step was to open the valve at the higher tubing end, and release all the accumulated air in the tubing, then put the piston cylinder back to vertical. Then the higher end of the tubing was opened again, still at a position higher than the top water level in the piston cylinder. Water was injected and the piston cylinder was ready for the next step if no water flowed spontaneously out of the cylinder. The water can flow out of the piston cylinder spontaneously only if the pressure inside the water-filled piston cylinder is higher than the atmospheric pressure. In this case, the cylinder is either pumped with too much water or there is too much air dissolved in the cylinder. Both scenarios are undesirable and would definitely influence the butane transfer in the next step, hence the water injection needs to be done carefully.

Secondly, the space was prepared for butane transfer. The volume of 5.6 *moles* liquid butane at room temperature is equal to a volume of 539 *ml* water. To transfer 5.6 *moles* liquid butane to the piston cylinder, we first injected nitrogen into the top of the water-filled piston cylinder prepared in Figure 3.18(a), so that the nitrogen drove the piston down and expelled the water out from the bottom. The next step was to open the valve at the bottom of the piston cylinder slowly, and collect the water in a beaker and weigh the water on a digital scale, shutting down the valve when the displaced water read 539 *g*. Then the nitrogen was released from the top of the piston cylinder, and the nitrogen source disconnected from the system.

Thirdly, the butane cylinder was connected to the the piston cylinder prepared in Figure 3.18(b) and then the tubing connection part and the top of the piston cylinder were vacuumed. If no air was dissolved in the water in the first step, then the piston will not be pulled up by the vacuum pressure since water has very low compressibility at room temperature. The butane cylinder was put upside down such that the liquid butane can flow directly into the piston cylinder. The butane was transferred and settled in the piston cylinder in a few minutes. The practice was to wait about half

an hour until the pressure in the butane cylinder stopped dropping. Then the valve on the butane cylinder and the valve on the top of the piston cylinder were shut, as in Figure 3.18(c). 5.6 *moles* butane had therefore been successfully transferred into the piston cylinder.

Lastly, the butane cylinder was disconnected, and the methane cylinder connected to the piston cylinder partially filled with butane as in Figure 3.18(c). The next step was to vacuum the connecting tubing and flow the methane directly into the piston cylinder as in Figure 3.18(c) and discharge all the remaining water from the bottom of the piston cylinder to the water bottle. The amount of methane transferred to the piston cylinder depends on the pressure on the methane cylinder. When the maximum pressure of the methane supply cylinder is around 2100 *psi*, the methane transferred to the piston cylinder is roughly 32 *moles* and the equilibrium pressure in the piston cylinder is about 2000 *psi*. Hence the mole percentage of the methane in the mixture is about 85%. Varying the supply pressure on the methane cylinder, we were able to slightly adjust the composition for the mixture by flowing less or more methane into the piston cylinder. The final composition of the mixture was determined accurately by GC composition analysis prior to conducting the flow experiment

The mixture prepared in Figure 3.18 (d) was ready for use when the piston cylinder was shaken 100 times to allow the methane and butane to be fully mixed with each other, then the mixture was pressurized to 2,200 *psi* for the core flow experiment by connecting the lower (empty) end to the high pressure nitrogen supply.

3.3.2 Core Flow Tests

In this section, the procedure of the five core flow experiments will be explained in detail. In Experiments A and B, the core was vacuumed and the hydrocarbon mixture was injected directly into the core before the flow experiment, while in Experiments C and D, the core was vacuumed and presaturated with high pressure methane. Experiment C and D were "capture" experiments in which the fluid flowed in the core for a given time, then both inlet and outlet valves were suddenly shut and all six sample parts immediately opened to sample the composition of the fluids. Fluid
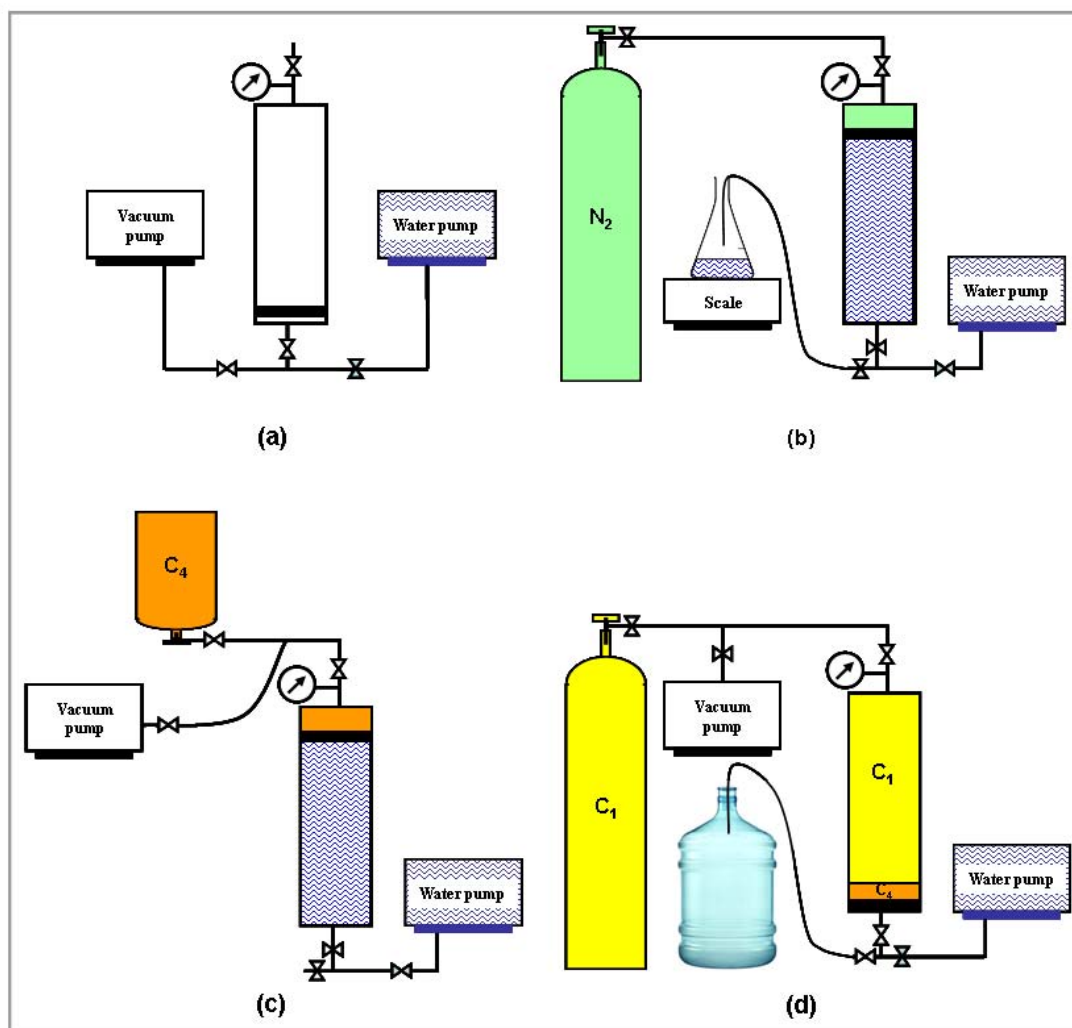
Figure 3.18: Overview of the gas mixing process. (*a*) Vacuum and fill the piston cylinder with water (*b*) Displace water from the piston cylinder with specified volume (*c*) Discharge liquid butane into the piston cylinder (*d*) infill the piston cylinder with high pressure methane.

samples were collected immediately after the core was captured. In Experiment E, the apparent permeabilities of the core to nitrogen gas were measured before and also after the hydrocarbon flow test.

Experiment A

In Experiment A, the whole flow system, including the core, the sampling system and the gas supply system, was fully vacuumed. The mixture in the piston cylinder was pressurized to 2200 *psi* with the support of the high pressure nitrogen. The maximum pressure of the nitrogen cylinder was 6000 *psi* and nitrogen was delivered under a pressure of 2200 *psi* using a regulator. The high pressure support from the nitrogen ensures the hydrocarbon mixture is always delivered as single-gas phase, as 2200 *psi* is well above the dewpoint of 1900 *psi*. During the experiment, the pressure regulator at the upstream was set around 1950 *psi*, the downstream valve was closed. The high pressure gas phase mixture was first flowed into the vacuumed core, and settled for about 2 minutes until the pressure in the core reached 1950 *psi*, then the first batch of fluid samples was taken.

The second batch of samples were taken during flow, which was controlled to be constant pressure drop with the upstream pressure regulator set at 1950 *psi* and downstream back pressure regulator set at 1000 *psi*. Samples were taken 40 *seconds* after the pressure drop along the core was stabilized. In this experiment, the coil setup shown in Figure 3.12 was originally a stainless tubing about 20 *cm* long. Longer sampling time was found necessary to ensure a sufficient sample size. The straight short tubing was later replaced by the 1 *meter* long coil in Experiments C, D and E to increase the sample volume. Because of the extended sampling time, there was sudden and dramatic pressure drop in the core during each sampling process.

Experiment B

Similar to Experiment A, two batches of samples were collected during the static and flowing conditions. Different from Experiment A, the mixture in Experiment B was slightly lighter because of the lower pressure provided by the methane cylinder

during the mixing process. The upstream pressure was regulated to a higher pressure of 2000 *psi*, hence the static samples were taken at 2000 *psi*. During the flowing stage, the upstream pressure was regulated to 2000 *psi*, and downstream to 500 *psi*, hence a bigger pressure drop occurred during Experiment B. In addition to changes in the pressure setting, the sampling was manipulated with extreme care during the experiment, and the two-way valves in Figure 3.12(a) were turned on slowly to minimize the sudden pressure drop during sampling.

After the flow, we shut down both the upstream and downstream valves on the core, as well as the valves on the sampling ports. The core was isolated, detached and taken to the CT scanning room for saturation analysis.

Experiment C

After Experiment B, the longer sampling coil design as in Figure 3.12 was adopted for better sampling. During the experiment, the core was vacuumed and presaturated with pure methane at a pressure around 2000 *psi*. Then at least two pore volumes of the gas mixture of methane and butane were flushed through the core to fully displace original methane gas. During the displacement process, the upstream pressure was set around 2000 *psi* and downstream to 1950 *psi* to ensure the mixture of methane and butane in the core was still in the gas phase. After about 10 minutes of the low pressure-drop flow, the downstream pressure was set at 1000 *psi*. Flow occurred at a high constant pressure drop for 3 minutes and reached steady state, then four valves, one before the upstream pressure regulator, one prior to the core holder, one right after the core holder and the one in the downstream of the back pressure regulator were all shut, capturing the flowing gas within the core. Samples from the six sample ports along the core were collected immediately after the flow shutoff. One sample from the tubing upstream of the core was collected, as well as a sample from the tubing between the back pressure regulator and the outlet end of the core. The valve at the end of the core was then opened, the fluid in the core was fully discharged into an empty piston cylinder, and one sample from the exhaust was collected.

Experiment D

The first part of Experiment D was exactly the same as in Experiment C, except the mixture was heavier than that in Experiment C. The heavier fluid was chosen to investigate the influence of the original fluid property on compositional variation. After discharging the hydrocarbon gas into the collection piston cylinder, the remaining liquid in the core was flushed out by injecting nitrogen into the core and three samples at the exit of the core were taken at three different times.

Experiment E

The apparent permeability to nitrogen was measured before and after the hydrocarbon flow test. The nitrogen was injected into the core with different pressures and the downstream flow rates were measured using the upside-down cylinder method, in which the volume of the gas outflow during a fixed time duration was calculated by monitoring the water displaced from the upside down glass graduated cylinder.

3.3.3   Sampling from the Tubing Ports

Earlier experience showed that samples from the various tubing ports were often problematic, and displayed different compositions when sampled under different pressure. This phenomena was more severe when the sampling pressure was below the dewpoint pressure. This was attributed to the fact that liquid and gas phases flow at different rate inside the tubing, hence the fluid captured in the sampling bag preferentially carried more gas or liquid, depending on whether the tube was pointing upward or downward. Hence the sample from the tubing was not representative. To reduce the sampling bias, heat tape was attached around the tubing as shown in Figure 3.19, to shift the fluid phase behavior to single-phase gas at a higher temperature. This approach showed a considerable improvement, as shown in Figure 3.20.
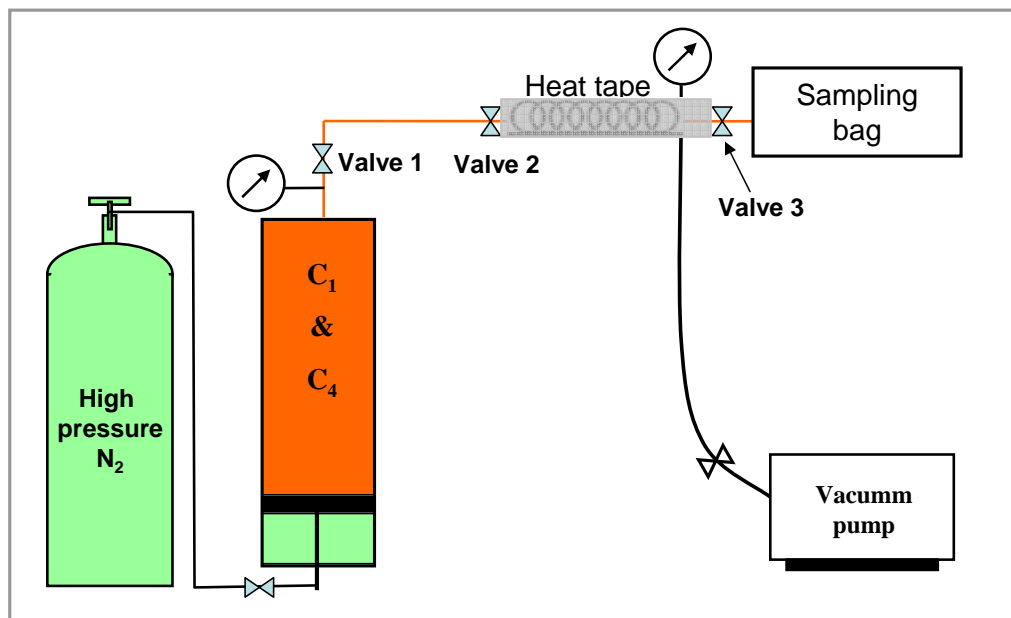
Figure 3.19: Schematic of gas sampling directly from the cylinder with heat tape.

3.3.4   Composition Analysis

Sample compositions were analyzed by gas chromatography. In the GC analysis, samples were injected manually into the GC column. There were a couple of issues associated with the manual injection process.

Before the GC analysis, we needed to check the septum. The recommended inlet septum is 11mm septum with partial through-hole and low-bleed (Part no. 51813383). First we needed to check if the septum is contaminated and whether the septum hole is closed. In either case, the septum was replaced. When the instrument is in steady use, a daily septum replacement is recommended. Secondly, it was necessary to check that the needle support assembly is installed correctly. Next, we needed to check that the correct insert is installed and that it is installed correctly. Finally, we checked the alignment of the inlet septum and the septum nut, tightening the septum nut finger tight. If the septum nut is tightened too much, it prevents the needle going through; on the other hand, a loose septum nut will reduce the peak height, and hence the analysis reproducibility. To the extreme extent, a loose septum end will cause leaks
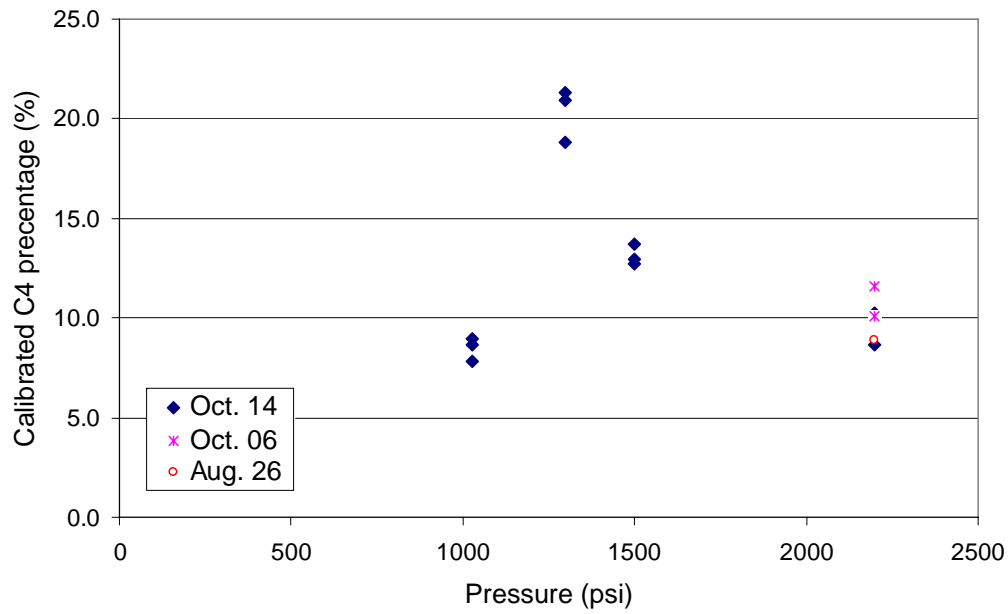
(a) Without heat tape.
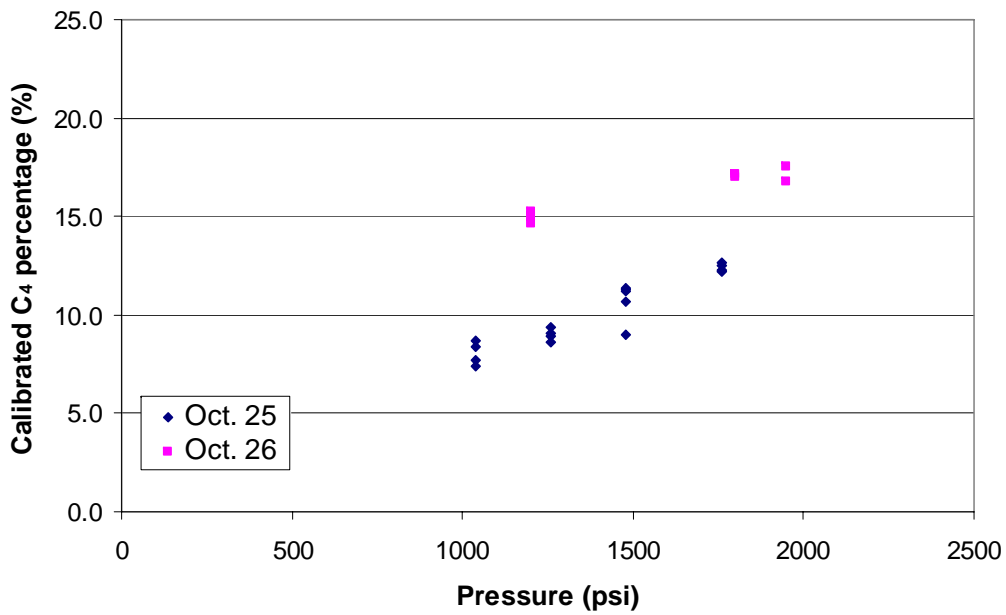
(b) With heat tape.

Figure 3.20: Composition measurement with and without using the heat tape. (*a*) without using heat tape (*b*) with heat tape.

in the septum. In this case, we will see symptoms such as longer or shifting retention times, loss of response, and/or loss of column head pressure. Additionally, signal noise will increase.

The second part needing to be checked was the syringe needle. The useful lifetime of septa depends upon injection frequency and needle quality; burrs, sharp edges, rough surfaces, or a blunt end on the needle decreases septum lifetime and may cause clogging by a septum crumb in the needle. For manual injection, the syringe plunger should be moved up and down with the needle in the sample to expel air and improve reproducibility.

Before the composition analysis, two blank runs are recommended to flush away possible leftover gases from any previous experiment run.

3.3.5   X-ray Saturation analysis

According to Akin and Kovscek (2003), a single energy scan is sufficient to measure two-phase saturations as shown in Eq. 3.7.

$$\mu_{glr} = (1 - \phi)\mu_r + \phi S_l \mu_l + \phi S_g \mu_g \tag{3.7}$$

where the subscript glr refers to rock containing both gas and liquid phases. Here, μ_r, μ_g and μ_l are the attenuation coefficients for the rock matrix, when the core is fully saturated with gas and liquid respectively and S_g and S_l are gas and liquid saturations respectively. $S_g + S_l = 1$. The CT number is defined by normalizing with the linear attenuation coefficients of water, μ_w, as shown in Eq. 3.8

$$CT = 1000\frac{\mu - \mu_w}{\mu_w} \tag{3.8}$$

The porosity, ϕ, is defined as Eq. 3.9:

$$\phi = \frac{CT_{lr} - CTar}{CT_l - CT_a} \tag{3.9}$$

where the subscripts l and a represent liquid-phase and air-phase CT numbers, whereas lr and ar refer to liquid- and air-saturation rock respectively. Thus, the saturation of gas in each voxel is defined as:

$$S_g = \frac{CT_{lr} - CT_{gr}}{CT_{lr} - CT_{glr}} \tag{3.10}$$

Thus to calculate the two-phase saturation, we need to have three parameters: CT_{lr}, CT_{gr}, and CT_{glr}. Due to the difficulty of discharging the hydrocarbon exhaust in the CT room, the three parameters were measured separately. The core saturated with liquid butane at 40 psi and gaseous methane at atmosphere pressure was first scanned and after the flow test experiment, the isolated core filled with mixture at high pressure was then taken to the CT room to measure CT_{glr}. Fluid density, especially gas density, normally changes with pressure, and according to Vinegar and Wellington (1987), the linear attenuation coefficient is expressed as:

$$\mu = [\sigma(E) + b\bar{Z}^{3.8}/E^{3.2}]\rho \tag{3.11}$$

where $\sigma(E)$ is the Klein-Nishina Coefficient, ρ is the electron density, $\bar{Z}$ is the effective atomic number, E is the photon energy in keV, and b is a constant. Eq. 3.11 shows that fluids with greater density have greater linear attenuation coefficient. The CT_{lr} and CT_{gr} were measured at relatively very low pressure (40 psi for the core saturated with liquid butane, and atmosphere pressure for the core saturated with gaseous methane), hence pressure adjustment for fluid density is needed to ensure that CT_{lr} and CT_{gr} are measured/calculated at the same pressure as the high mixture pressure. Due to the relatively small compressibility, we can assume that the sandstone matrix density and the pore volume does not change with pressure, thus the change in the μ_r is mainly due to the change of fluid in the pore space.

$$\Delta\mu_{fr} = \mu_{fr(p)} - \mu_{fr(ref)} = \phi[\mu_{f(p)} - \mu_{f(ref)}] \tag{3.12}$$

where μ_{fr} is the attenuation coefficient for the core saturated with fluid f, and $\mu_{f(p)}$

is the attenuation coefficient for fluid f at pressure p, and $\mu_{f(ref)}$ at reference measurement pressure.

According to Eq.3.11, for the same fluid, we have:

$$\frac{\mu_{f(ref)}}{\rho_{f(ref)}} = \frac{\mu_{f(p)}}{\rho_{f(p)}} \tag{3.13}$$

The change of CT number for the core saturation with fluid f due to the change of density in the fluid is, therefore, given by:

$$\Delta CT_{fr} = CT_{fr(p)} - CT_{fr(ref)} = 1000\frac{\Delta\mu_{rf}}{\mu_w} \tag{3.14}$$

substitute Eq. 3.12 and Eq. 3.13 into En.3.14, then Eq. 3.14 can be written as:

$$\Delta CT_{fr} = 1000\phi\frac{(\frac{\rho_{f(p)}}{\rho_{f(ref)}} - 1)\mu_{f(ref)}}{\mu_w} \tag{3.15}$$

Divide ΔCT_{fr} by $CT_f(ref)$, we can get:

$$\frac{\Delta CT_{fr}}{CT_{f(ref)}} = \phi\frac{(\frac{\rho_{f(p)}}{\rho_{f(ref)}} - 1)\mu_{f(ref)}}{\mu_{f(ref)} - \mu_w} \tag{3.16}$$

Rearrange Eq. 3.16, then the final ΔCT_{fr} is given by:

$$\Delta CTfr = CT_{f(ref)}\phi(\frac{\rho_{f(p)}}{\rho_{f(ref)}} - 1)(1 + \frac{1000}{CT_{f(ref)}}) \tag{3.17}$$

Eq. 3.17 tells us that the change in CT number due to the density change for the same fluid can be adjusted if the fluid density at pressure p and at the reference pressure are both known, and CT numbers for the fluids themselves at the reference measurement condition are also available. Table 3.3 shows the density of the liquid butane and the vapor methane at reference pressure and a pressure of 2000 *psi*. The density of the liquid butane and the density of the vapor methane at other pressures can be calculated from correlations given in Figure 3.21 and Figure 3.22 respectively.

Figure 3.23 shows the nine scanning positions. The positions were chosen carefully to avoid the ports and fittings along the core holder. The start and end scanning
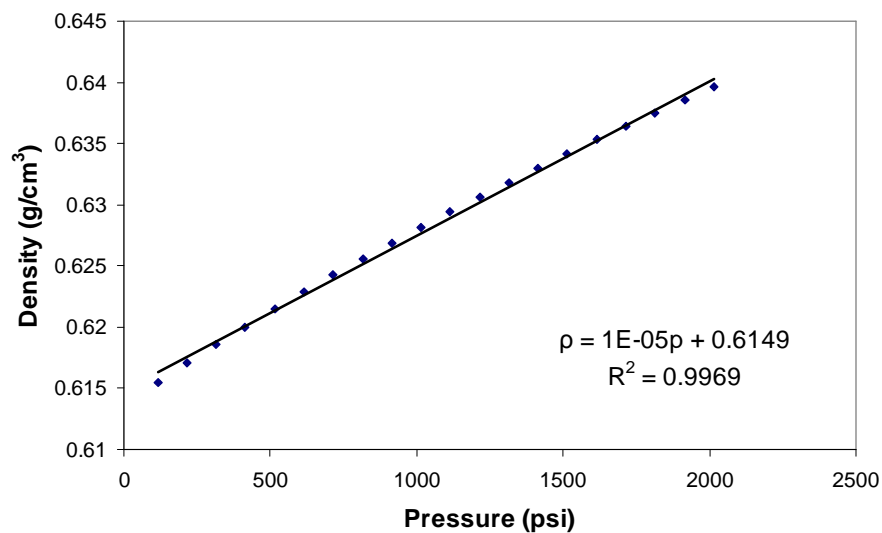
Figure 3.21: Butane density as a function of pressure.
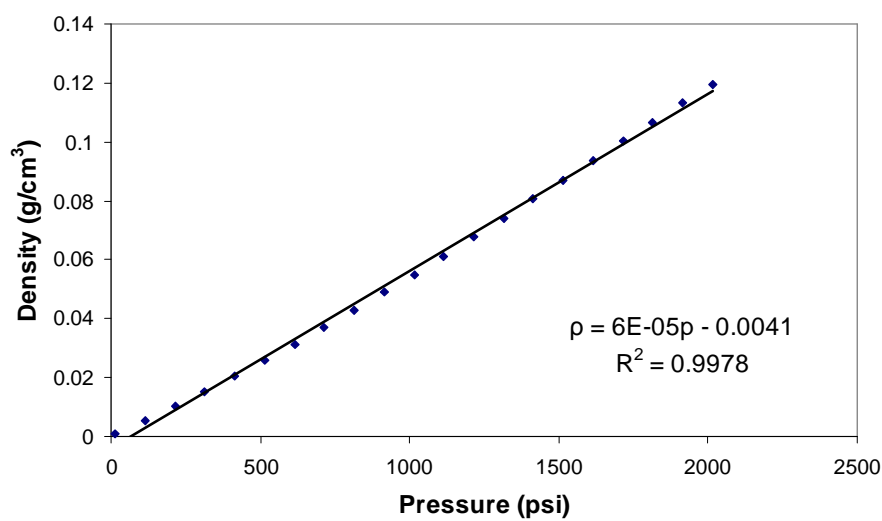
Figure 3.22: Methane density as a function of pressure.

Table 3.3: Parameters for CT number calculation.

$\rho_{C_4(ref)}$	$\rho_{C_4(2000)}$	$\rho_{C_1(ref)}$	$\rho_{C_1(2000)}$	$CT_{C_4(ref)}$	$CT_{C_1(ref)}$
(g/cm^3)	(g/cm^3)	(g/cm^3)	(g/cm^3)	(liquid)	(vapor)
0.6	0.6394	0.000717	0.1159	-285	-1000
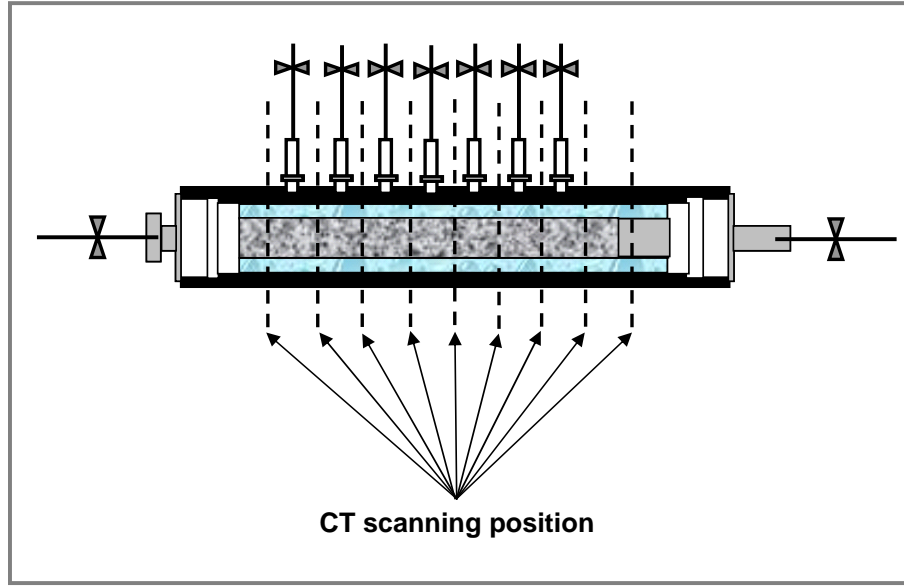
Figure 3.23: Apparatus for x-ray CT scanning.

position were labeled on the core holder, and all scans were started from the same position and ended at the same location. Hence, for each scanning location, CT_{lr}, CT_{gr}, and CT_{glr} were ensured from exactly the same slice.

The images files from the CT room were transferred to the local computer and postprocessed with Matlab. Figure 3.24(a) shows the whole image of the core with the core holder. In saturation calculation, we are interested in the CT numbers of the core only. So the image of the core (as shown in Figure 3.24(b)) was extracted from the original image and only the CT numbers of the core were used for saturation calculation.

(a) CT image with core holder   (b) CT image of the core only
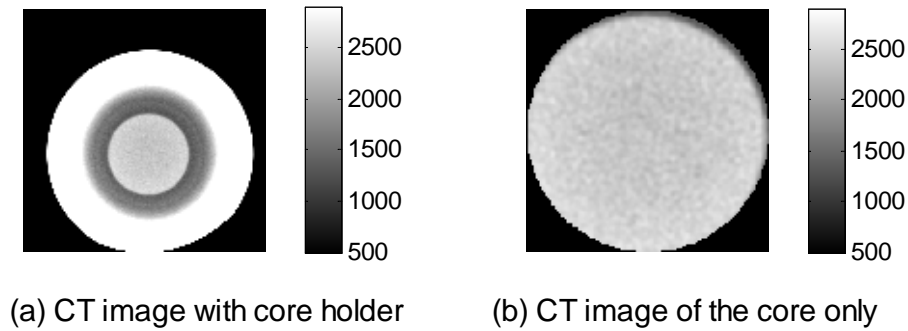
Figure 3.24: CT image processing.

3.4   Summary

Experimental equipment was constructed to allow detailed and accurate measurements of real time pressure and in situ composition of the flowing fluid along the core. This apparatus was used to do constant pressure-drop core flooding experiment and the isolated coreholder was taken to the X-ray CT room for saturation measurements.

Chapter 4

Experimental Results

The results from the experiment are discussed in this chapter. The pressure data, compositional data and also the saturation data are analyzed and presented here. These results help in understanding of gas-condensate flow in porous media.

4.1 Experimental Results

4.1.1 Pressure Measurements

Experiment A

Figure 4.1 shows the pressure profiles for Experiment A. At the first sampling stage, the core was saturated with the gas-condensate fluid of methane and butane at a pressure of 1,956 psi. Due to the sudden pressure drop during the sampling process, the actual sampling pressures are different from the baseline 1,956 psi, as depicted by the pink square dots in Figure 4.1(a). From this figure, we can see that samples collected at port 1, port 2, port 3 and port 5 are roughly at the same pressure of 1865 psi, which is above the dewpoint pressure (1837 psi), while the sampling pressures at port 4 and port 6 are lower than the dewpoint pressure.

Sampling during the flow also showed pressure drop in all ports, the biggest instantaneous pressure drops occurred at port 1 and port 5 due to the long sampling time. The influence of pressure drop on the compositional results will be discussed in

the next section.

Experiment B

Figure 4.2 illustrates the pressure results for constant pressure drop flow experiment B. During this experiment, the sampling process was meticulously operated, consequently, the sampling pressure did not drop as severely as in Experiment A.

Experiment C

Figure 4.3 shows the pressure measurements from Experiment C. Different from Experiments A and B, the flow samples in Experiments C and D were collected when the core was in "capture" status instead of in flowing condition. "Capture" refers to the status in which both the upstream and downstream of the flow were shut, and the flow in the core was immediately isolated. Samples from the "capture" status were collected immediately after the flow cut. "Capture" mode was designed to try to sample the in-situ (static) composition, instead of flowing composition measured in flow mode in Experiments A and B. Fluid samples collected from the tubing in the downstream of the core were usually contaminated by the fluid from the core. The "capture" design helped to get the true sample right after the core flow. However, samples collected from the core were slightly altered even though sampling was done in 3-4 seconds after the "capture". Because of the small volume of the core, pressure in the core tended to reach balance immediately after the external flow was shut down. Sampling pressures, as shown in Figure 4.3(a), display a near uniform distribution, which confirms the instant pressure redistribution.

The buildup pressures in Figure 4.3(a) were measured shortly after the core sampling. Due to the small volume of core, the fluid redistributed in the core very quickly and the pressure reached a steady-state condition very soon at 1570 *psi*. Pressure in the core went down to 71 *psi* after the fluid in the core was fully discharged to an empty piston cylinder.
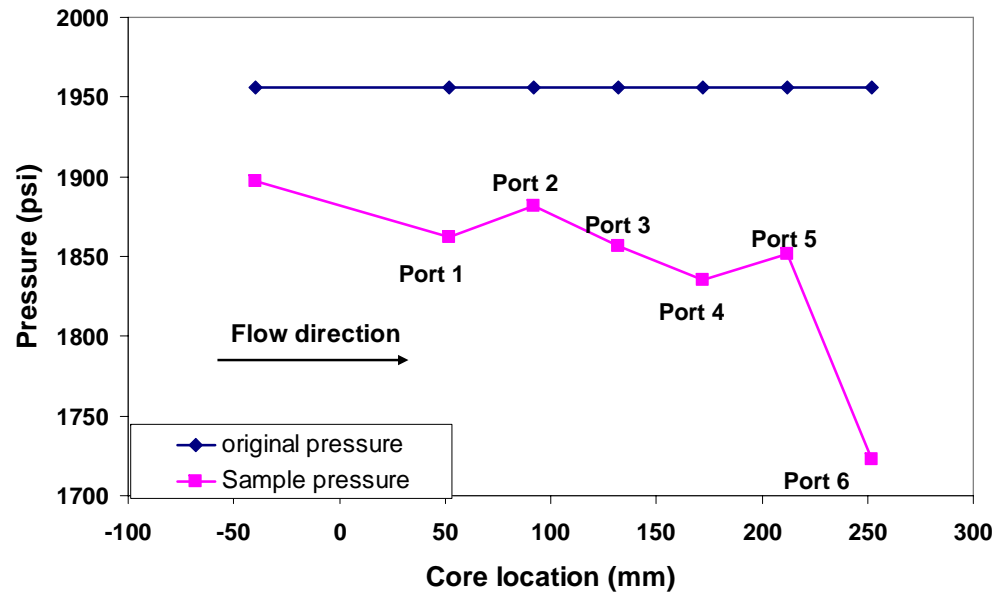
(a) Sampling without flow.
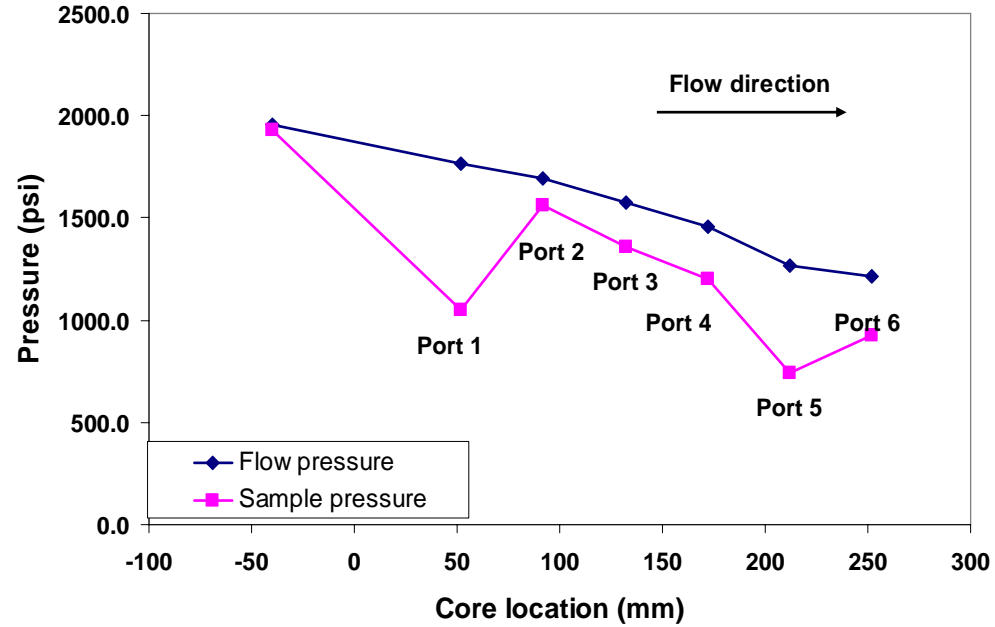
(b) Sampling during flow.

Figure 4.1: Sampling pressure profiles for Experiment A. (*a*) Sampling without flow (*b*) Sampling during flow.
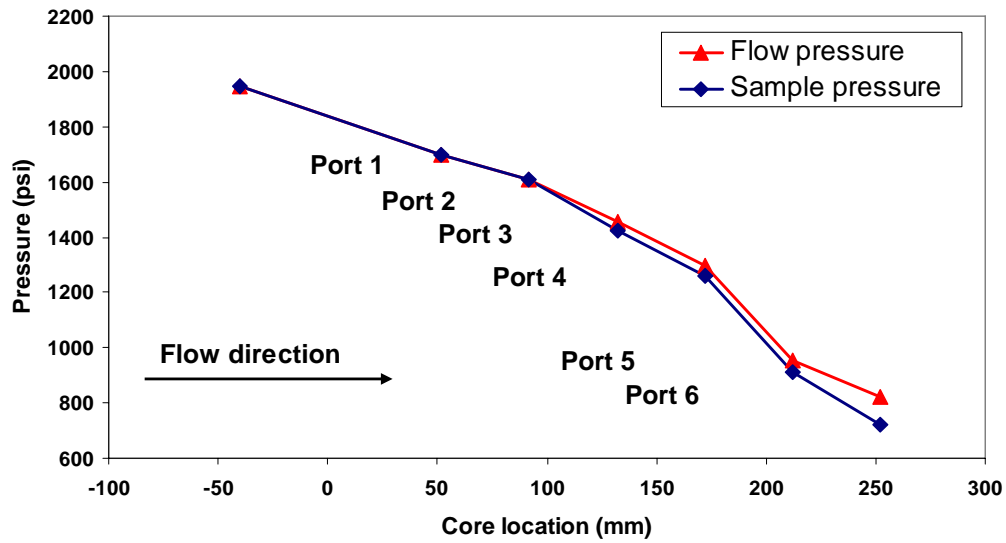
(a) Sampling during flow.
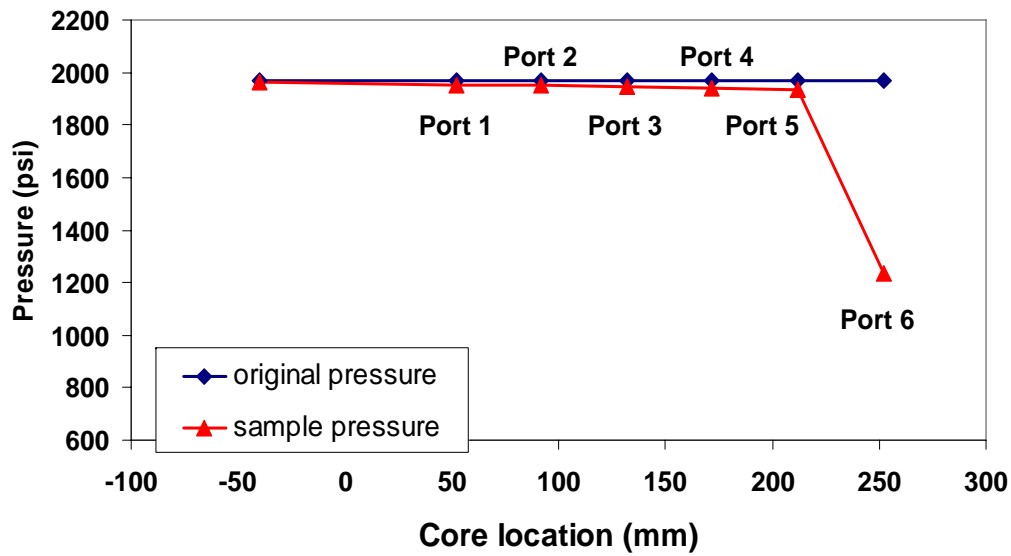
(b) Sampling without flow.

Figure 4.2: Sampling pressure profiles for Experiment B. (*a*) Sampling during flow (*b*) Sampling without flow.
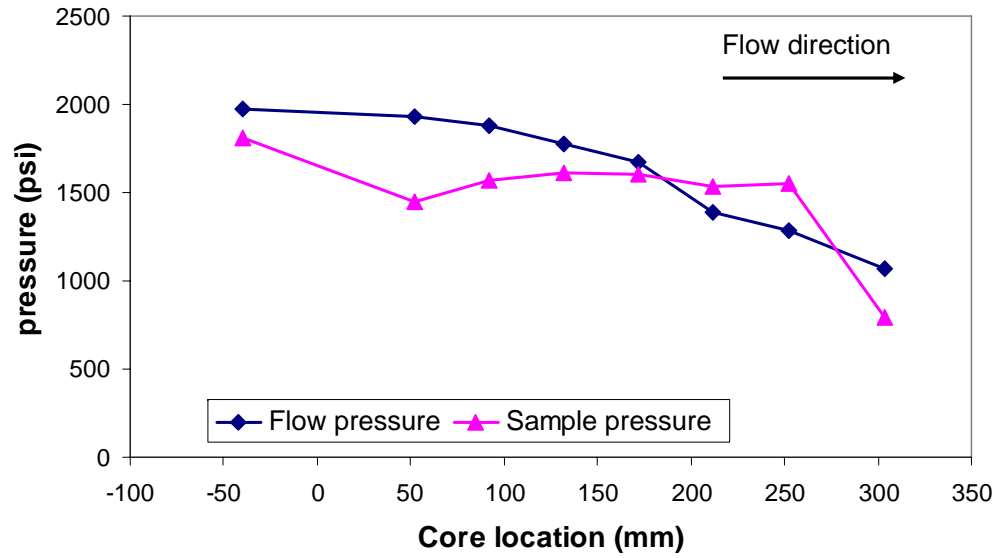
(a) Sampling after shutdown.
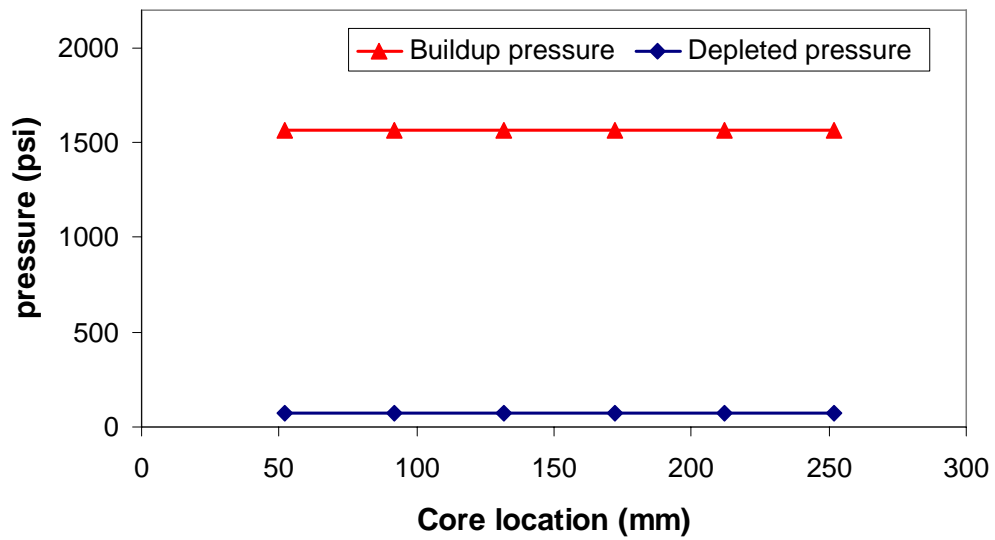
(b) Build up pressure.

Figure 4.3: Pressure profiles for Experiment C. (*a*) Flowing and sampling pressure profiles (*b*) Build-up pressure and the static pressure in the fully discharged core.

Experiment D

Figure 4.4 shows the pressure measurements from Experiment D. Experiment procedure in the first part of Experiment D was similar to that used in Experiment C. Sampling pressure in Experiment D (Figure 4.4(a)) also suggests a near uniform distribution due to the fluid and pressure redistribution. The buildup pressure in Experiment D is 1312 psi, 258 psi below the buildup pressure in Experiment C. This maybe due to the difference in the sampling time. We tried to collect the samples along the core as quickly and simultaneously as possible, but a few seconds of sampling difference still occurred among the six samples.

Comparison with Nitrogen Flow

In the previous four subsections, the flow pressure, sampling pressure and buildup pressure (if applicable) were discussed. To further understand the information behind those pressure data, we performed two additional flow experiments with nitrogen under similar pressure settings. Pressure profiles from the single-phase nitrogen flow were then compared with the hydrocarbon flow. Figure 4.5 shows the pressure profile comparison. Three hydrocarbon experiments, Experiment A, B and D, show greater pressure drop at core locations close to upstream, this reveals two-phase flow in the core since two-phase flow has lower mobility, and hence greater pressure gradient. Experiment C, however, only show an increased pressure gradient at core location from 50 mm and 100 mm. At core location from 100 mm to 175 mm, the pressure gradient is smaller than the corresponding nitrogen flow at the same location. This abnormal pressure distribution may due to measurement error in the pressure transducers or unusual flow activity.

Apparent permeability was calculated for both single-phase nitrogen flow and also for four hydrocarbon experiments. The apparent permeability for compressible flow is defined as Eq. (4.1):

$$k = \frac{Q}{A} \cdot \frac{2\mu L p_0}{p_i{}^2 - p_0{}^2} \tag{4.1}$$

where Q is the volumetric flow rate, μ, the fluid viscosity, L, the flow distance and p_i
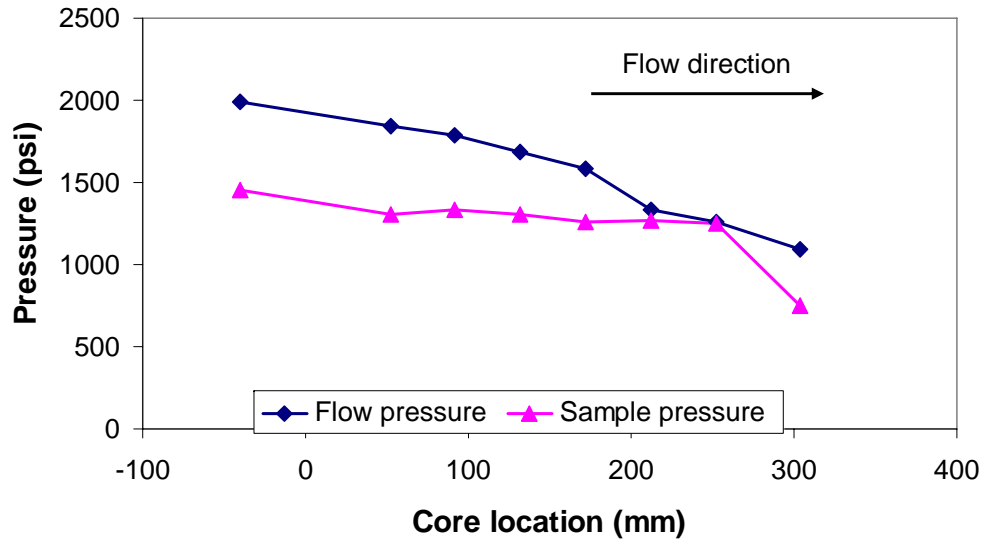
(a) Sampling after shutdown.
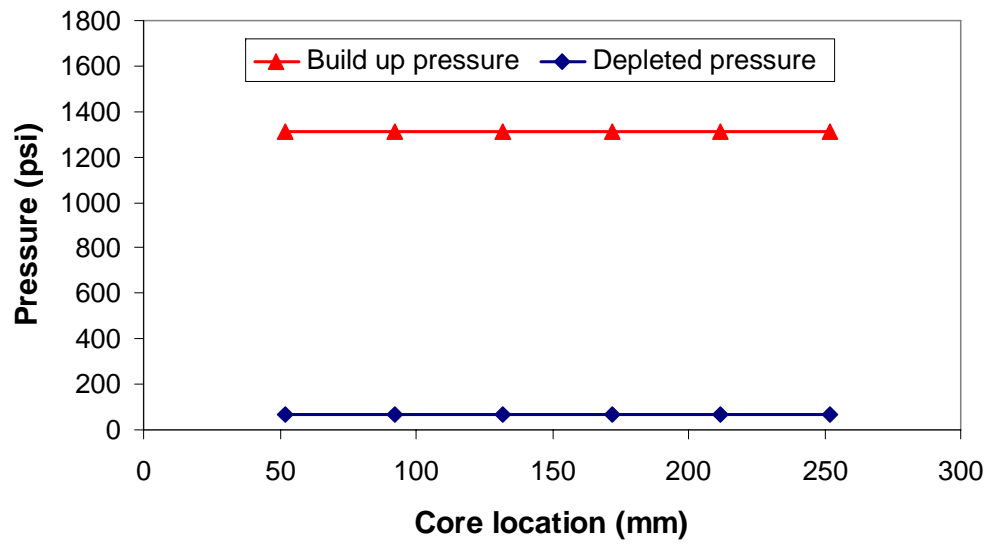
(b) Build up pressure.

Figure 4.4: Pressure profiles for Experiment D. (*a*) Flowing and sampling pressures (*b*) Build-up pressure and pressure in the fully discharged core.
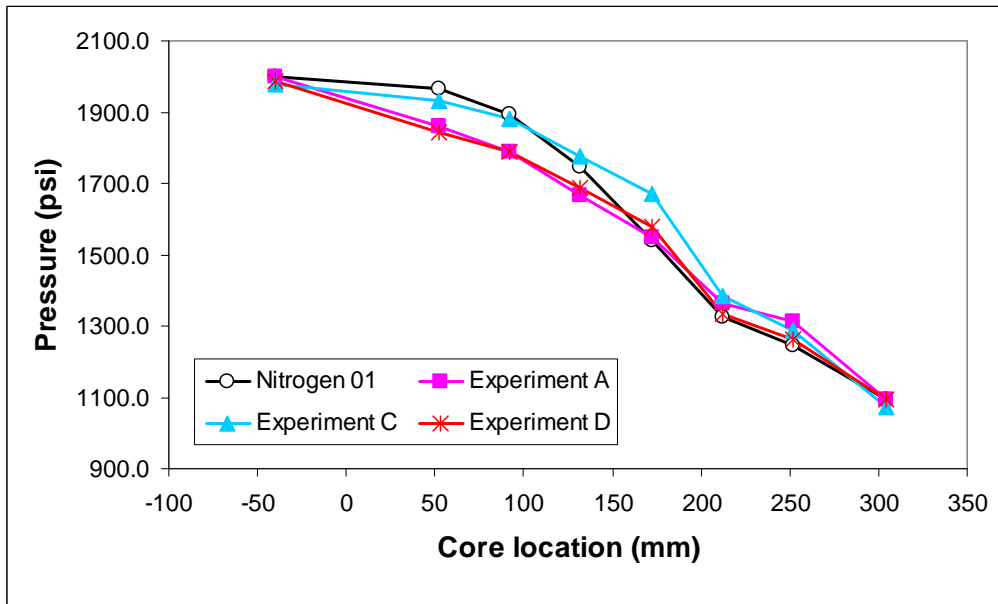
(a) Pressure profile comparison of nitrogen flow run 1 and hydrocarbon Experiment A, C and D.
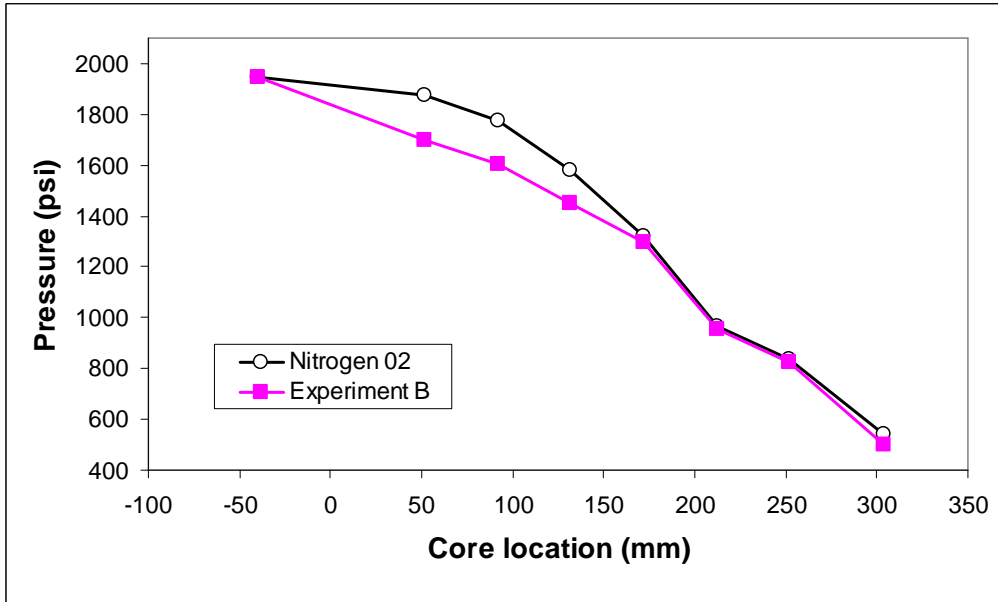
(b) Pressure profile comparison of nitrogen flow run 2 and hydrocarbon Experiment B.

Figure 4.5: Pressure profile comparison of nitrogen flow and hydrocarbon flow. (*a*) Comparison of nitrogen flow run 1 and hydrocarbon Experiment A, C and D. (*b*) Comparison of nitrogen flow run 2 and hydrocarbon Experiment B.

and p_0, the upstream pressure and reference pressure respectively.

An average density of the liquid and the vapor density was used for two-phase hydrocarbon flow and the vapor viscosity was used for hydrocarbon viscosity calculation. Since flow rate measurements are not available in this study, a relative apparent permeability k_i/k_{ref} is adopted for comparison. k_i/k_{ref} is calculated as:

$$\frac{k_i}{k_{ref}} = \frac{\mu_i p_0}{(p_i^2 - p_0^2)\rho_i} / \frac{\mu_{ref} p_0}{(p_{ref}^2 - p_0^2)\rho_{ref}} \tag{4.2}$$

where k_i is the apparent permeability at location i, and k_{ref} is the apparent permeability at the reference location.

Figure 4.6 shows the density and the viscosity profiles as functions of pressure for nitrogen. The average density and vapor viscosity of the methane-butane system ($C_1/C_4 = 85\%/15\%$) at $T = 20°C$ were calculated with WinProp (version 2006, Computer Modeling Group Ltd., PR(1978) EoS), as displayed in Figure 4.7. Nitrogen density bears a straight correlation with pressure, and shows lower density at high pressure than the methane-butane mixture. In general, nitrogen viscosity has a narrower variation from 0.017 cp to 0.0214 cp, however, the vapor viscosity for methane and butane mixture varies from 0.01 cp to 0.0251 cp. At pressure lower than the dewpoint pressure, the viscosity of the two-phase hydrocarbon flow should have greater value than the vapor viscosity used in the calculation. Hence the k_i/k_{ref} calculation for hydrocarbon flow at low pressure could be underestimated.

Figure 4.8 shows the calculated k_i/k_{ref} for both nitrogen flow and four hydrocarbon experiments. Compared with the nitrogen flow, the hydrocarbon flow at the low pressure range shows decrease in the k_i/k_{ref}, which is due to the lower flow capacity in the two-phase flow region.

4.1.2 Compositional Measurements

Experiment A

In this experiment, the first batch of samples (we call them original compositions) were collected before the flow test, and the core was in static condition during sampling.
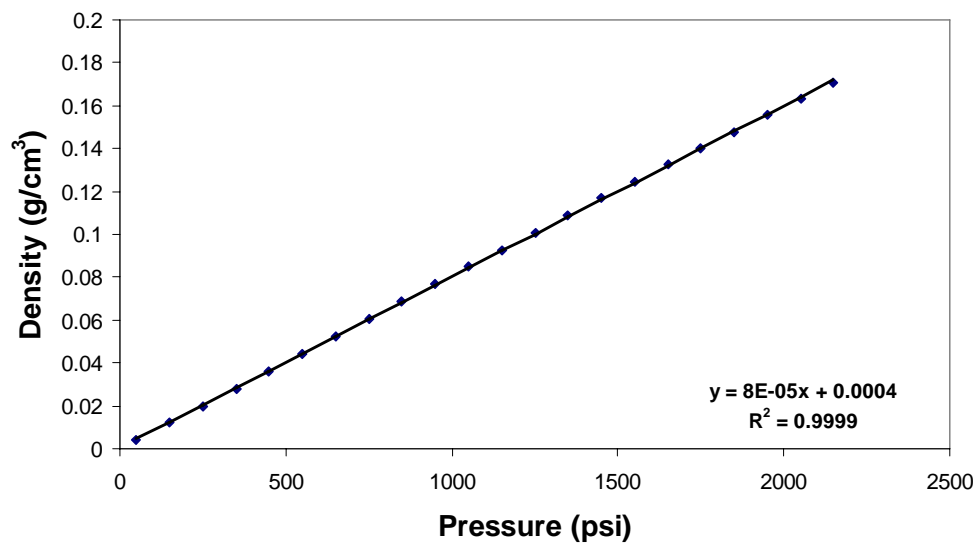
(a) Density of nitrogen.
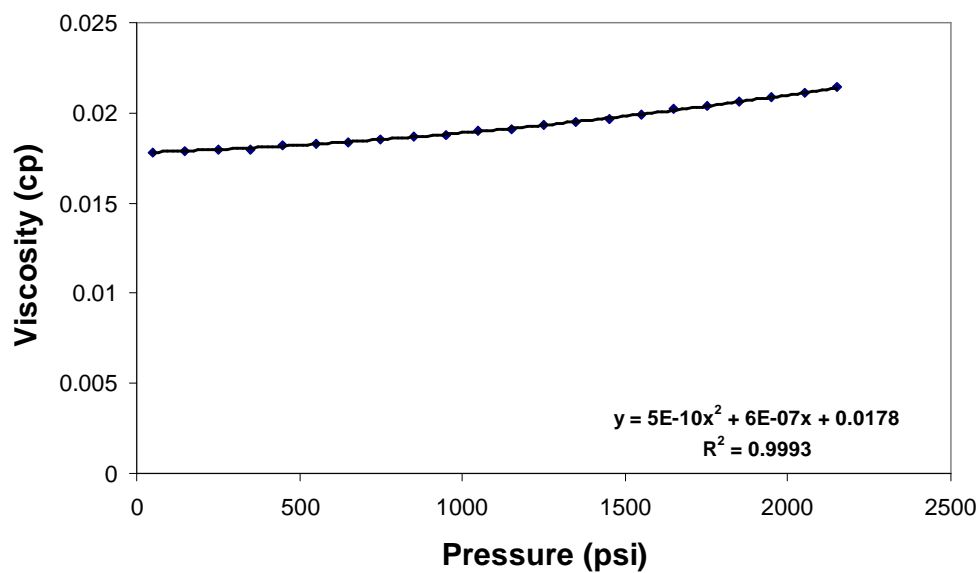
(b) Viscosity of nitrogen.

Figure 4.6: Density and viscosity of nitrogen at $T = 20°C$ (a) Density vs. Pressure (b) Viscosity vs. Pressure.
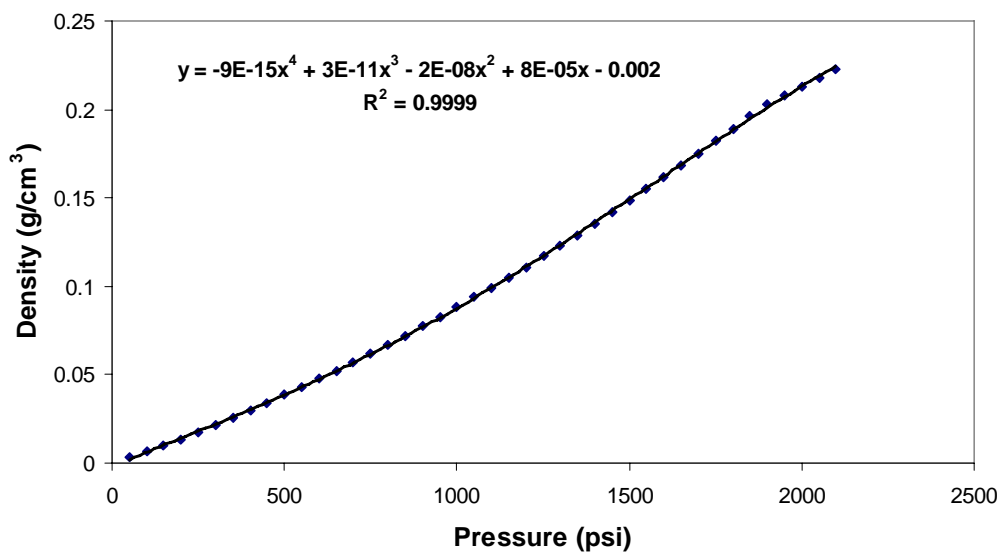
(a) Density of methane and butane mixture ($C_1/C_4 = 85\%/15\%$).
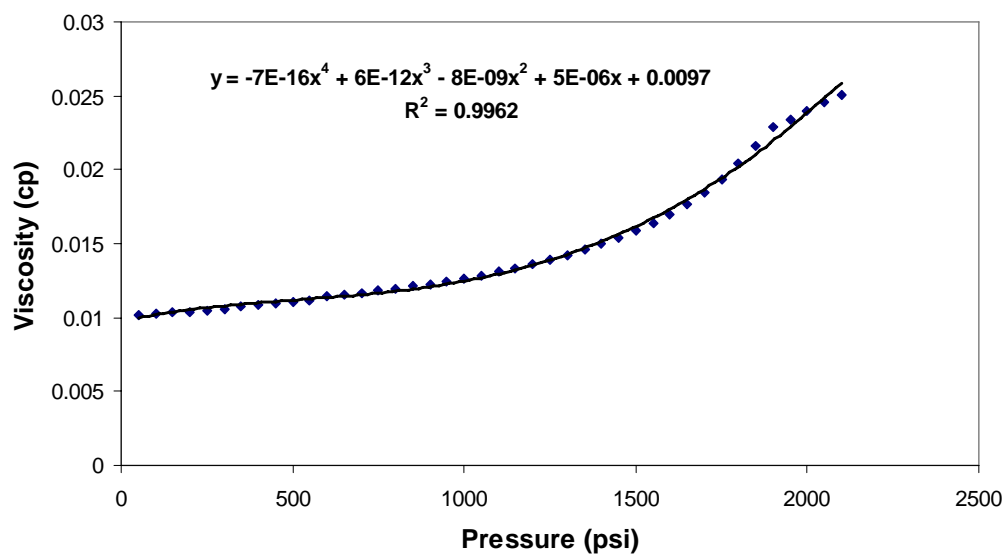
(b) Viscosity of methane and butane mixture ($C_1/C_4 = 85\%/15\%$.

Figure 4.7: Density and viscosity of methane and butane mixture ($C_1/C_4 = 85\%/15\%$) at $T = 20°C$ (*a*) Density vs. Pressure (*b*) Viscosity vs. Pressure.
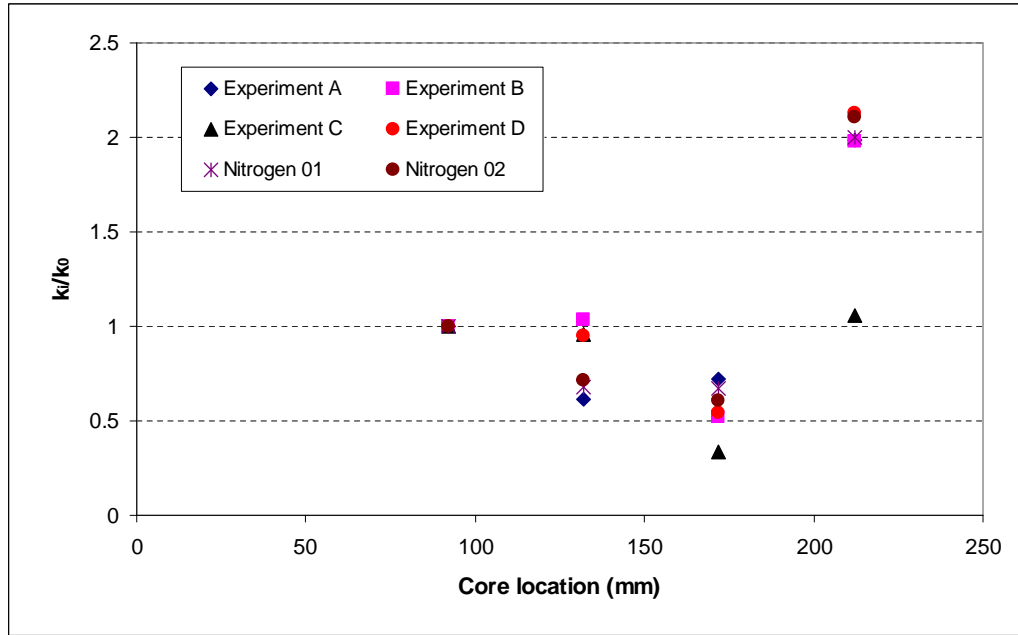
Figure 4.8: Apparent permeability ratios for nitrogen and hydrocarbon flow (k_i/k_1, scaled with the apparent permeability at location $90mm$.).

Notice that, the original compositions (blue diamond dots in Figure 4.9) show slight drop in the butane mole percentage at the two sample ports located downstream. Compositions from the four upstream ports are identical and consistent with the composition from the cylinder. The drop of butane mole percentage in the last sampling ports may be due to the pressure drop during the sampling process or due to liquid dropout during the initial introduction of the mixture into the empty core.

The flow test was performed under constant pressure drop with the upstream and downstream pressures were regulated to 1,954.1 psi and 1,000 psi respectively. The second batch of samples were taken during the steady constant pressure drop flow. The composition results in Figure 4.9 show that as the pressure drops, the molar fraction of the heavy component C_4 also decreases. This is due to the fact that as the pressure decreases, liquid drops out into the core, and the accumulated liquid remains immobile until the liquid saturation exceeds the critical condensate saturation (Scc). Since the liquid is mainly comprised of the heavy component, the liquid becomes richer
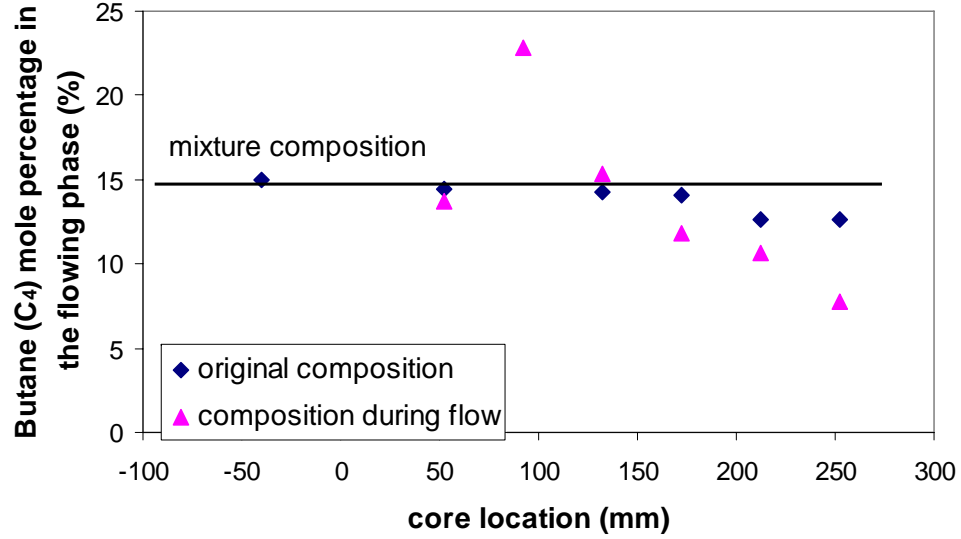
Figure 4.9: Butane mole percentage profiles with samples collected in Experiment A during flow with constant pressure drop.

as the pressure decreases. At the early stage of the flow, the flowing phase becomes leaner as the system had not reached the steady-state condition. This confirms the presimulation results as depicted previously in Figure 3.4(a).

Experiment B

Experiment B was similar to Experiment A except that it was performed under larger constant pressure drop. In this experiment, the compositional sampling during the flow was taken when the flow reached fully steady state, hence the flowing compositions are almost identical to those from static condition (as shown in Figure 4.10). This also verifies the preexperiment simulation estimation.

Experiment C

Experiments C and D were designed for two purposes. The main purpose was to isolate both the tubing lines at core ends, and thus the fluid sampling prior to and after the core will not be influenced by the instant pressure drop during the sampling
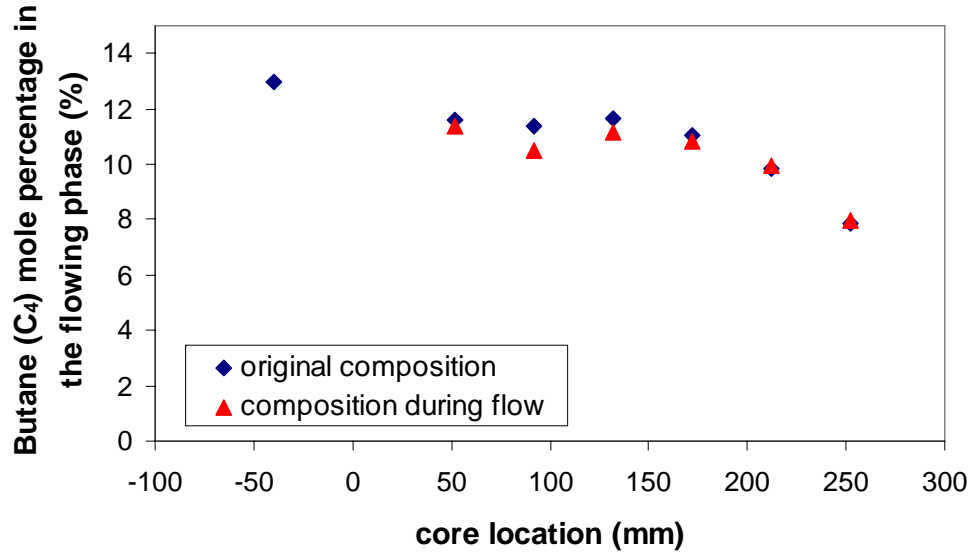
Figure 4.10: Butane mole percentage profiles with samples collected in Experiment B during flow with constant pressure drop.

process. This is especially important for the sampling at the core exit because more liquid tends to be flushed to the tubing if there is a sudden pressure drop. The second purpose is to see how quickly the composition redistributes in the core. As seen from the preexperiment simulation results, the butane mole percentage in both liquid and in-situ fluid drops in six seconds after the injector and producer shut down, at the same time the butane mole percentage in the vapor phase increases. Hence the fluid from the core at such condition becomes leaner. Figure 4.11 shows the composition results taken right after shutting down both the upstream and the downstream flow. Composition in the tubing prior to the core and after the core shows perfect match with the original composition from the cylinder. Composition prior to the core is in gas phase, so it is identical to the composition from the cylinder. Composition in the tubing after the core is the composition in the flowing phase during the constant pressure drop flow, hence is also the same as the original composition. Compositions of fluid from the interior of the core show butane content drop. This drop is not homogenous in the core, which may due two reasons. One reason is that
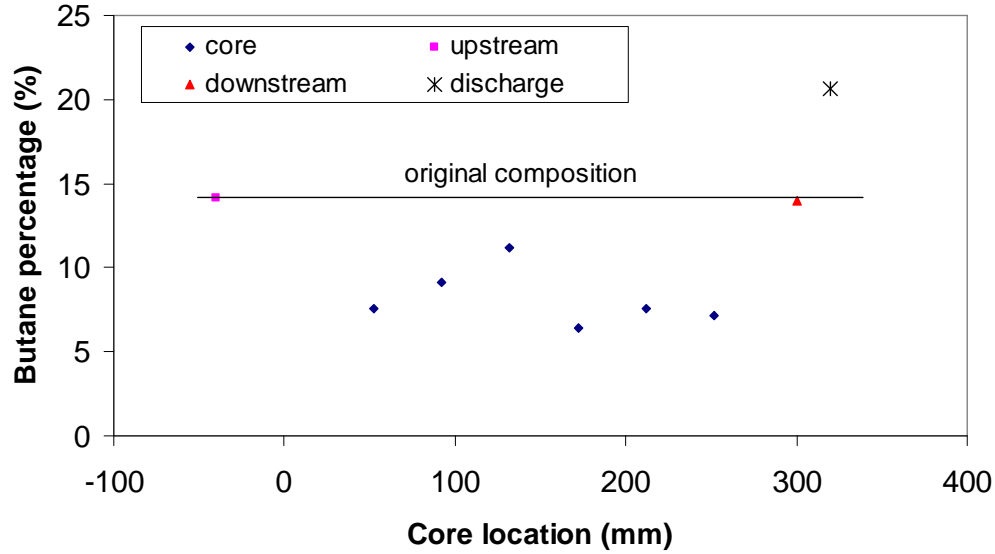
Figure 4.11: Butane mole fraction profiles with samples collected in Experiment C immediately after the flow with constant pressure drop.

the composition is not identical everywhere in the core even though the saturation redistributed in the core within very short time period. The composition configuration is still constrained by the history of the composition distribution at each core location. Another reason is that the six samples were collect by three different persons, and hence the samples were not collected at exactly the same time. The later the sampled collected, the bigger drop in the butane mole percentage.

After the flow test, the core was naturally discharged, and the fluid was collected in an empty piston cylinder. The discharging experiment measures the average composition z_i flowing in the core, which can not be sampled directly from the flowing phase during the constant pressure drop flow. The composition analysis (Figure 4.11) shows increase of butane mole percentage in the fluid, which further confirms that the in-situ fluid in the constant pressure drop flow became heavier.

Experiment D

Experiment D is similar to Experiment C except that the mixture used for the flow test is heavier. Similar conclusions are found in Figure 4.12. In Experiment D, the composition collected from the tubing after the core shows increase in the butane mole percentage. This is due to the reason that the downstream valves were switched off one second later than those in the upstream. This delay, although very short, still caused some liquid to be flushed out of the core. The composition of the discharged fluid also shows increase in the heavier component.

After discharging naturally, the core was flushed by nitrogen gas. Three samples were collected during the nitrogen injection. Figure 4.13 shows that butane percentage decreases as the injection proceeds in the core. At the beginning, the butane percentage is about 14%, then after three minutes, butane percentage dropped to about 2%. This demonstrates that the accumulated liquid could not fully revaporize from the porous medium once it had been trapped there, and nitrogen injection is an effective way to recover the heavy component trapped in the core.

4.1.3   Saturation Measurements

Saturation is calculated from CT numbers as defined in Eq. (3.10), and $S_l = 1 - S_g$. Figure 4.14 shows that the CT images for the core saturated with butane liquid, gas and the mixture of methane and butane. Figure 4.14(d) and Figure 4.14(e) illustrate that the differences between the CT images for core saturated with different fluids. The liquid saturation interpreted from the CT images is shown in Figure 4.15. Note that CT_{lr} and CT_{gr} were also adjusted with pressure to reflect the density change due to pressure change. Comparing the measured saturation results with the preexperiment saturation distribution (as shown in Figure 3.7), we can see that simulation and experiment behave differently in the well region. In the simulation, liquid vaporizes to zero in the well region as the build-up pressure stabilizes at 2000 psi (Figure 4.16). However, in the core flow experiment, liquid redistributes in the core one hour after the flow shut down. Although the final build up pressure is as high as 2000 psi, the liquid did not revaporize as suggested by the original phase
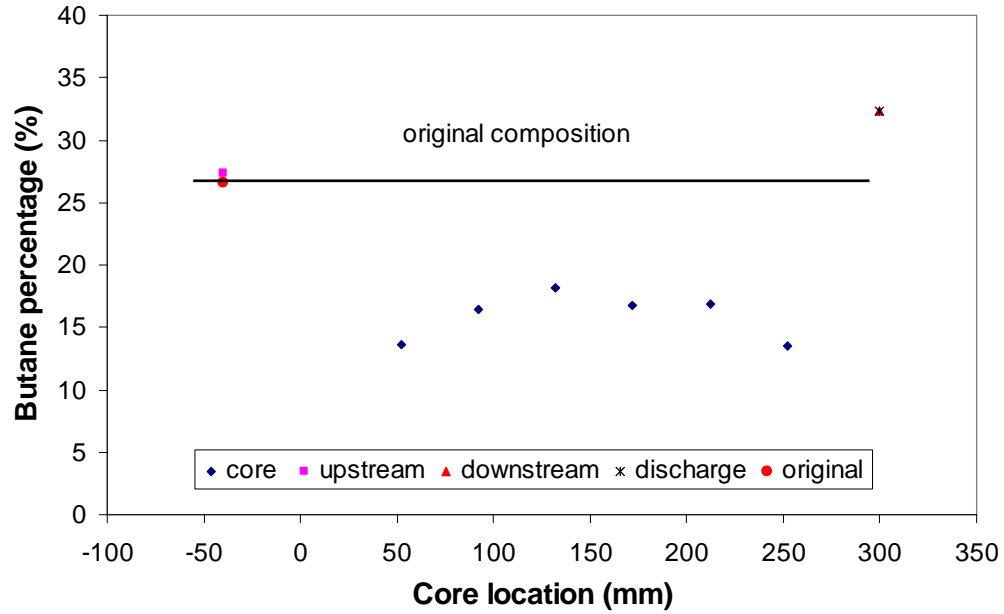
Figure 4.12: Butane mole fraction profiles with (*a*) samples collected immediately in Experiment D after the flow with constant pressure drop (*b*) Samples collected after nitrogen injection into the naturally depleted core.

diagram (Figure 3.1). This further confirms that the liquid becomes heavier (richer in heavy component), and the fluid in the core did not go back to the single gas phase at 2000 *psi* and room temperature according to the new phase configuration. The zero liquid saturation near the well region suggested by ECLIPSE simulation results is probably due to the inappropriate phase treatment in ECLIPSE. ECLIPSE treats all the regions outside the phase diagram as one single gas phase. This is true when the reservoir temperature remains on the right side of the critical temperature, and the composition configuration in the core does not change over time. However, the composition in the core becomes heavier as liquid builds up in the core, the phase diagram shifts towards the heavier configuration, and the critical temperature of the heavier fluid may shift to the right side of the reservoir temperature (as shown in Figure 4.17). In this case, the reservoir fluid is no longer gas-condensate, and hence liquid can not revaporize as the pressure goes up. In this case, repressurizing is not a good strategy to remove the liquid accumulation.
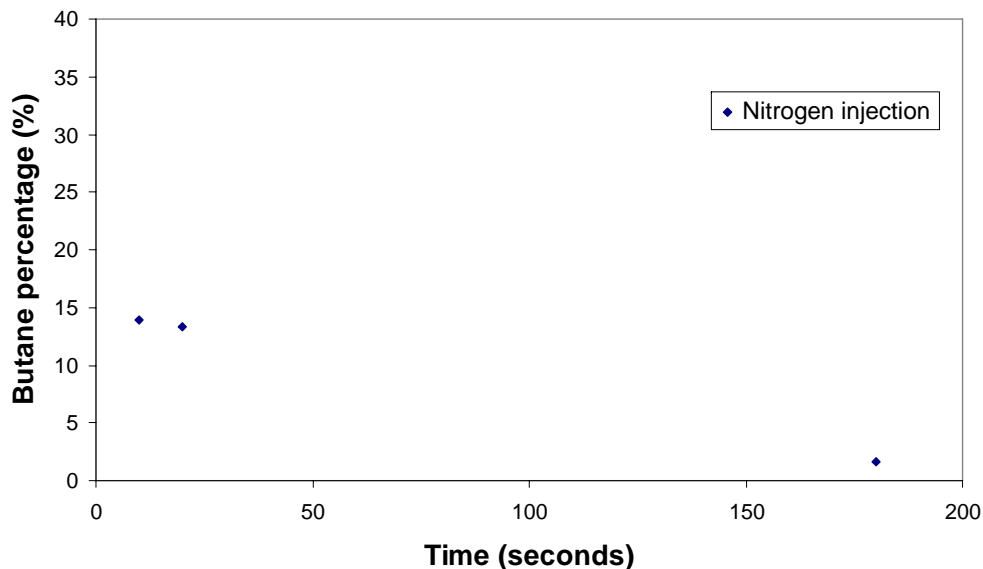
Figure 4.13: Butane mole fraction in the exit flow with nitrogen injection (Experiment D).

4.1.4   Apparent Permeability Measurements

Nitrogen permeability was measured before and after the hydrocarbon flow test. Figure 4.18 shows the results measured at different time. Where k is apparent permeability, defined as Eq. (4.1). From the figure, we can see that permeabilities measured right after the hydrocarbon flow test are lower than those measured before the test, which indicates that some liquid drop-out in the core did not revaporize. The fact that liquid still exists even though the original phase diagram suggests complete revaporization is of primary importance, because it shows that the liquid remaining in the core is not the same as the original composition. Nitrogen permeability measured two weeks after the hydrocarbon flow test is consistent with those measurements before the hydrocarbon flow test, which indicates the ultimate revaporization of the condensate in the core. These results are also consistent with the composition measurements in Experiment D.

(a) Image of the core saturated with liquid C_4.
(b) Image of the core saturated with gas C_1.
(c) Image of the core saturated with the mixture of C_1 and C_4.
(d) The difference between the core saturated with liquid C_4 and gas C_1.
(e) The difference between the core saturated with liquid C_4 and the mixture of C_1 and C_4.
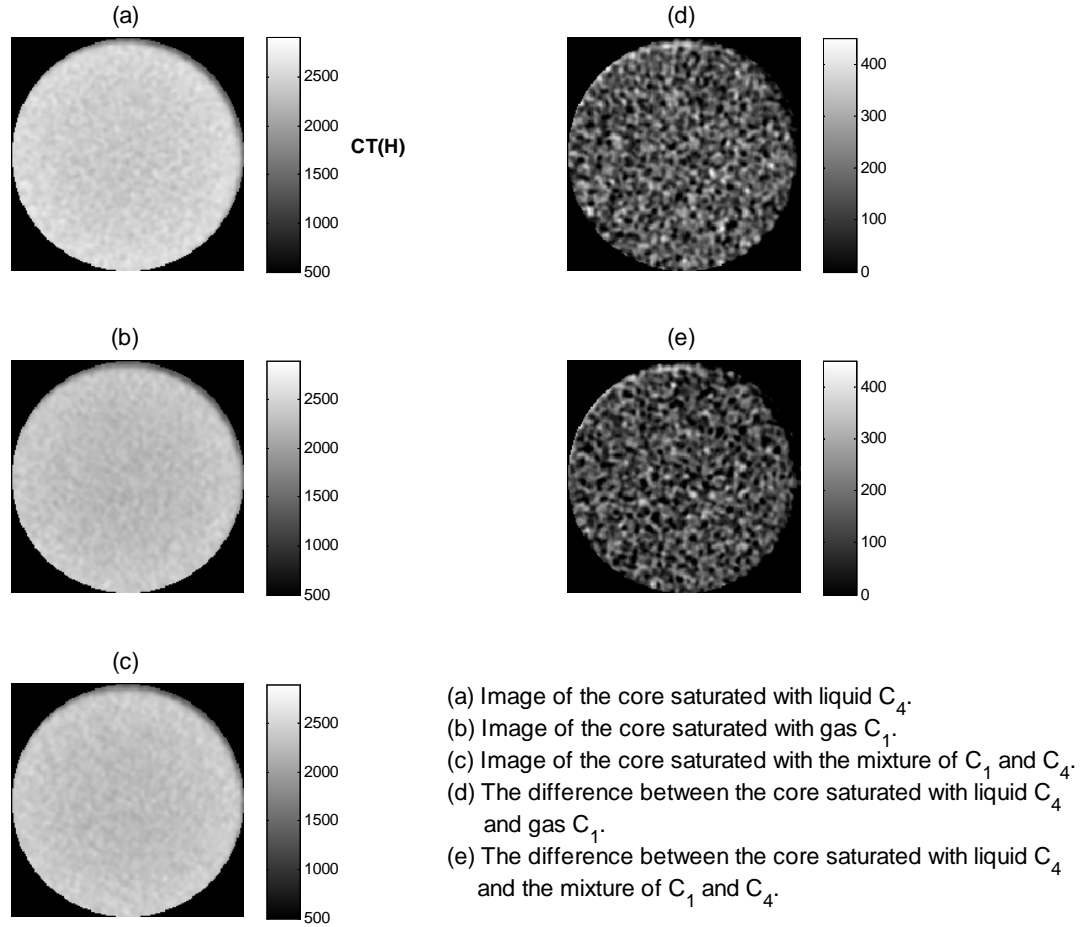
Figure 4.14: CT images of the core saturated with (a) liquid butane (b) gas methane (c) the mixture of methane and butane and (d) the difference between liquid butane and gas methane and (e) the difference between liquid butane and the mixture of methane and butane at $l = 74mm$.

4.2 Summary

These five example experiments on the binary gas-condensate system demonstrate and confirm the compositional variation in the gas-condensate flow, even in the constant pressure-drop flow case. In gas-condensate flow, local composition changes due to the influence of relative permeability effect although the composition of the flowing phase has slight or no change. The reservoir flow would not revaporize as suggested by the
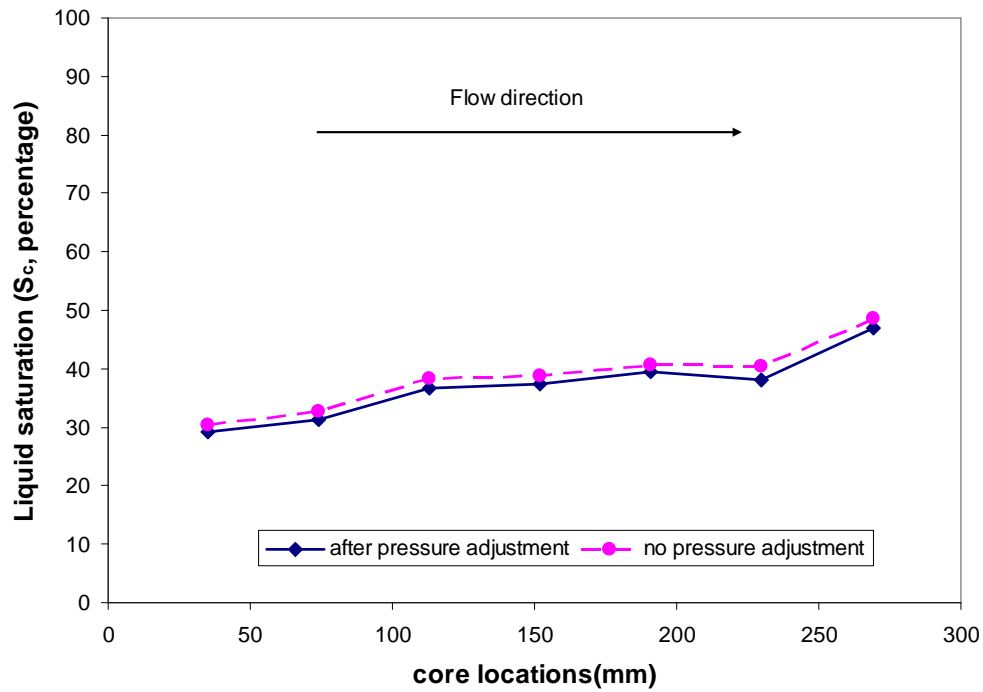
Figure 4.15: A saturation profile from CT image interpretation.
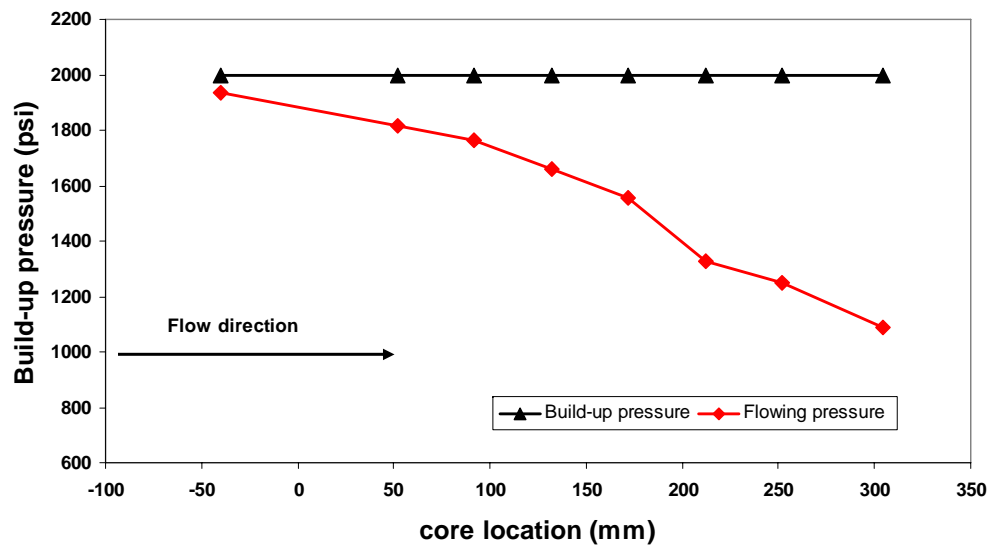
Figure 4.16: Pressure profile in the core during x-ray CT scanning.
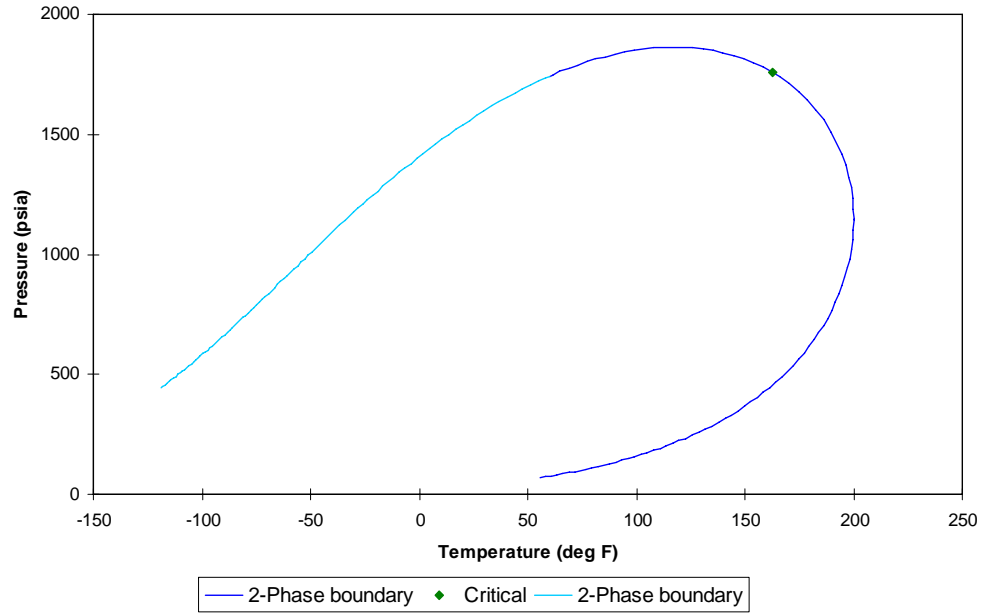
Figure 4.17: PT diagram for binary component $C_1/C_4 = 63\%/37\%$.
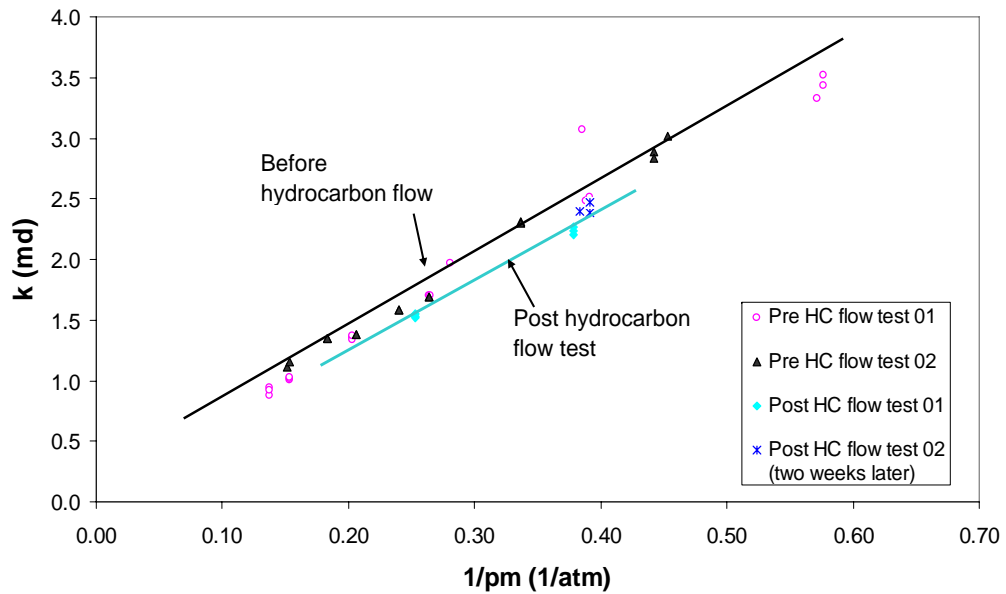
Figure 4.18: Apparent permeability measurements for nitrogen flow.

CVD experiment in the PVT cell due to the local composition variation. Pressurizing would not be a good strategy to remove the liquid accumulation in the reservoir once the fluid composition shifted to the heavier side.

Chapter 5

Gas-Condensate Flow Modeling

In this chapter, we present the general form of material balance equation for condensate flow in porous media. The compositional variation of the reservoir fluid, especially the heavier component of the fluid, around the well during condensate dropout is analyzed. Key parameters that influence the compositional behavior are also discussed in detail.

The theoretical analysis assists us to understand the mechanism of the compositional variation in the reservoir. From the theoretical material balance standpoint, we can then use our theoretical knowledge to investigate ways to enhance the productivity by producing more gas, and at the same time controlling the liquid composition that drops out around the well. In the second section of this chapter, compositional simulations are studied, and the resulting optimal producing strategies are suggested.

5.1 Theoretical Model

For an arbitrary volume, $V(t)$, of the porous medium bounded by a surface, $S(t)$, a general form of the compositional conservation equation can be defined as Eq. 5.1 if the dispersion and the effects of pressure differences between phases (capillary pressure differences) can be neglected. This assumption holds true for large capillary number cases ($N_c > 10^{-3}$), where the viscous force dominates.

Consider the experiment we studied in Chapter 4, the core is 0.25 m long with an

average permeability around 5 mD and pressure drop across the core is about 1000 to 1500 psi, the darcy velocity u is of order 1 to 1.5 cm/sec. The gas viscosity at 1800 psi is around 0.02 cp and the interfacial tension (IFT) is around 0.2 $dyne/cm$. In this case capillary number N_c is around 2×10^{-3} to 3×10^{-3} in which case the capillary and viscous forces is about the same. For gas flow with high flow rate near the well region, N_c is relatively large, hence capillary forces can be reasonably neglected, however, in cases where wells producing at low flow rate, and the interfacial tension between gas and liquid is high, the capillary force needs to be considered in the model as well.

$$\frac{\partial}{\partial t}\phi \sum_{j=1}^{n_p} x_{ij}\rho_j S_j + \nabla \cdot \sum_{j=1}^{n_p} x_{ij}\rho_j \vec{v}_j = 0, \qquad i = 1, n_c. \tag{5.1}$$

where ϕ is the porosity of the porous media, S_j is saturation of phase j, ρ_j is the molar density of phase j, x_{ij} is the mole fraction of component i in phase j, $\vec{v}_j$ is local flow velocity of phase j.

One-Dimensional Flow

For one-dimensional flow in a Cartesian coordinate system, Eq. 5.2 reduces to:

$$\frac{\partial}{\partial t}\phi \sum_{j=1}^{n_p} x_{ij}\rho_j S_j + \frac{\partial}{\partial x} \sum_{j=1}^{n_p} x_{ij}\rho_j v_j = 0, \qquad i = 1, n_c. \tag{5.2}$$

In the absence of capillary pressure and gradational force, the Darcy flow velocity, v_j, is defined by Eq. 5.3:

$$v_j = -\frac{kk_{rj}}{\mu_j}\frac{\partial p}{\partial x}, \qquad j = 1, n_p. \tag{5.3}$$

The notation of Eq. 5.2 and Eq. 5.3 can be simplified by defining two additional functions, G_i and m_i, as:

$$G_i = \sum_{j=1}^{n_p} x_{ij}\rho_j S_j \tag{5.4}$$

and

$$m_i = \sum_{j=1}^{n_p} x_{ij} \rho_j \frac{kk_{rj}}{\mu_j} \tag{5.5}$$

G_i is an overall molar density of component i, and m_i an overall mobility of component i weighted with component molar density. The final version of the equations for multicomponent, multiphase convection is, therefore,

$$\phi \frac{\partial G_i}{\partial t} - \frac{\partial m_i}{\partial x} \frac{\partial p}{\partial x} - m_i \frac{\partial^2 p}{\partial x^2} = 0, \qquad i = 1, n_c. \tag{5.6}$$

Summing up Eq. 5.6 over all components, a similar conservation equation can be obtained as:

$$\phi \frac{\partial G}{\partial t} - \frac{\partial m}{\partial x} \frac{\partial p}{\partial x} - m \frac{\partial^2 p}{\partial x^2} = 0 \tag{5.7}$$

where

$$G = \sum_{i=1}^{n_c} G_i \tag{5.8}$$

and

$$m = \sum_{i=1}^{n_c} m_i \tag{5.9}$$

Rearranging and combining Eq. 5.6 and Eq. 5.7 together, the following equation can be obtained:

$$\frac{1}{m_i} \frac{\partial G_i}{\partial t} = \frac{1}{m} \frac{\partial G}{\partial t} + \frac{1}{\phi} \frac{\partial}{\partial x} ln(\frac{m_i}{m}) \frac{\partial p}{\partial x}, \qquad i = 1, n_p. \tag{5.10}$$

ρ_j is the molar density (in moles per unit volume) of phase j. Given a volume V and a porous media with porosity ϕ, then $\rho_j V \phi S_j$ is the mole fraction of phase j, hence,

$$G_i V \phi = \sum_{j=1}^{n_p} x_{ij} V \phi \rho_j S_j = z_i \tag{5.11}$$

and

$$GV\phi = \sum_{i=1}^{n_c} G_i V\phi = \sum_{i=1}^{n_c} z_i = 1 \qquad (5.12)$$

Therefore:

$$\frac{G_i}{G} = \frac{G_i V\phi}{GV\phi} = \frac{z_i}{1} = z_i \qquad (5.13)$$

Rearranging and putting $z_i = G_i/G$ in Eq. 5.10, the final version of the equations for multicomponent, multiphase convection is, therefore,

$$\frac{\partial z_i}{\partial t} = (\frac{m_i}{m} - z_i)\frac{\partial lnG}{\partial t} + \frac{m_i}{\phi G}\frac{\partial}{\partial x}ln(\frac{m_i}{m})\frac{\partial p}{\partial x}, \qquad i = 1, n_c. \qquad (5.14)$$

Notice that G_i, G and m_i/m are functions of pressure, by applying the chain rule, Eq. 5.14 can be further expressed as:

$$\frac{\partial z_i}{\partial t} = (\frac{m_i}{m} - z_i)\frac{\partial lnG}{\partial p}\frac{\partial p}{\partial t} + \frac{m_i}{\phi G}\frac{\partial}{\partial p}ln(\frac{m_i}{m})(\frac{\partial p}{\partial x})^2, \qquad i = 1, n_c. \qquad (5.15)$$

The notation of Eq. 5.15 can be simplified by defining two additional functions, A_i and B_i, as

$$A_i = (\frac{m_i}{m} - z_i)\frac{\partial lnG}{\partial p}, \qquad i = 1, n_c. \qquad (5.16)$$

and

$$B_i = \frac{m_i}{\phi G}\frac{\partial}{\partial p}ln(\frac{m_i}{m}), \qquad i = 1, n_c. \qquad (5.17)$$

The final version of the simplified equations for multicomponent, multiphase convection is, therefore,

$$\frac{\partial z_i}{\partial t} = A_i\frac{\partial p}{\partial t} + B_i(\frac{\partial p}{\partial x})^2, \qquad i = 1, n_c. \qquad (5.18)$$

A_i and B_i are the coefficients of time derivative of pressure $(\partial p/\partial t)$ and the pressure gradient $(\partial p/\partial x)$ respectively. Both A_i and B_i are functions of relative permeability, viscosity, pressure and PVT properties. During the production, the reservoir pressure varies both temporally and spatially, so does the compositional change, as indicated by Eq. 5.18. If the producer is controlled at a constant bottom hole flowing pressure $(\partial p/\partial t = 0)$, the rate of compositional change is determined by the pressure gradient only. For a low permeability system, the pressure gradient around the well is usually very large, and hence the compositional variation around the well can become significant as well. Away from the well, pressure gradient is generally small or sometimes, insignificant, the compositional variation is then mainly determined by the time derivative of pressure $(\partial p/\partial t)$.

Radial Flow

For three-dimensional radial flow in a cylindrical coordinate system, a similar derivation can be made by applying radial Darcy velocity. The general form is given as:

$$\frac{\partial z_i}{\partial t} = A_i \frac{\partial p}{\partial t} + B_i (\frac{\partial p}{\partial r})^2, \qquad i = 1, n_c. \tag{5.19}$$

Similar to the linear flow, the rate of compositional change in a radial flow $(\partial z_i/\partial t)$ also depends not only on pressure, but also on composition and both the gas and the condensate relative permeabilities. The detailed discussion of the compositional variation behavior is presented in the following section.

5.2 Compositional Variation Behavior

The condensate bank builds up around the producing well when the bottom hole flowing pressure drops below the dewpoint pressure. As the reservoir pressure declines, the bank grows and the well produces less heavy components at the surface. Eq. 5.18 and Eq. 5.19 provide us a straightforward theoretical model to facilitate the understanding of the process involved in the compositional change. Three binary-component

fluids consisting of methane and butane only are considered for compositional behavior analysis. The composition of the heavier component C_4 varies from 0.15 to 0.25, representing a range of lean, near-critical and light oil mixtures. Figure 5.1 shows the PT phase diagram for the methane-butane systems adopted in this analysis. The reservoir temperature is 60 ^oF and is assumed to remain constant during production. At reservoir temperature, the fluid with 15% butane is a lean gas-condensate system, the fluid with 20% butane is near critical gas-condensate, while the fluid with 25% Butane is light oil. For gas-condensate fluid, the maximum of the CVD liquid dropout, as shown in Figure 5.2, varies from 31% to 11% in terms of liquid volume relative to the dewpoint volume at temperature 60 ^oF, and in the light oil case, the fluid originally consists of 100% butane at the reservoir condition, and the liquid percentage drops as the solution gas evolves from the system as the reservoir pressure drops below bubble-point pressure.

As illustrated in Eq. 5.19 and Eq. 5.18, the variation rate of compositions depends on the time derivative of pressure ($\partial p/\partial t$), the pressure gradient ($\partial p/\partial x$) for linear flow or ($\partial p/\partial r$) for radial flow and their coefficients A_i and B_i. According to the definition of A_i (Eq. 5.16) and B_i(Eq. 5.17), both A_i and B_i consist of the mobility term m_i and m. Since mobility is closely related to relative permeability. A representative relative permeability model needs to be used in the A_i and B_i calculation. In the following section, we will examine the sensitivity of A_i and B_i to relative permeability, pressure and fluid types.

The A_i and B_i terms in Eq. 5.18 are calculated for the heavier component C_4 from the PVT properties and relative permeabilities. The PVT properties, such as molar density, composition, viscosity and interfacial tension etc, were modeled with WinProp (version 2006, Computer Modeling Group Ltd.) The Peng-Robinson equation of state (EoS) was used to represent the thermodynamic properties of the fluids and the viscosity calculation is based on the Pederson Corresponding States model. Three relative permeability models were used in this calculation. Details of the relative permeability modeling are presented in the flowing subsection.
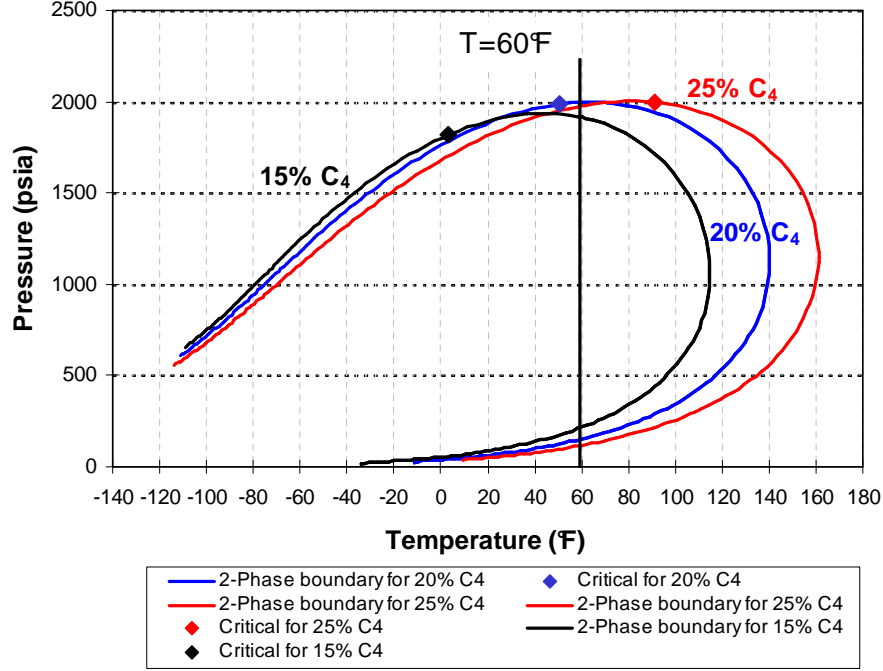
Figure 5.1: PT diagram of methane-butane systems. The reservoir temperature is 60 ^oF. At reservoir temperature, the fluid with 15% butane is a lean gas-condensate system, the fluid with 20% butane is near critical gas-condensate, while the fluid with 25% Butane is light oil.

5.2.1 The Impact of Relative Permeability Models

Both coefficients A_i and B_i are functions of mobility terms m_i and m. To model the mobility correctly, we need to have a representative relative permeability model. In the following section, we will demonstrate how the relative permeability plays a role in the A_i and B_i terms. In the governing equation, we did not include the capillary pressure terms explicitly. This treatment may not be appropriate when the gas-condensate fluid is far away from the critical point, the interfacial tension is high and the phase interface is distinct. To account for the influence of high interfacial tension (IFT) , we can adopt a relative permeability model with IFT dependent functions. The IFT dependant relative permeability model was initially proposed by Bette *et al.*
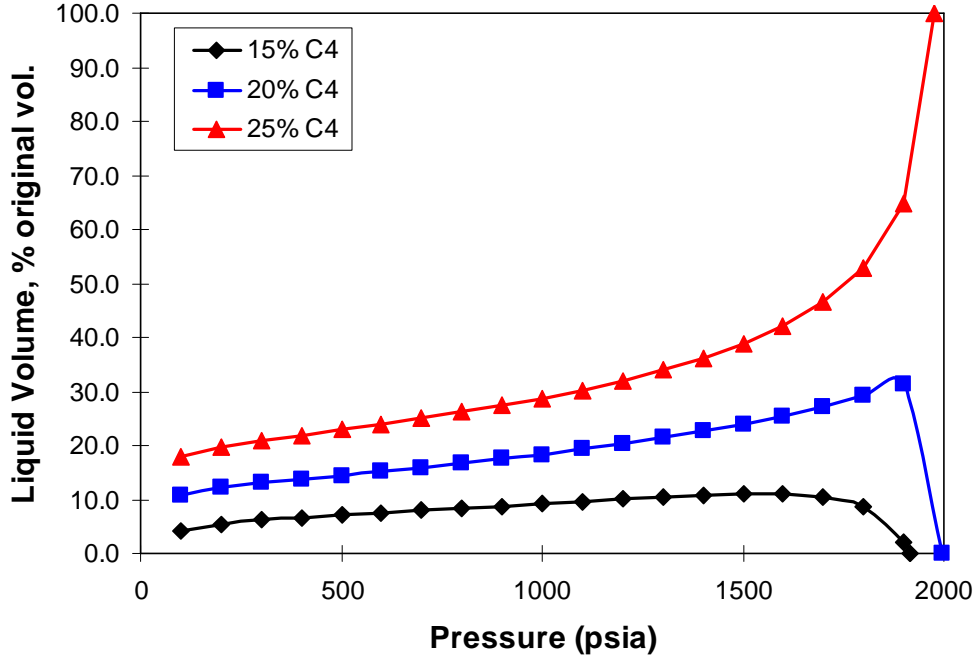
Figure 5.2: CVD liquid dropout curves for three fluids at temperature $60\,^oF$. At reservoir temperature, the fluid with 15% butane is an lean-intermediate gas-condensate system, having a maximum liquid drop of 10.9%; the fluid with 20% butane is near critical gas-condensate with a maximum liquid drop of 31.4%; the fluid with 25% Butane is light oil with 100% oil in reservoir condition.

(1991) and Coats (1980). Recently, Hartman and Cullick (1994) applied this method to study the oil recovery at low interfacial tension. The relative permeabilities to condensate, k_{rc} and to gas, k_{rg}, at a specified saturation is:

$$k_{rc} = f(\sigma)k_{rci} + (1 - f(\sigma))k_{rcm} \tag{5.20}$$

$$k_{rg} = f(\sigma)k_{rgi} + (1 - f(\sigma))k_{rgm} \tag{5.21}$$

$$f(\sigma) = (\frac{\sigma}{\sigma^*})^{\frac{1}{n}} \tag{5.22}$$

where σ is the IFT, σ^* is a reference IFT, k_{rcm} and k_{rgm} are the condensate and gas relative permeabilities at complete miscibility, the immiscible k_{rci} and k_{rgi} are the condensate and gas relative permeabilities for the fluids at IFT values equal to or greater than σ^*, and n is an adjustable exponent. Eq. 5.20 and Eq. 5.21 states that the relative permeability transition function is a mixing model as a function of IFT.

Based on experimental data, Hartman and Cullick (1994) suggested a correlation for residual condensate saturation to gas as a function of IFT:

$$S_{crg}(\sigma) = [1 + 0.67log(\frac{\sigma}{\sigma^*})]S_{crgi} \tag{5.23}$$

The gas endpoint is:

$$S_{gc}(\sigma) = \frac{\sigma}{\sigma^*}S_{gc} \tag{5.24}$$

The miscible relative permeability used in the mixing function is normalized with respect to the IFT dependent endpoints:

$$k_{rcm} = \frac{1 - S_{crg}(\sigma) - S_g}{1 - S_{crg}(\sigma)} \tag{5.25}$$

$$k_{rgm} = \frac{S_g}{1 - S_{gc}(\sigma)} \tag{5.26}$$

When the fluid condition is far away from the critical point, the phase interface is distinct. The permeabilities of the liquid and vapor phase can be approximated with Eq. 5.27 and Eq. 5.28:

$$k_{rci} = [\frac{1 - S_{crg}(\sigma) - S_g}{1 - S_{crg}(\sigma)}]^2 \tag{5.27}$$

$$k_{rgi} = [\frac{S_g}{1 - S_{gc}(\sigma)}]^2 \tag{5.28}$$

Figure 5.3 shows the calculated interfacial tension (IFT) correlated with pressure data for the three binary fluids used in this compositional analysis. A good relationship (Eq. 5.29) between IFT and pressure can be inferred from the correlation.
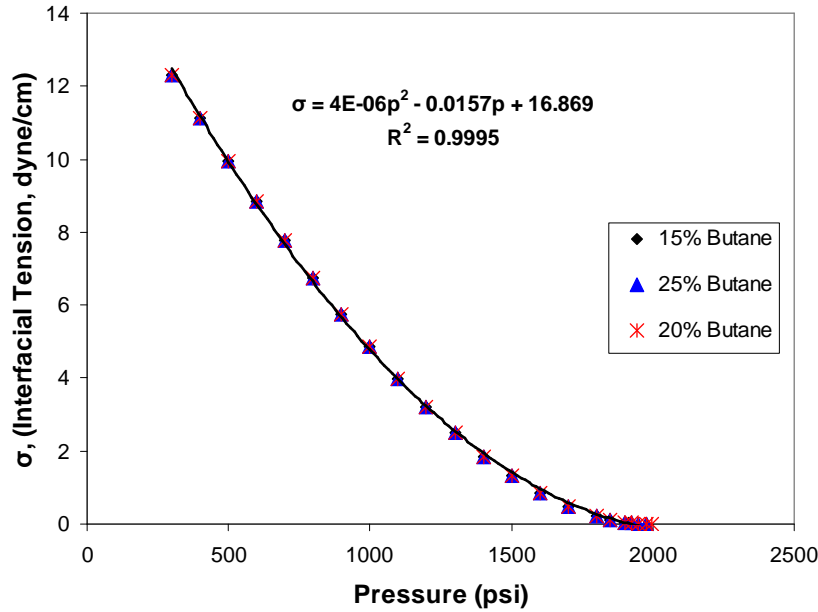
Figure 5.3: Interfacial tension (IFT) as a function of pressure. IFT is independent of fluid type and decreases with increasing pressure.

Notice that IFT is independent of fluid type, and it decreases sharply with increasing pressure, and IFT equals zero at dew-point pressure.

$$IFT = 4 \times 10^{-6}p^2 - 0.0157p + 16.869 \tag{5.29}$$

Figure 5.4 illustrates the difference among three different relative permeability models for a binary-component fluid with 25% butane. The miscible treatment of relative permeability is near X-curve shape and has the lowest critical condensate saturation threshold, which implies that in the miscible situation, liquid is easier to move than immiscible cases. As the miscibility decreases in the fluid, liquid phase in the mixture needs to overcome greater critical condensate saturation to become mobile. The liquid mobility is also harmed as the phase interface becomes distinct.

Although IFT itself only depends on pressure and independent of fluid types, the relative permeability is affected by the fluid type because different fluid has different liquid drop-out volume, and hence different liquid saturation. Figure 5.5 shows the
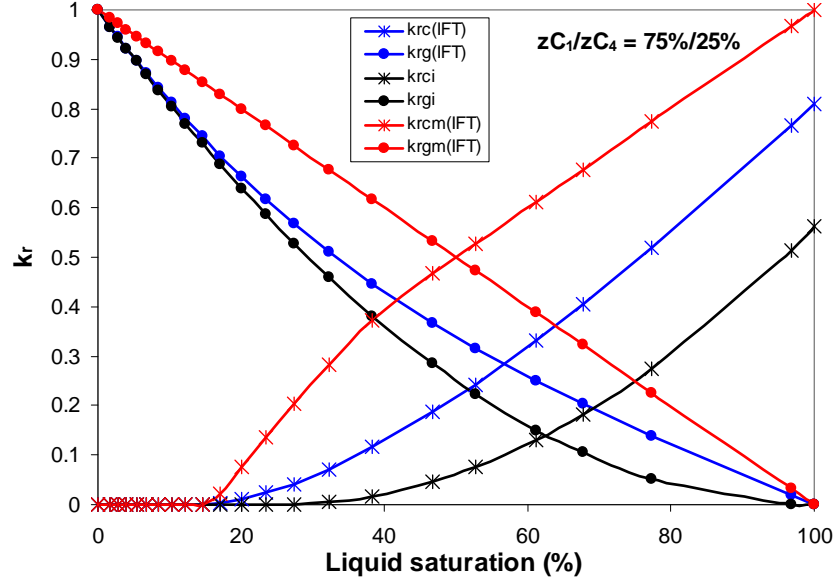
Figure 5.4: Different relative permeability curves for a binary methane and butane system with 25% butane. $krc(IFT)$ and $krg(IFT)$ are IFT corrected relative permeability; $krci$ and $krgi$ are relative permeability curves with immiscible treatment and $krcm$ and $krgm$ are miscible treatment of relative permeabilities.

IFT corrected relative permeabilities for three fluids. Notice that the leaner the fluid, the lower the threshold for the liquid phase to mobilize. Both the liquid and the gas exhibit greater capability to move in a leaner fluid than in a richer one. This is due to the fact that the leaner fluids tend to have greater miscibility.

Figure 5.6, Figure 5.7 and Figure 5.8 show the influences of the relative permeability on term $ln(m_i/m)$ for different fluids. $ln(m_i/m)$ bears a good quadratic relationship with pressure for all fluids with three different relative permeability models. In the lean gas-condensate case ($z_{C_4} = 0.15$), $ln(m_i/m)$ values resulting from different relative permeability curves show very little discrepancy, and the nuance appears on the low IFT, high pressure side. Different relative permeability models do have greater impact on $ln(m_i/m)$ term in the case of richer fluid, ($z_{C_4} = 0.25$) in this example. Greater difference in $z_{C_4} = 0.25$ also exists on the higher pressure side. The richer the fluid, the greater the impact of relative permeability. In all cases, the
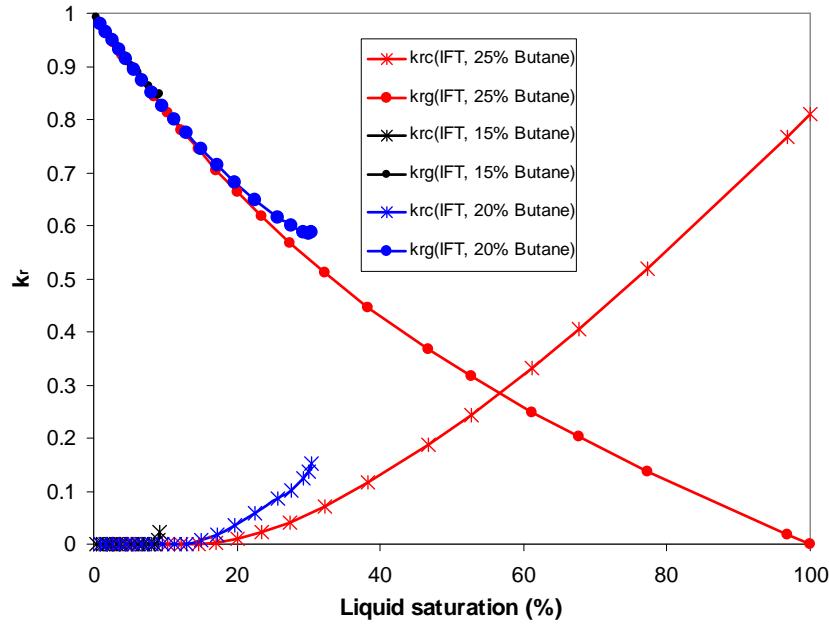
Figure 5.5: IFT corrected relative permeability curves for binary methane and butane systems with 15% butane, 20% butane and 25% butane.

miscible treatment of relative permeability always give the highest $ln(m_i/m)$ value, and the completely immiscible case has the lowest $ln(m_i/m)$ value.

Figure 5.9 shows the influences of relative permeability on coefficient A_{C_4}. First of all, A_{C_4} is very small of the order of 10^{-4} and there are very small differences in A_{C_4} value on the high pressure side. The difference is also small in rich fluids, as shown in Figure 5.10.

Compared with term A_i, term B_i is of the order of 10^{-2}, 100 times greater than term A_i (Figure 5.11 and Figure 5.12). The impact of relative permeability is obvious for both lean and rich fluids, especially on the high pressure side. Unlike A_i, which is negative when pressure is below the dew-point pressure, B_i is positive when the pressure is above some threshold, say 1000 psi, in both cases. The richer the fluid, the greater the discrepancy of B_i in the high pressure end for different relative permeability models.

In summary, relative permeability has greater impact on term B_i than on term A_i, and the difference varies with fluid types and pressure. The richer the fluid,
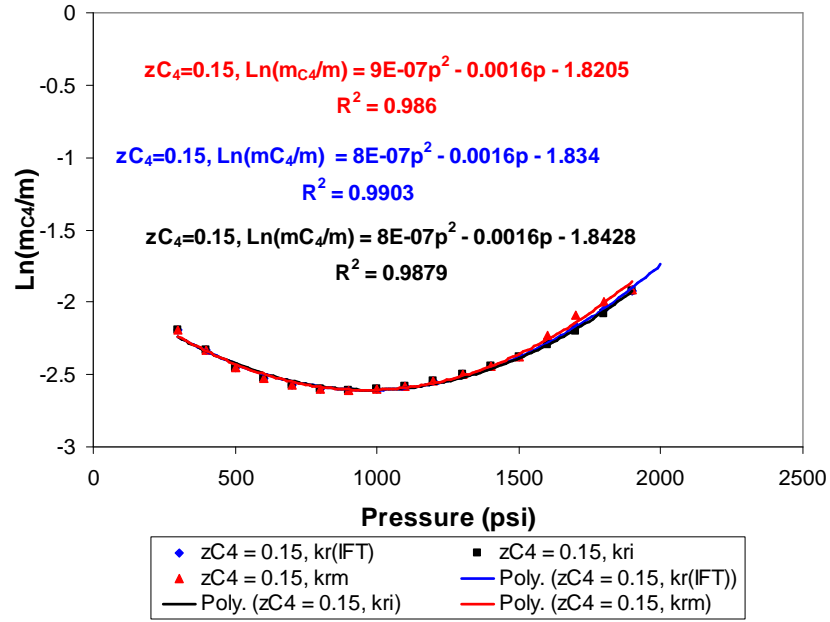
Figure 5.6: Variation of term $Ln(m_i/m)$ with pressure for a methane-butane system ($z_{C_4} = 0.15$) with different relative permeability models.
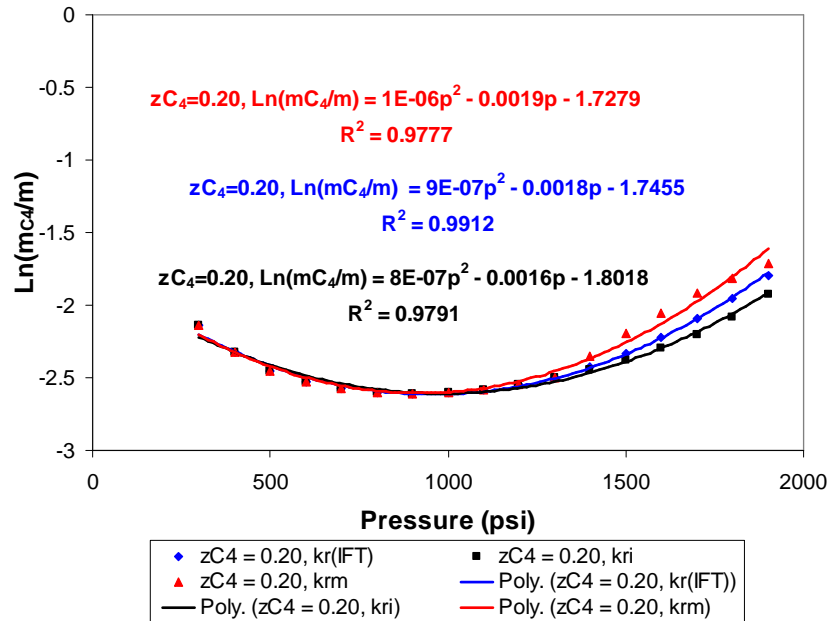
Figure 5.7: Variation of term $Ln(m_i/m)$ with pressure for a methane-butane system ($z_{C_4} = 0.20$) with different relative permeability models.
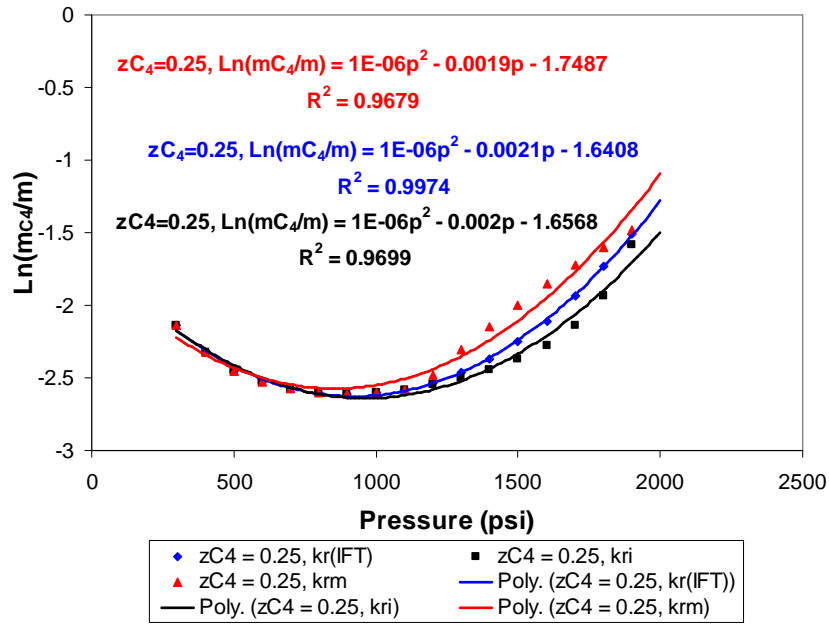
Figure 5.8: Variation of term $Ln(m_i/m)$ with pressure for a methane-butane system ($zC_4 = 0.25$) with different relative permeability models.
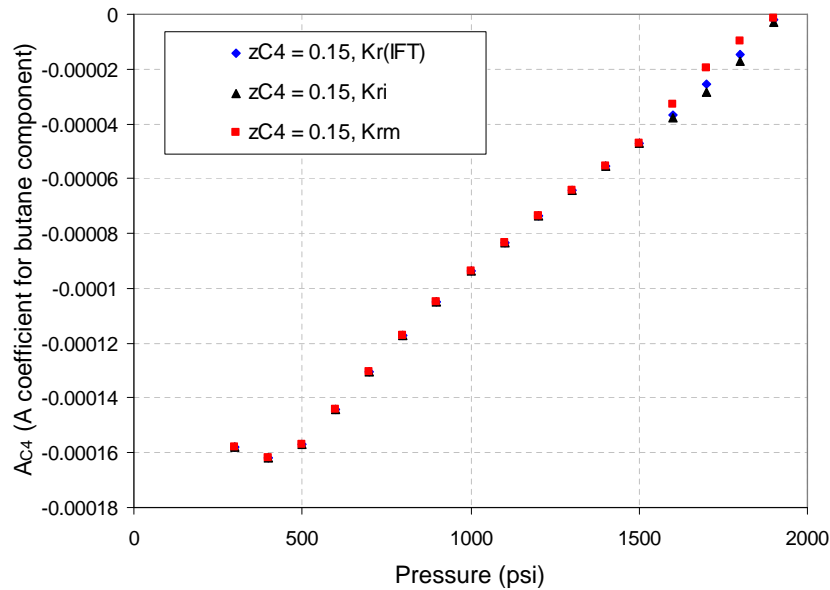
Figure 5.9: Variation of term A_{C_4} with pressure for a methane-butane system ($z_{C_4} = 0.15$) with different relative permeability models.
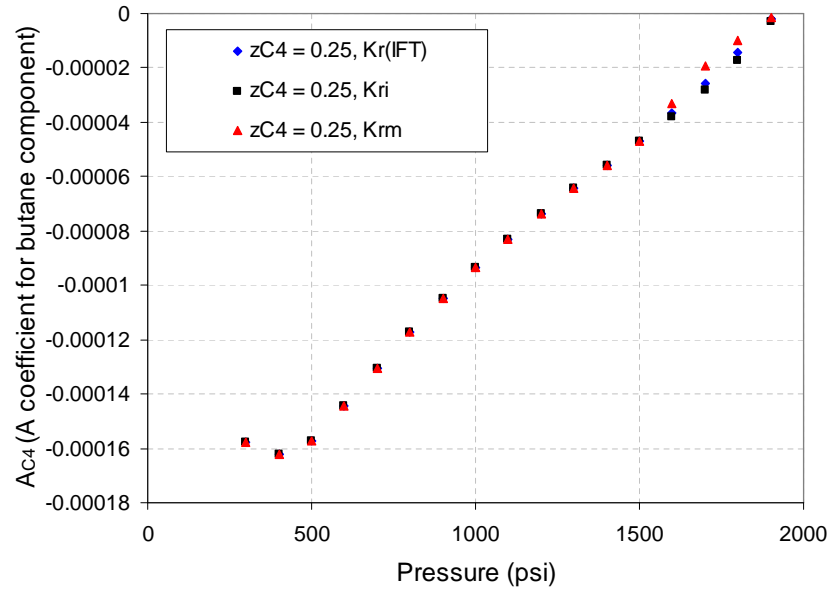
Figure 5.10: Variation of term A_{C_4} with pressure for a methane-butane system (z_{C_4} = 0.25) with different relative permeability models.
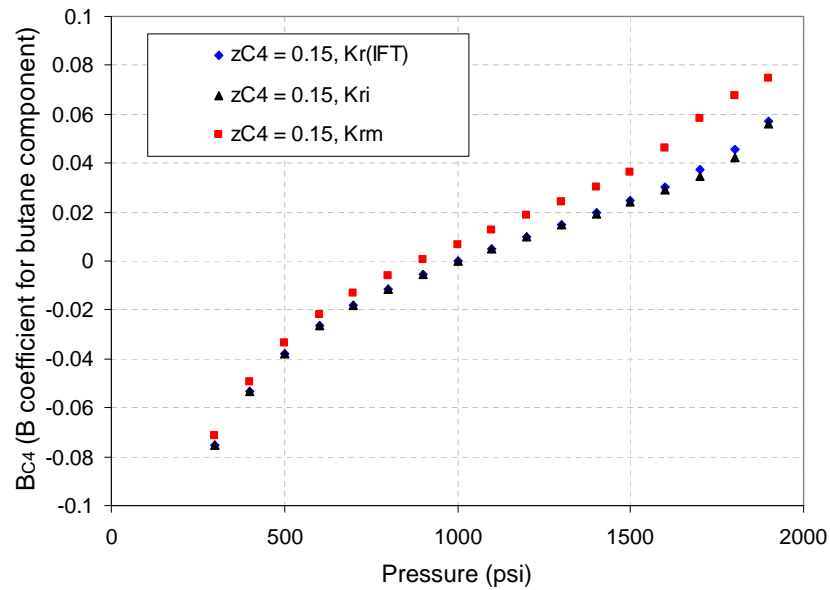
Figure 5.11: Variation of term B_{C_4} with pressure for a methane-butane system (zC_4 = 0.15) with different relative permeability models.
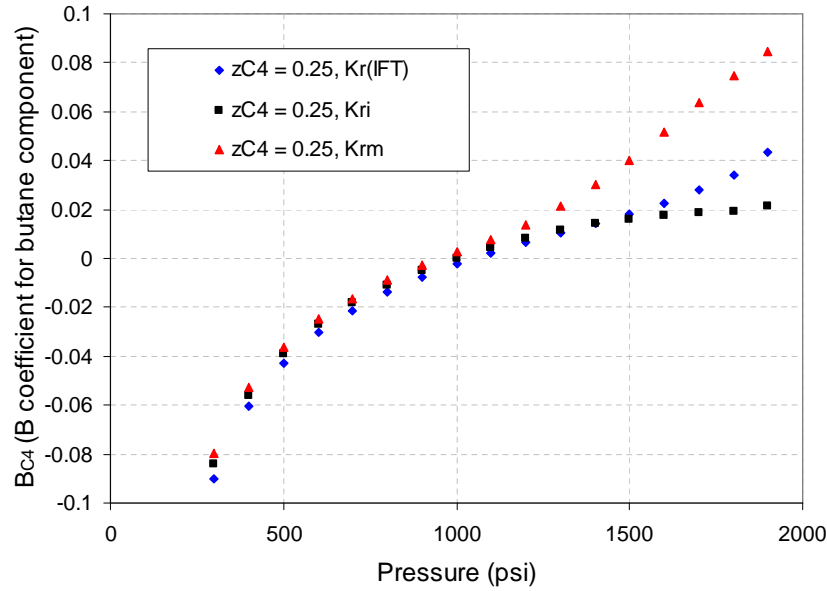
Figure 5.12: Variation of term B_{C_4} with pressure for a methane-butane system (zC_4 = 0.25) with different relative permeability models.

the greater the differences and the higher the pressure, the greater the differences. Miscible behavior tends to generate greater A_i and B_i values, while immiscible fluid has lower A_i and B_i values.

5.2.2   The Impact of Pressure

Figure 5.9, Figure 5.10, Figure 5.11 and Figure 5.12 discussed in the previous subsection show the great dependency of B_i on relative permeability models. These figures also show that both A_i and B_i are highly influenced by pressure. Both A_i and B_i decrease as the pressure drops. The magnitude of the decrease in A_i is almost doubled when the heavier component concentration varies from 0.15 to 0.20. B_i shows less magnitude change for different fluid types. A_i value is negative and relatively small, of the order of 10^{-4} within the pressure range presented in this study, while B_i is positive at higher pressure end, and negative on the lower side of pressure range and B_i is 100 times greater than A_i in magnitude. Since A_i is the coefficient for

the time derivative of pressure $(\partial p/\partial t)$ and B_i for the pressure gradient $(\partial p/\partial x)$ or $(\partial p/\partial r)$, the compositional change resulted from the time derivative of pressure is insignificant and hence negligible when $(\partial p/\partial t)$ is small. This is true when the well flows at a constant bottom hole pressure. In this case, the compositional variation in the well block is controlled mainly by the pressure gradient around the well. In regions far away from the well, the pressure gradient $(\partial p/\partial x)$ or $(\partial p/\partial r)$ is relatively small and $(\partial p/\partial t)$ becomes relatively larger. In this case, the compositional change is dominated by $(\partial p/\partial t)$. Recall that A_i is by definition a small coefficient, and hence the compositional variation is considerably smaller in regions not near the well.

5.2.3   The Impact of Fluid Types

Since fluid properties are directly associated with fluid type, the difference in the fluid properties resulting from different fluid types is then carried over to terms Gi, G, A_i and B_i accordingly. Figure 5.13 shows that different fluids have minor impact on the overall molar density term G, hence, $ln(G)$. Rich fluid results in greater $ln(G)$. The impact of fluid type on term A_{C_4}, however, is obvious and the influence is seen in the entire pressure range (Figure 5.14). At pressure 300 psi, A_{C_4} is ranging from -0.00016 to -0.00056 as the heavier component butane mole concentration varies from 0.15 to 0.25. The difference on A_{C_4} decreases as the fluid pressure increases. As the fluid pressure approaches dew-point pressure, A_{C_4} approaches zero. This implies that when the pressure is around dew-point pressure, the term $A_{C_4}(\partial p/\partial t)$ draws close to negligible. The impact of fluid type on term B_{C_4} is very small, and rich fluid gives slightly smaller B_{C_4} value according to Figure 5.11.

In summary, fluid type, relative permeability and pressure all have impact on terms A_i and B_i, hence $\partial z_i/\partial t$. A_i is mainly impacted by pressure and fluid type. Higher pressure gives greater A_i value for the heavier component C_4 for the binary methane and butane system and richer fluid yields lower A_{C_4} value. The impact of relative permeability on A_i is negligible and only noticeable as pressure close to dew-point pressure. Relative permeability and pressure have greater impact on B_i than fluid type. The influence of fluid types on B_i is small and only detectable as the fluid
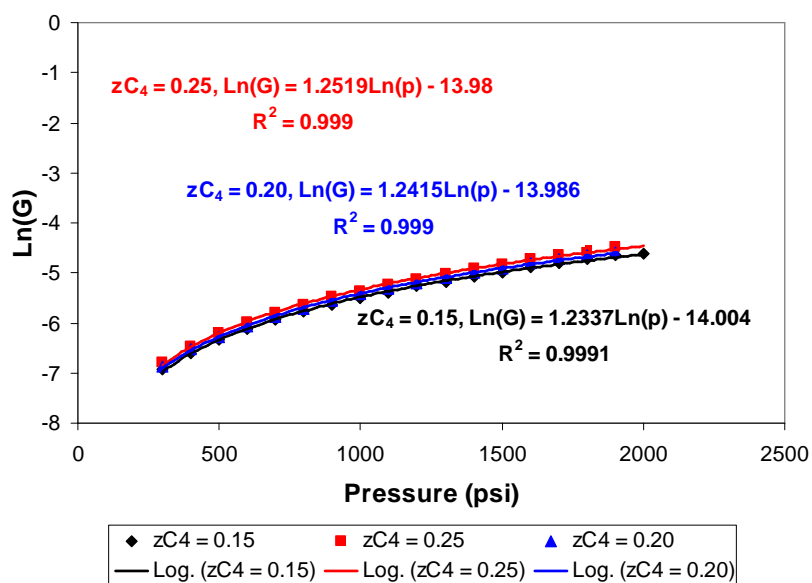
Figure 5.13: Variation of term G with pressure for a methane-butane systems with different compositions.
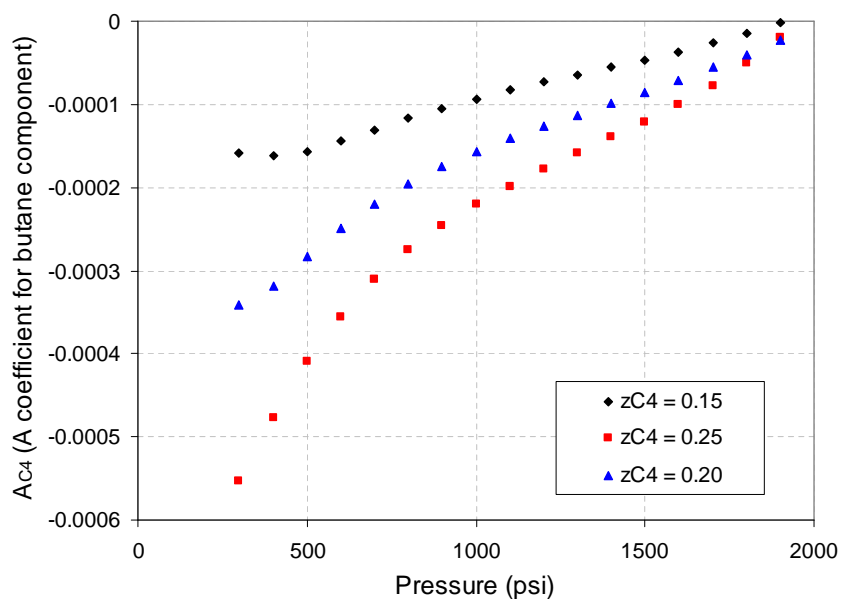
Figure 5.14: Variation of term A_{C_4} with pressure for methane-butane systems with different compositions.
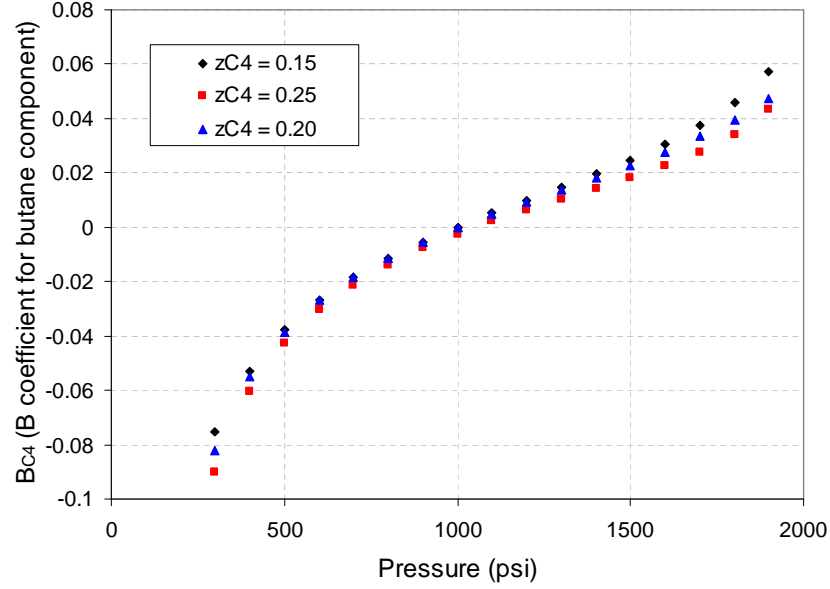
Figure 5.15: Variation of term B_{C_4} with pressure for methane-butane systems with different compositions.

pressure approaches dew-point pressure. In general, miscible behavior yields greater value in B_i, and B_i decreases as the miscibility reduces on the phase interface. B_{C_4} is negative under lower flow pressure and positive at higher pressure. At some point, B_{C_4} can be zero.

The magnitude of A_i is insignificant in general and therefore negligible when $(\partial p / \partial t)$ is very small. A_{C_4} is negative for the methane and butane binary system, which implies that in the depletion scenario, $(\partial p / \partial t)$ is negative, $A_{C_4}(\partial p / \partial t)$ is therefore positive. The compositional variation of C_4 resulting from the $A_{C_4}(\partial p / \partial t)$ part is then positive. In another words, the methane and butane mixture becomes richer during depletion if $(\partial p / \partial t)$ is the dominant factor. This is often true when the flow region is far away from the well. In zones other than the near-well region, the pressure gradient $(\partial p / \partial x)$ or $(\partial p / \partial r)$ is insignificant and can be negligible.

When the gas-condensate well flows at a constant bottom hole pressure $(\partial p / \partial t = 0)$ or the flow pressure approaches dew-point pressure (A_i approaches zero), $A_{C_4}(\partial p / \partial t)$ is zero or close to zero, the pressure gradient part is the main factor controlling the

compositional variation. In either of these two cases, the compositional variation rate of butane can be either positive or negative depending on the sign of B_i. When the pressure is high, $B_i > 0$, the overall butane concentration increases with time. At lower pressure, $B_i < 0$, the overall butane concentration decreases with time. As pressure decreases, some part of the accumulated liquid starts to vaporize, this may account for the decrease in overall butane concentration. The dividing point is, however, much lower than the pressure corresponding to the maximum liquid drop-out pressure. This is due to the relative permeability effect. The condensate drop-out during pressure draw down accumulates and becomes mobile only when the accumulated condensate saturation exceeds the critical condensate saturation.

5.3   Simulation Model for Binary Gas-Condensate Systems

In this section, we present our work on the numerical simulation of gas-condensate system on field scales. We first present the simulation model and results for a binary gas-condensate system and then later apply the simulation model to a multicomponent gas-condensate system and discuss the issues associated with different producing schemes. Finally we summarize important findings and discuss direction for future work.

5.3.1   Model Setup

The primary objective of the simulation is to understand the impact of producing scheme on the condensate banking and compositional variations. A hypothetical cylindrical reservoir model, with radius of 9699 ft and permeability-thickness of 162.5 $md - ft$ has been chosen. In the simulations, small grid block radii around the wellbore were chosen to allow accurate pressure drop calculation in the near well-bore region. A simulator $E300$ (2005a, $Eclipse$) with the fully implicit ($FULLIMP$) method

was used to simulate the performance under different producing strategies. The reservoir fluid is a binary synthetic gas-condensate system with $C_1/C_4 = 85\%/15\%$, characterized by Figure 2.2. The simulation is performed under reservoir temperature 60 ^oF.

The single producer in this simulation is controlled by gas rate and minimum bottom hole pressure. The well initially produces at the designated gas rate and switches to BHP control if the BHP is below the BHP minimum limit. The same gas rate but different BHP control schemes were adopted to explore the flow behavior features for this binary system.

5.3.2   Simulation Results for Binary Gas-Condensate Systems

Figure 5.16 shows the total gas production, well BHP and well gas production rate history for six different BHP configurations. The producer starts with constant production rate at 3300 MCF/day, and then switches to BHP pressure control as long as the flowing BHP drops below the BHP limit. BHP01, BHP02 and BHP03 scenarios follow this producing scheme switch. Under the other three scenarios, the well produces with constant producing rate as the flowing BHPs remain high above the BHP limit. As the BHP decreases from 700 psi in BHP01 to 200 psi in BHP06, the well shows delay in the production rate drop, hence achieved higher cummulative gas production, as shown in Figure 5.16(a). In BHP01, BHP02 and BHP03 scenarios, the well flows at a constant BHP ($\partial p/\partial t = 0$) during part of the production period.

According to Figure 5.11, as the well block pressure falls below 1000 psi, the overall mole concentration of the heavier component, butane (z_{C_4}), in the well block should decrease with time because of the negative B_i. However, the simulated (z_{C_4}), as shown in Figure 5.17(a) does not show decrease as predicted by the theoretical model (Eq. 5.19). This is caused by the accumulated condensate. The theoretical model does not account for the liquid accumulation as happened in the real porous medium. Although relative permeability is included in the theoretical model, the liquid saturation estimation is based on the in-situ pressure and original compositional

information. In real porous media, the condensate drops out and accumulates in the reservoir and only gains the mobility when the accumulated liquid saturation exceeds the threshold saturation. Since the liquid drop out is rich in heavier component, the local reservoir fluid becomes richer than the PVT cell flash calculation. Hence we do not see the expected heavier component drop in the well block at low well block pressure. Figure 5.17(b) illustrates the correlation of z_{C_4} in the flowing phase with pressure. The flowing fluid composition in this case reflects the condensate accumulation effect. When the flowing pressure drops immediately below the dewpoint pressure, the well produces leaner gas as the heavier component drops to the reservoir and stays immobile. As part of the condensate starts to flow and part of the butane previously stuck in the reservoir vaporizes, the well starts to produce more butane at the wellhead.

Different BHPs give rise to different compositional variations in the well block and wellhead fluid (Figure 5.18). As mentioned earlier, in scenarios $BHP01$, $BHP02$ and $BHP03$, the well flows at a constant BHP ($\partial p / \partial t = 0$) during part of the production period. During that period, we see that z_{C_4} actually remains constant. As analyzed in the previous section, at constant BHP ($\partial p / \partial t = 0$), the increase or decrease of the butane mole fraction depends on the sign of B_{C_4} unless B_{C_4} is zero or pressure gradient ($\partial p / \partial r = 0$). $\partial p / \partial r = 0$ implies that the well production rate is zero, which is not true in this case, and according to Figure 5.15, $B_{C_4} = 0$ at pressure around 1100 psi for $z_{c_4} = 0.25$. B_{C_4} reaches zero at higher pressure for fluid richer than $z_{c_4} = 0.25$. The bottom hole pressure in scenario $BHP01$, $BHP02$ and $BHP03$ are all below 1000 psi. Possible reason for the constant z_{C_4} under constant bottom hole pressure is that at the constant flowing pressure, the temporary butane concentration z_{C_4} is decreasing because of the negative B_{C_4}, however, because of the accumulation of butane in the earlier stage, the temporary decrease in the butane concentration cancels out the previous accumulation.

The producing fluid composition shows the predicted trend. The wellhead fluid becomes leaner initially as the liquid dropout is stuck in the reservoir, and becomes richer as the part of the condensate starts to flow. When the well is controlled by the BHP only, as in part of the scenarios $BHP01$, $BHP02$ and $BHP03$, the higher

the BHP pressure control, the lower the overall heavier component fraction in the reservoir and hence more heavier component produced at surface.

In summary, for this binary gas-condensate system, producing with the lower BHP constraint can yield higher cumulative gas production while losing more heavy component, butane, to reservoir liquid dropout.

5.4 Simulation Model for MultiComponent Gas-Condensate Systems

5.4.1 Model Setup

The multicomponent fluid properties are shown in Table 5.1. The phase envelope for the multicomponent gas-condensate system of component set 1 is shown in Figure 2.10, and the liquid dropout estimation is shown in Figure 2.11. IFT adjusted relative permeability were used in this simulation. Different from the binary cases studies in the previous section, different gas rate controls but the same minimum $BHP = 500$ psi constraint were explored in this simulation. The well produces at constant rate unless the flowing BHP falls below 500 psi, in this case, the well is then switched to the minimum BHP constraint. The PVT properties for this fluid were estimated with $PVTi$ (2005a, Schlumberger). The corrected Peng-Robinson equation of state (PRCORR) is used to represent the thermodynamic properties of the fluids and the viscosity calculation is based on the Pederson Corresponding States model.

5.4.2 Simulation Results for MultiComponent Gas-Condensate Systems

Figure 5.19, Figure 5.20 and Figure 5.21 show the simulation results for this multi-component system. Since the heavier components C_7^{+1}, C_7^{+2} and C_7^{+3} have very small mole fractions, three components are grouped together and form a new group C_7^+ for discussion. As we can see from these figures that the different rate controls give rise to different flowing bottom hole pressure, which yields similar results as setting different

(a) Accumulated gas production with time.

(b) Bottom hole pressure history.

(c) Gas production history

Figure 5.16: History profiles of (a) The accumulated gas production ($WGPT$ (b) Well bottom hole pressure ($WBHP$) and (c) Gas production rate ($WGPR$) for a binary gas-condensate system.
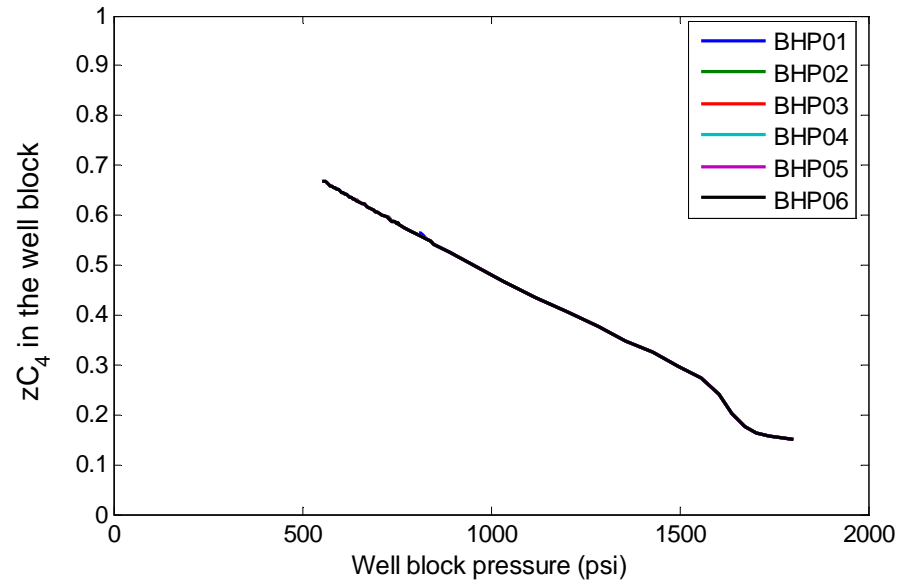
(a) Overall C$_4$ mole fraction in the well block vs. well block pressure.
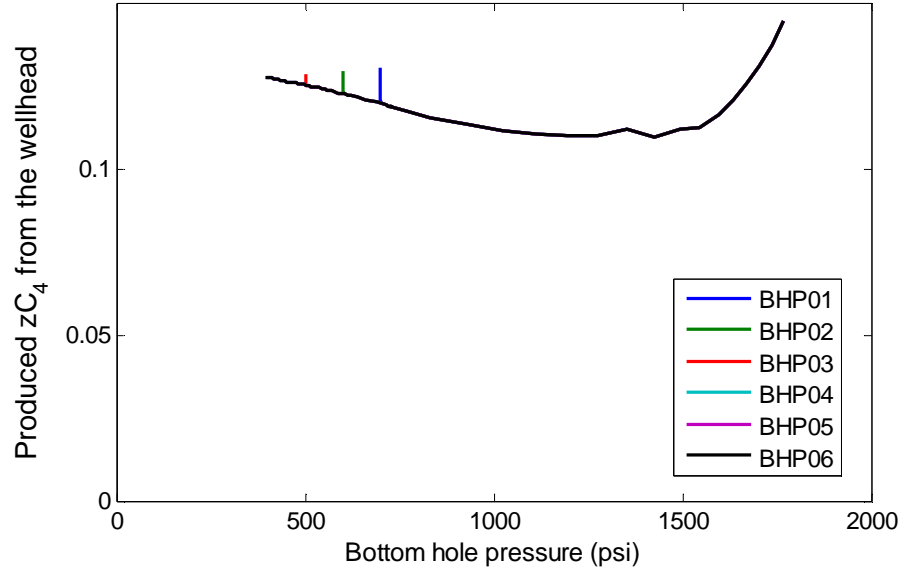
(b) Flowing C$_4$ mole fraction vs. well bottom hole pressure (BHP).

Figure 5.17: Overall butane mole fraction z_{C_4} profiles. (a) Overall butane mole fraction Bz_{C_4} profiles in the well block *vs.* the well block pressure. (a) Overall butane mole fraction Wz_{C_4} profiles in the producing fluid *vs. BHP*.

(a) Overall C_4 mole fraction in the well block vs. time.

(b) Flowing C_4 mole fraction vs. time.

Figure 5.18: Overall butane mole fraction z_{C_4} history profiles. (a) History of the overall butane mole fraction Bz_{C_4} in the well block. (a) History of the overall butane mole fraction Wz_{C_4} profiles in the producing fluid.

Table 5.1: Fluid characterization for a multicomponent gas-condensate system.

Component	Composition	$P_C(atm)$	$T_C(K)$	Acentric factor	Mol. Weight
N_2	0.0121	72.8	304.2	0.225	44.01
CO_2	0.0194	33.5	126.2	0.04	28.013
C_1	0.6599	45.4	190.6	0.008	16.043
C_2	0.0869	48.2	305.4	0.098	30.07
C_3	0.0591	41.9	369.8	0.152	44.097
C_{4-6}	0.0967	35.0386	448.0781	0.225	66.85942
C_7^{+1}	0.04745	27.94985	465.6182	0.3123	107.77943
C_7^{+2}	0.01515	16.84569	587.7992	0.5567	198.56203
C_7^{+3}	0.0033	10.91565	717.7171	0.91692	335.1979

BHP limits in the binary cases. The maximum rate control, scheme $BHP06$, yields maximum total gas production. The overall composition $z_{C_7^+}$ in the well block varies as the well is controlled under different $BHPs$. The higher the gas rate, hence the lower the flowing BHP, and the more heavier components are seen in the reservoir fluid, as illustrated in Figure 5.20(a). The well-head fluid composition bears a similar relation with pressure and time as in the binary case. The C_7^+ mole fraction in both the well block and the well-head fluid changes. As C_7^+ deposits in the reservoir, the well loses some heavier component production initially as BHP drops below the dewpoint pressure. The reduced production of the heavier component is remedied as the BHP further draws down because part of the condensate build-up resumes flow or part of the condensate starts to vaporize at lower flowing pressure. Condensate vaporizing in the low pressure condition is not always feasible because of the phase envelopes, as shown in Figure 2.10. Notice that as the reservoir pressure drops below dew-point, the original reservoir fluid shifts toward heavier gas-condensate, and even to light oil side. As a result of this phase envelope shifting, the vaporization becomes less feasible.

Different from the binary simulations, both well BHP and production rate have

great ranges in the multicomponent simulations. As a result, we saw more differences in the $z_{C_7^+}$ in the well block and also the well-head flow. The general findings in the binary simulation still apply here. The lower the BHP, the more $z_{C_7^+}$ accumulates in the well block and the less $z_{C_7^+}$ produced from the well-head flow, as seen in Figure 5.20.

Combined with the observations from the binary system, we found that for both the binary simple gas-condensate system and the complex multicomponent system, no matter how rich or lean the fluid is, the higher the gas flow rate control, hence the lower the BHP constraint, the greater the total gas production yield, at the same time, the greater the loss of heavier component produced at the surface.

5.5   Flow Optimization with Genetic Algorithm

In both binary and multicomponent simulations, we choose six BHP or rate control scenarios to investigate the impact of different producing schemes on compositional variations. In this section, we used Genetic Algorithm (GA) technique to confirm and generalize the optimal producing strategy for gas production and condensate recovery.

Genetic Algorithm (GA) is a robust search method based on analogies to biology and genetics. Survival of the latest among a population of individuals, selection criteria, and reproduction strategies are concepts copied from the natural life and used as operators in this artificial environment (Holland, 1975). Only function evaluations are used rather than derivatives or other secondary descriptors in GA, which makes GA particularly handy for production optimization application as the value of the objective function is known.

GA begins the search with a population of parameter realizations, rather than a single realization as many of the conventional optimization methods might. Each set of possible configurations of the decision variables is referred to as one realization or member of the population. In this way, the search domain is covered in a random distribution. The realizations are perturbed by probabilistic rules rather than deterministic ones. To assure that evaluation values will never decrease from one generation to the next and assure that crossover and mutation do not lead to
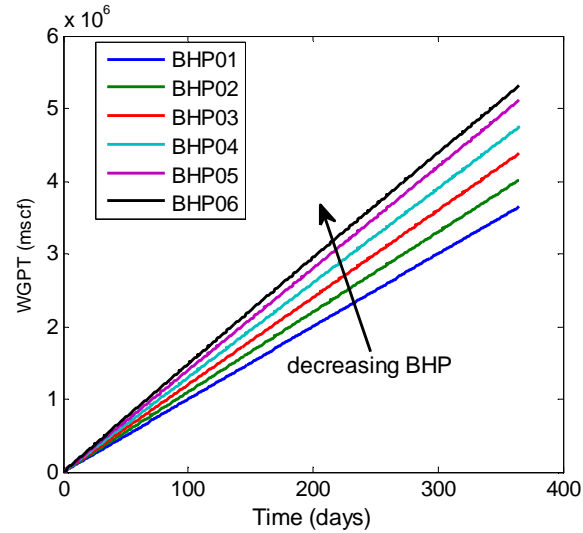
(a) Accumulated gas production with time.
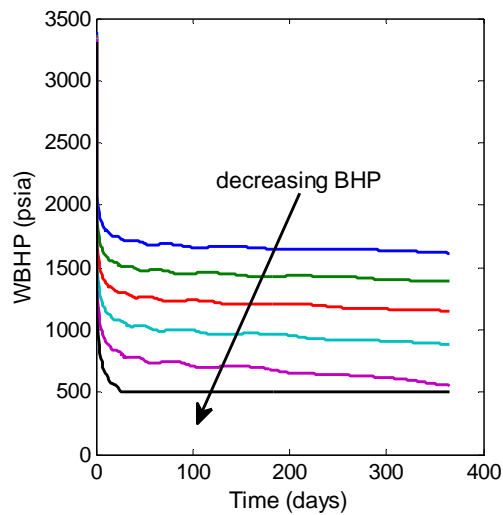
(b) Bottom hole pressure history.
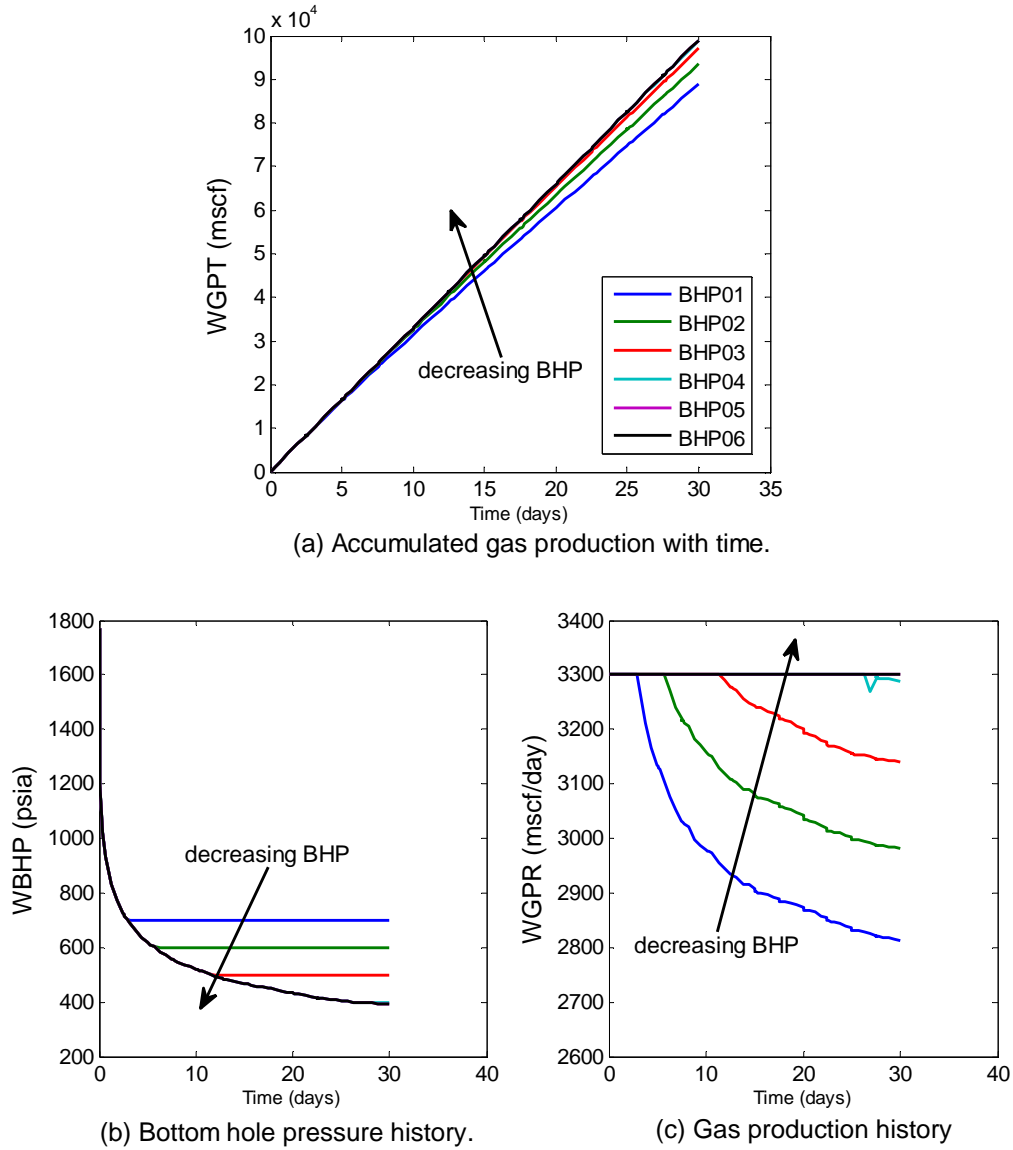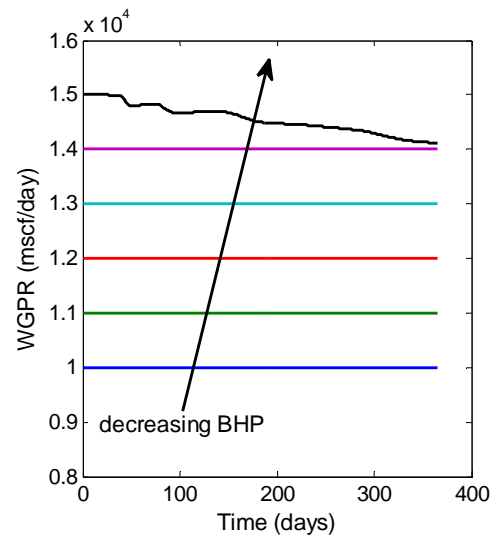

(c) Gas production history

Figure 5.19: History profiles of (a) The accumulated gas production ($WGPT$ (b) Well bottom hole pressure ($WBHP$) and (c) Gas production rate ($WGPR$ for a multicomponent gas-condensate system.
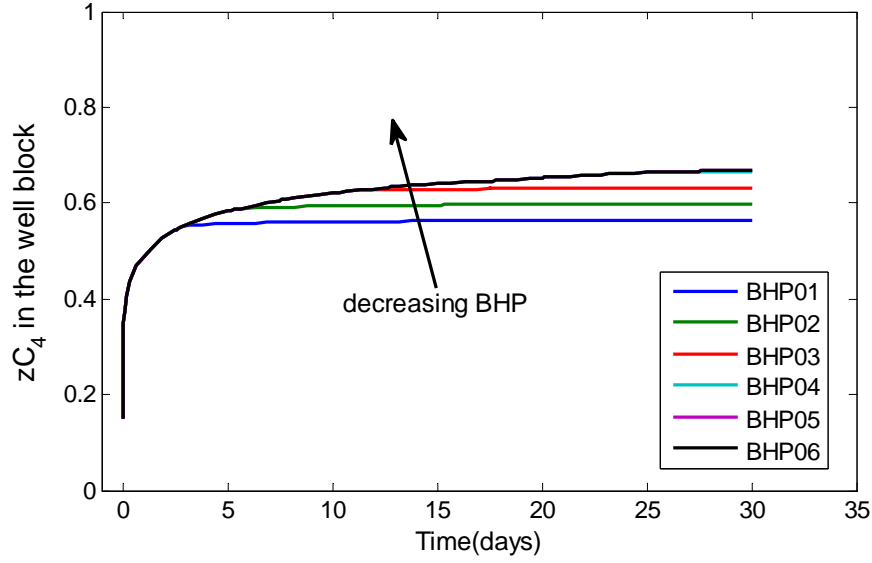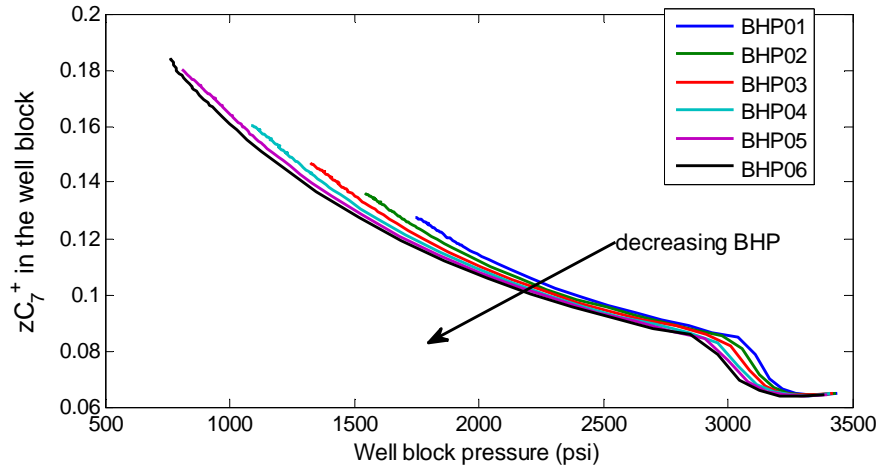
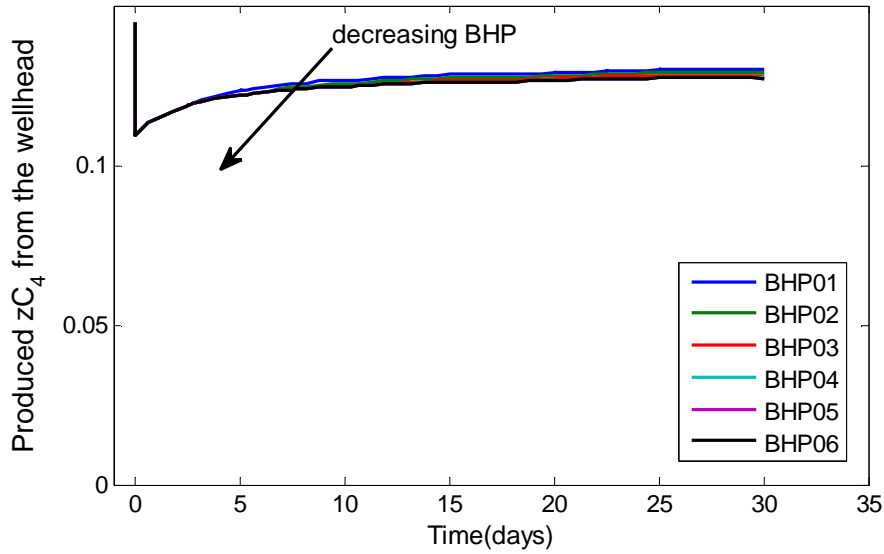(a) Overall C_7^+ mole fraction in the well block vs. well block pressure.

(b) Flowing C_7^+ mole fraction vs. well bottom hole pressure (BHP).

Figure 5.20: Overall butane mole fraction $z_{C_7^+}$ profiles. (a) Overall butane mole fraction $Bz_{C_7^+}$ profiles in the well block $vs.$ the well block pressure. (a) Overall butane mole fraction $Wz_{C_7^+}$ profiles in the producing fluid $vs.$ BHP.

(a) Overall C_7^+ mole fraction in the well block vs. time.

(b) Flowing C_7^+ mole fraction vs. time.

Figure 5.21: Overall butane mole fraction $z_{C_7^+}$ history profiles. (*a*) History of the overall butane mole fraction $Bz_{C_7^+}$ in the well block. (*a*) History of the overall butane mole fraction $Wz_{C_7^+}$ profiles in the producing fluid.
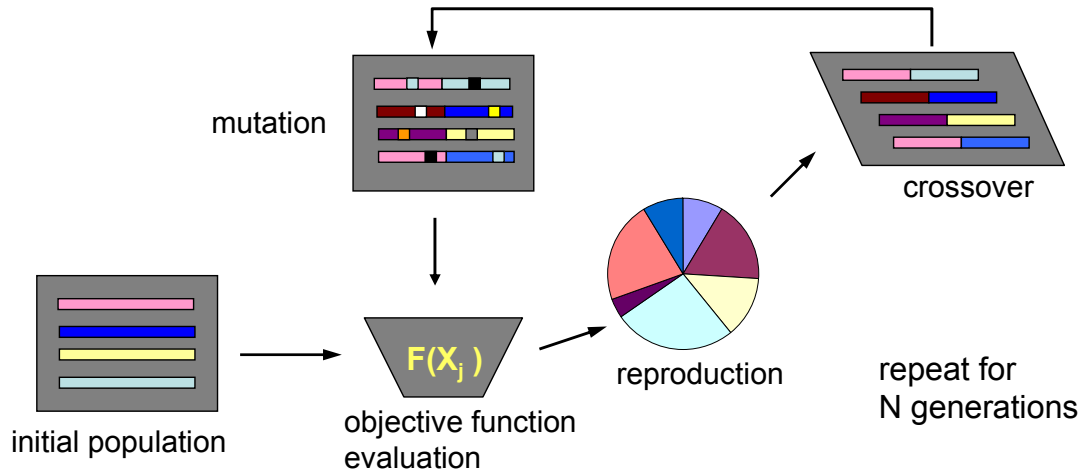
Figure 5.22: Computation procedure for Genetic Algorithm.

a degradation, we can use *elitism* in the GA model, in which the best individual is always saved from generation to generation. A typical Genetic Algorithm is processed as the procedure shown in Figure 5.22 and in the following pseudocode.

1. Choose initial population.

2. Evaluate the fitness of each individual in the population.

3. Repeat:

   - Select any two individuals to reproduce.
   - Breed new generation through crossover and mutation and give birth to offspring.
   - Evaluate the individual fitness of the offspring.
   - Replace worst ranked part of population with offspring.

4. Until termination.

Instead of fixing the BHP or production rate at a predefined value, combinations of random rates were used in the Genetic Algorithm in an attempt to define an optimal strategy. In this study, two producing parameters, BHP and $WGPR$, were

optimized. In BHP optimization, a BHP is defined as a combination of 30 random $BHPs$ from 500 to 2000 psi. and in $WGPR$ optimzation, a $WGPR$ is defined as a combination of 30 random production rates from 1,000 to 300,000 SCF/day. The individual population fitness is evaluated by the cumulative gas production ($WGPT$). A total of 100 generations were performed during the optimization process. For each generation, the mole fraction of the heavier component (z_{C_4}) in the well block is also checked as a secondary evaluation parameter. When two individuals produce the same amount of gas, the one with lower (z_{C_4}) in the well block is kept as one of the offsprings.

The final top three optimized $BHPs$ are shown in Figure 5.23, Figure 5.24 and Figure 5.28. The reference model has $BHP = 500psi$, the lowest boundary of the initial population. As observed from the binary simulations in the previous section, the lowest BHP scheme tends to yield the highest gas production, so the lowest $BHP = 500\ psi$ scenario is selected as a checkpoint for GA optimization results. In all GA simulations, a longer producing time, 3650 days, was chosen to investigate the long term compositional variation behavior. Figure 5.23 illustrates that all top three individuals have BHP close to the 500 psi, which is the lowest bottom hole pressure boundary. The optimized BHP after 100 generations comes as expected from previous observation. That is, the lowest BHP case yields the highest cumulative gas production. The z_{C_4} mole fraction in the well block reaches a startling high level of 0.7 as compared with initial 0.15. Produced z_{C_4} shows a sharp decrease initially as the condensate starts to deposit in the reservoir, and the well-head flow gains part of z_{C_4} back as the accumulated condensate begins to flow, however, in the long run, less and less butane is produced from the well, as shown in Figure 5.28(b).

Similar to BHP optimization, the optimized $WGPR$ also comes close to the highest reference $WGPR$ (Figure 5.23). From Figure 5.24 and Figure 5.25, we can see that although we gain total gas production by optimizing the producing rate, we also leave more butane in the reservoir.

To summarize the GA simulation results, we can conclude using low BHP or high production rate, we can achieve higher total gas production, but leaving with more butane, the heavier component in the reservoir. To minimize the condensate banking

(a) Accumulated gas production with time.
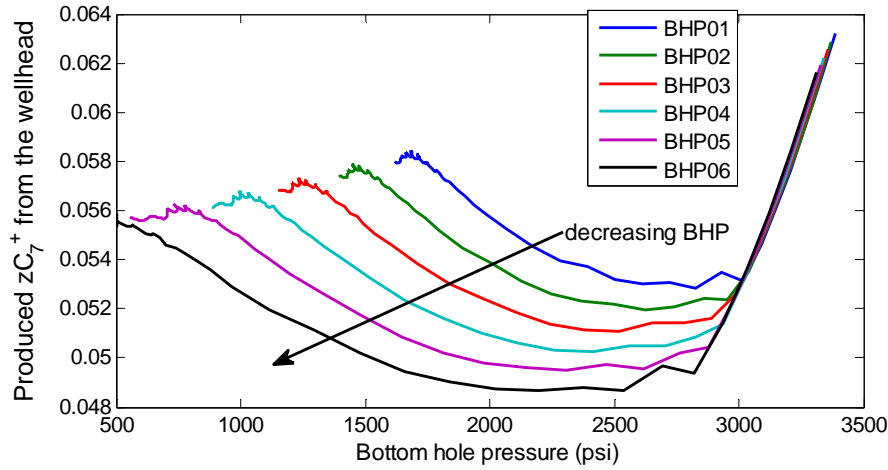

(b) Bottom hole pressure history.

(c) Gas production history.
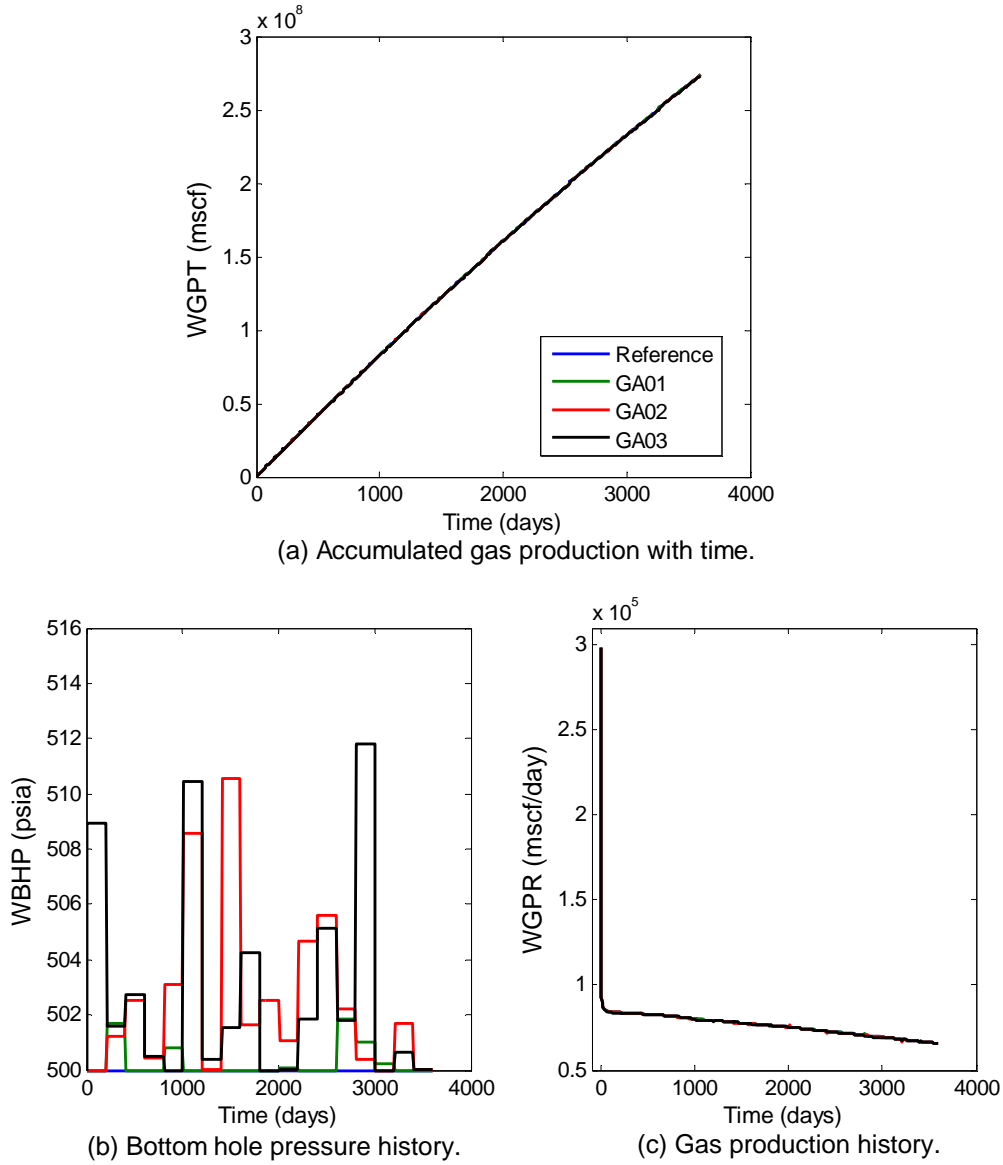
Figure 5.23: History profiles of (a) The accumulated gas production ($WGPT$ (b) Well bottom hole pressure ($WBHP$) and (c) Gas production rate ($WGPR$ for the top three $WBHP$ GA optimized scenarios.
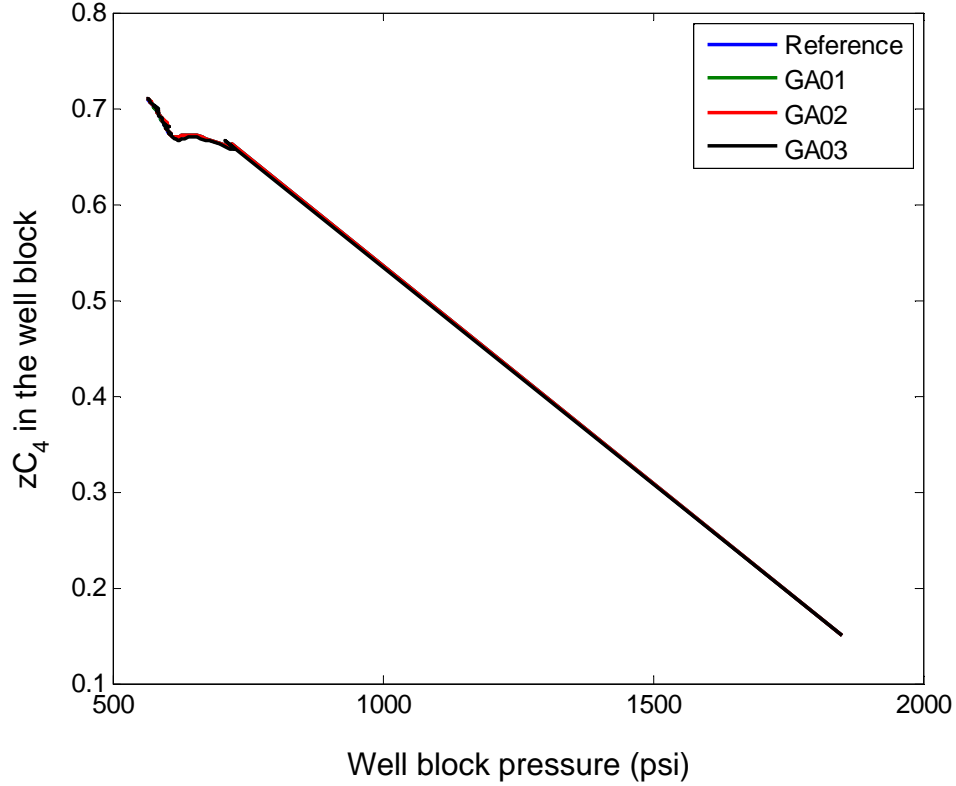
Figure 5.24: Overall butane mole fraction z_{C_4} profiles. (*a*) Overall butane mole fraction Bz_{C_4} profiles in the well block *vs.* the well block pressure. (*a*) Overall butane mole fraction Wz_{C_4} profiles in the producing fluid *vs.* BHP for the top three $WBHP$ GA optimized scenarios.

blockage and hence to enhance the ultimate liquid recovery, higher BHP or lower initial production rate may be a better strategy.

5.6 Summary

In the first section, a general form of material balance equation for condensate flow in porous media was developed for both one-dimensional linear flow and three-dimensional radial flow of two-phase gas-condensate fluid through porous media, with the effect of interfacial tension. The compositional variation of the reservoir fluid,
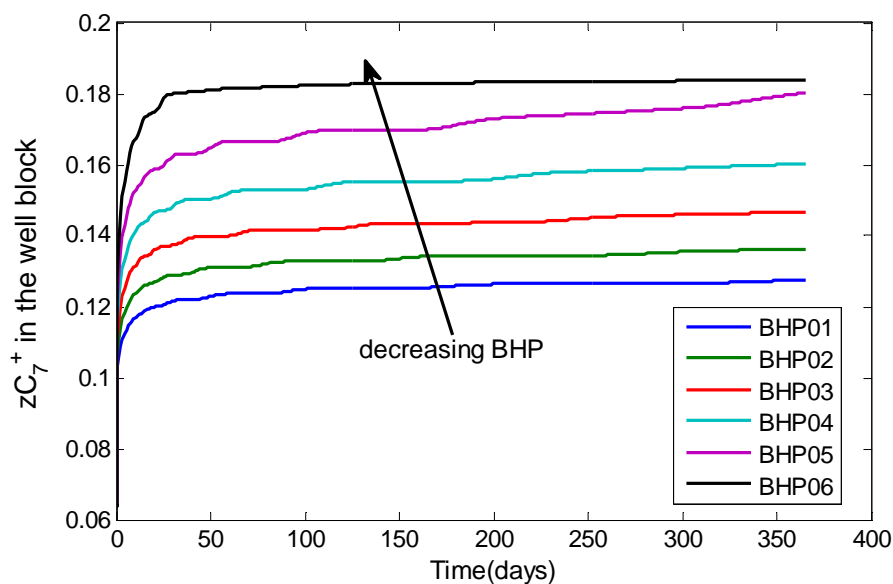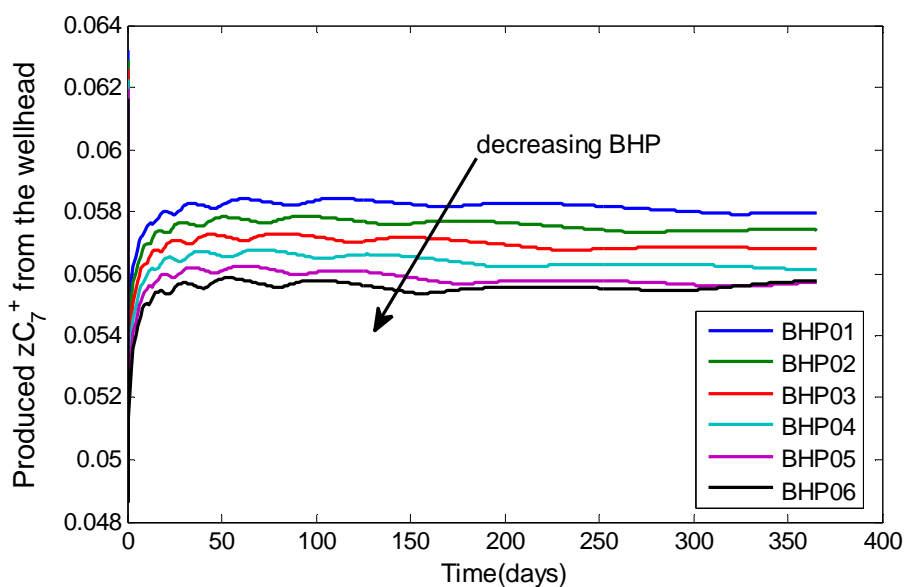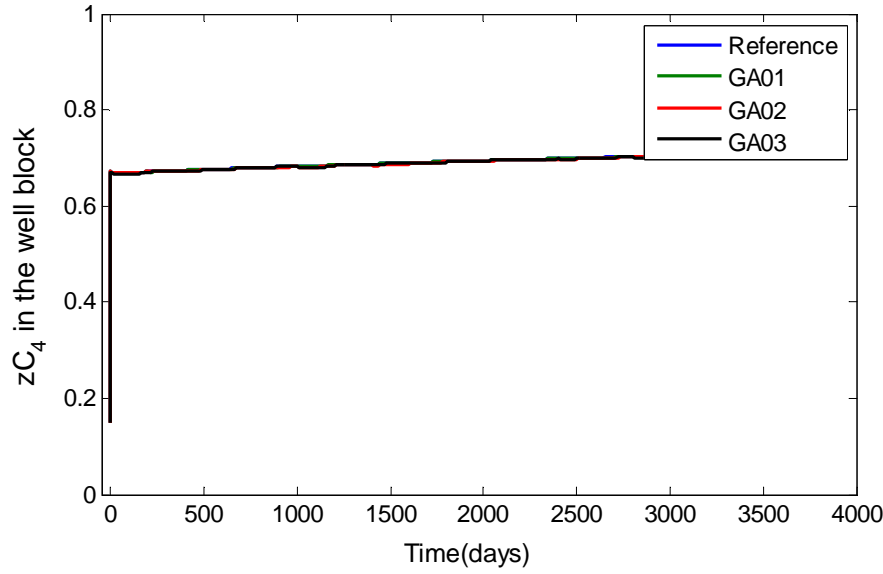
(a) Overall C$_4$ mole fraction in the well block vs. time.
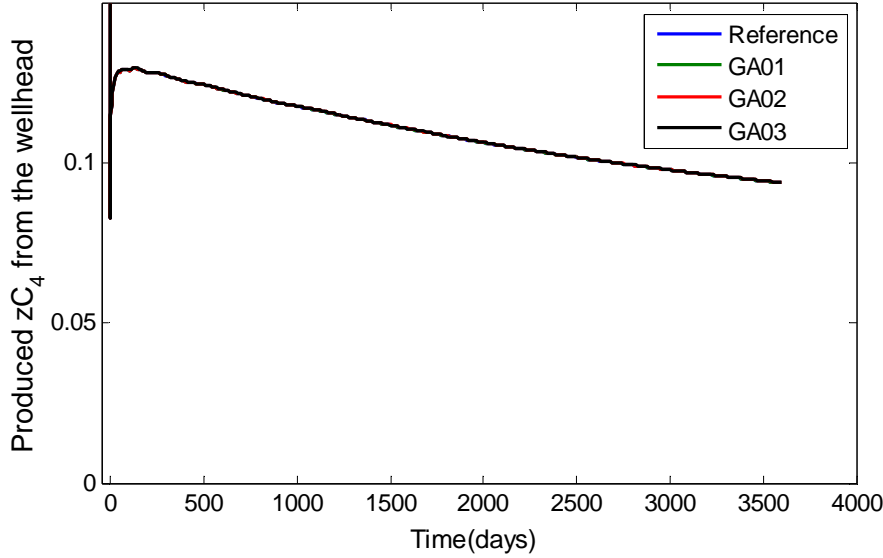
(b) Flowing C$_4$ mole fraction vs. time.

Figure 5.25: Overall butane mole fraction z_{C_4} history profiles. (a) History of the overall butane mole fraction Bz_{C_4} in the well block. (a) History of the overall butane mole fraction Wz_{C_4} profiles in the producing fluid for the top three $WBHP$ GA optimized scenarios.
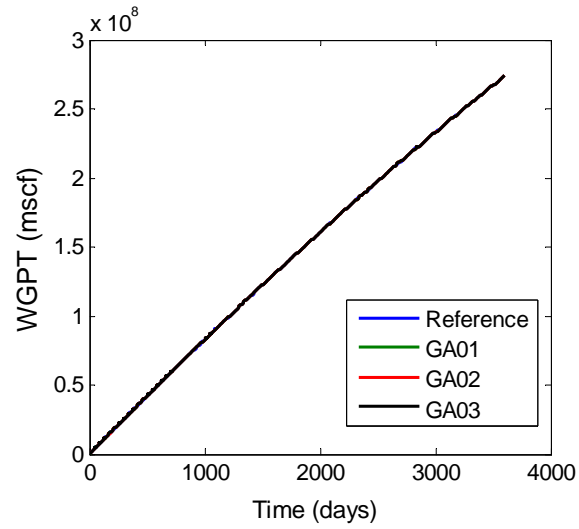
(a) Accumulated gas production with time.
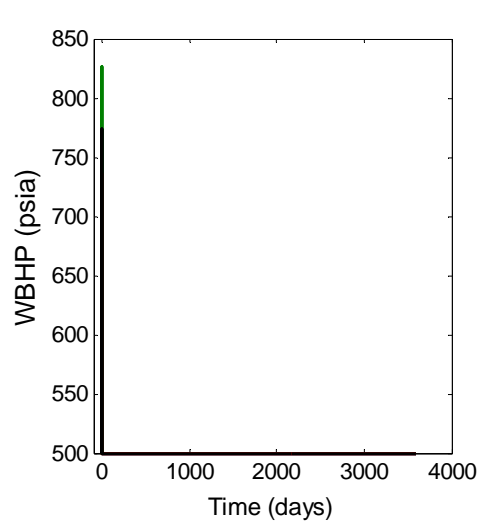
(b) Bottom hole pressure history.
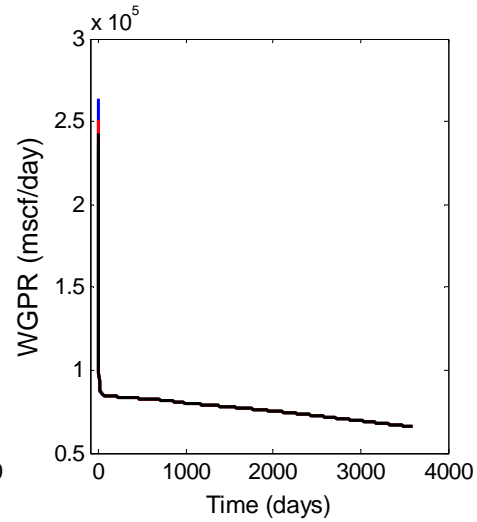
(c) Gas production history

Figure 5.26: History profiles of (a) The accumulated gas production ($WGPT$ (b) Well bottom hole pressure ($WBHP$) and (c) Gas production rate ($WGPR$ for the top three $WGPR$ GA optimized scenarios.
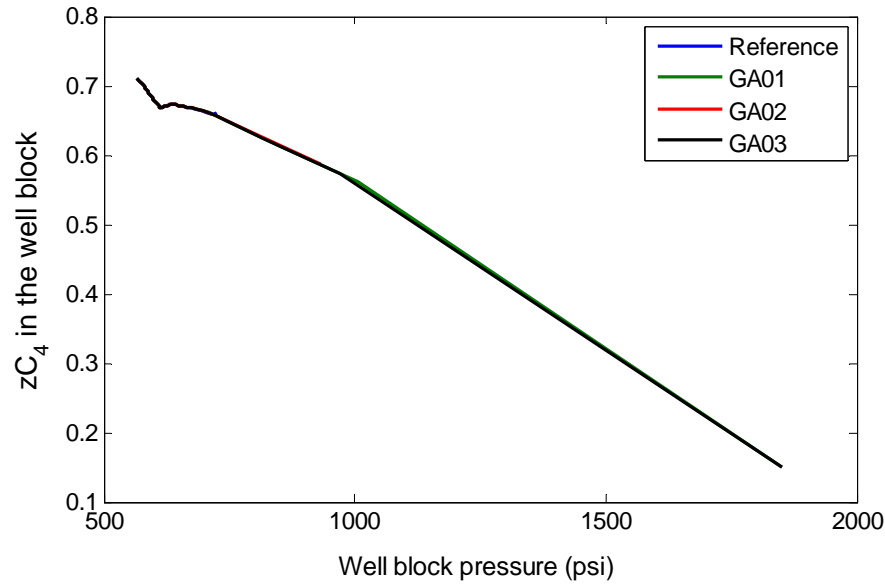
(a) Overall C$_4$ mole fraction in the well block vs. well block pressure.
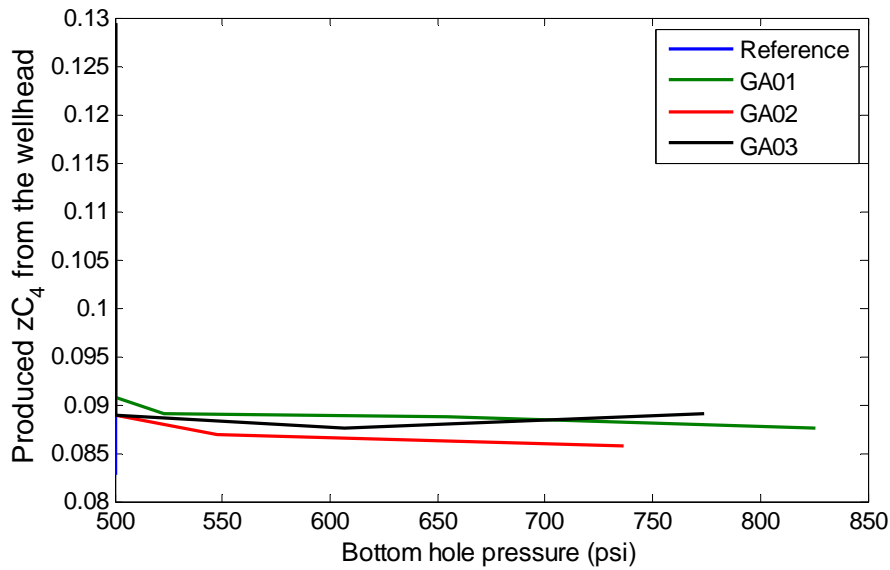
(b) Flowing C$_4$ mole fraction vs. well bottom hole pressure (BHP).

Figure 5.27: Overall butane mole fraction z_{C_4} profiles. (a) Overall butane mole fraction Bz_{C_4} profiles in the well block $vs.$ the well block pressure. (a) Overall butane mole fraction Wz_{C_4} profiles in the producing fluid $vs.$ BHP for the top three $WGPR$ GA optimized scenarios.
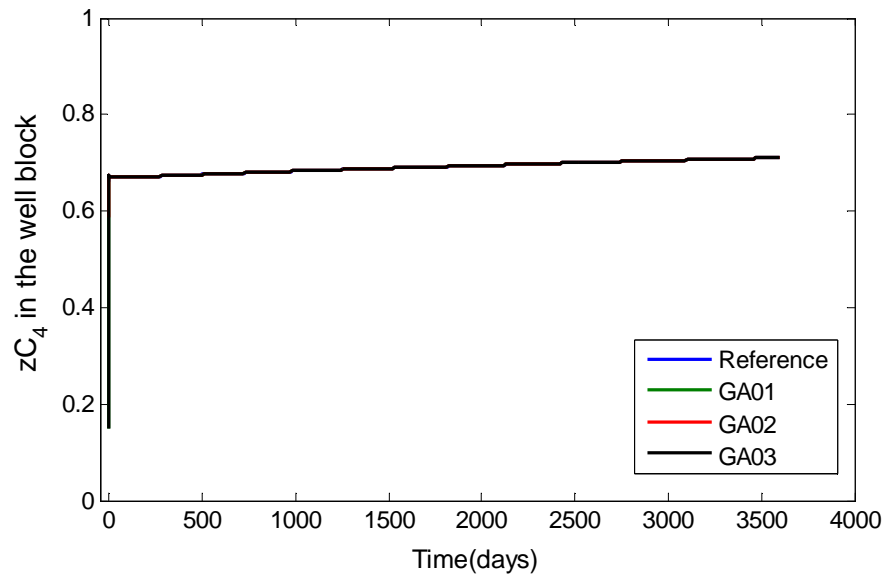
(a) Overall C$_4$ mole fraction in the well block vs. time.
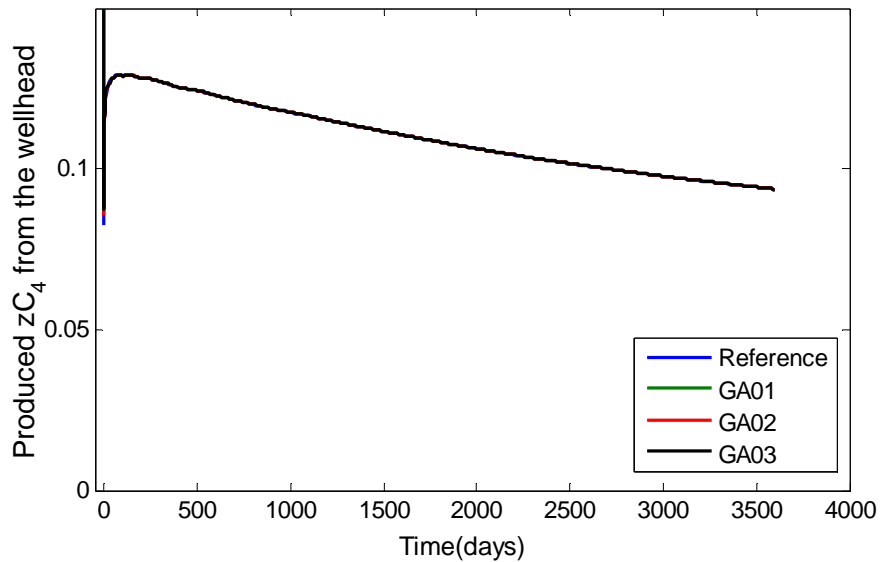
(b) Flowing C$_4$ mole fraction vs. time.

Figure 5.28: Overall butane mole fraction z_{C_4} history profiles. (a) History of the overall butane mole fraction Bz_{C_4} in the well block. (a) History of the overall butane mole fraction Wz_{C_4} profiles in the producing fluid for the top three $WGPR$ GA optimized scenarios.

especially the heavier component of the fluid, around the well during condensate dropout was analyzed. Key parameters that influence the compositional behavior were also discussed in detail. The theoretical models provide tools to better understand the momentary compositional variation in the reservoir.

In the last two sections, compositional simulations of binary and multicomponent gas-condensate systems were performed to investigate how the producing strategies influence the total gas production and compositional variation in both the well block and the well-head flow. Then in the following section, GA algorithm was applied to confirm and generalize the optimal producing schemes observed in the previous simulation.

Chapter 6

Conclusions and Discussions

This chapter consists of two parts. In the first section, general conclusions are drawn from the work performed on experimental, theoretical and simulation studies for gas-condensate flow in porous media with emphasis on composition behavior. In the second section, we discuss possible improvements of the current work.

6.1 General Conclusions

Compositional variation behavior in the reservoir was studied through experimental, theoretical and numerical simulation work. Optimal producing schemes were suggested for both gas production and also for condensate recovery. More specific conclusions are summarized in the following sections.

6.1.1 Theoretical Compositional Variation Models

General mathematical models were established to describe problems of dynamic condensate banking in both one-dimensional linear flow and three-dimensional radial flow in the porous media, with the effect of interfacial tension. The theoretical models provide us with an opportunity to isolate and investigate certain parameters that influence the compositional variation of the heavy components with time in the near-well region during depletion. The effects of relative permeability, fluid type and

127

pressure on condensate banking were discussed. The primary conclusions from the theoretical work can be summarized as follows:

- Both relative permeability and absolute permeability have effects on condensate banking behavior through the influence of the mobility term. Relative permeability models adjusted with the effect of interfacial tension may be more appropriate for gas-condensate modeling. The rate of the change in heavy components is higher for low permeability gas-condensate systems with greater pressure gradient.

- The total molar concentration of heavy components around the well increases as the flowing bottom hole pressure falls below the dew-point pressure. The rate of change in heavy components is higher for rich gas-condensate than for lean gas-condensate for a given reservoir.

- Reservoir pressure has significant effects on compositional variation behavior. In regions far away from the well, where pressure gradient is small, the total molar concentration of heavy components increases as the reservoir pressure drops below the dewpoint pressure. The heavy component deposits faster in low pressure regions than in high pressure regions. For a well producing at a constant bottom hole flowing pressure, the change of the composition of heavy components depends highly on pressure. The total molar concentration of heavy components increases around the well when the flowing pressure is above some pressure values, and then could decrease as pressure further drops down if vaporization takes effect in the reservoir.

6.1.2   Experimental Study of Gas-Condensate Flow in a Core

An experimental apparatus was designed and built to allow in-situ measurements of the real time pressure and composition sampling of the flowing fluid along the core. This coreholder can be used to perform constant pressure-drop core flooding experiment and the isolated coreholder can be taken to the x-ray CT room for saturation measurements.

Conclusions on the experimental work can be summarized as follows:

- In gas-condensate flow, local composition changes due to the influence of relative permeability effects even in the constant pressure-drop flow case. The composition of the flowing fluid had slight or no change in a flow with constant pressure drop.

- The reservoir fluid would not vaporize as suggested by the CVD experiment in the PVT cell due to the local composition variation.

- Repressurizing may not be a good strategy to remove the liquid accumulation in the reservoir.

- The condensate drop-out will hinder the flow capability due to relative permeability effects.

6.1.3 Numerical Simulation Study of Gas-Condensate Flow

Compositional simulations of binary and multicomponent gas-condensate systems were performed to investigate how the producing strategies influence the total gas production and compositional variation in both the well block and the well-head flow. GA algorithm was also performed to confirm and generalize the optimal producing schemes observed in simulation work. Observations on the simulation work are as follows:

- Composition and condensate saturation change significantly as a function of producing sequence. The higher the BHP, the less the condensate banking and a smaller amount of heavy-component is trapped in the reservoir. The lower the producing rate, the lower the amount of heavy-component left in the reservoir.

- Gas productivity can be maximized with a proper producing strategy. The total gas production can be increased by lowering the BHP or optimizing the producing rate.

- Productivity loss can be reduced by optimizing the producing sequence.

6.2   Possible Improvements and Future Work

As a number of assumptions and simplifications have been made in order to make the attempt to solve problems in the experimental setup presented earlier in this study. Other than the intrinsic restrictions of the equipment, improvements can still be made to the following aspects to better characterize the gas-condensate flow behavior in the reservoir.

First, composition samples from the core flow represent only the flowing fluid. In this study, the flowing fluid happens to have slight or no change in the composition. An immediate improvement would be a more careful design of non-constant pressure drop core-flooding or other forms of core-flooding that allow changes in the flowing fluid. The difficulties may come from identifying the sampling pressure correctly as the pressure keeps changing in non-constant pressure drop flow.

Second, the change in the total molar concentration of components in the core was investigated by comparing the original fluid with the fluid collected by the natural discharge into a receiver cylinder. The sample from the receiver cylinder is, therefore, an average of the molar concentration of fluids in the core. Due to the fact that some liquid is still stuck in the reservoir, and may not vaporize and flow out of the core without external force, the discharged fluid sample has lower heavy component concentration. A better way to measure the in-situ fluid composition in the core is desirable.

Third, the current saturation measurements were taken on the isolated core. An improvement on the tubing systems to allow the concurrent saturation and flow measurements is favored.

Finally, the current experiment was conducted at room temperature. The Joule-Thompson cooling effect was remedied in the tubing flow by applying heat tapes. The temperature variation in the core, however, has not been investigated. Temperature variation in the core would affect the flow on sampling. An improvement would be a real-time constant temperature environment for the experiment.

Appendix A

Core Scale Simulation Input File

```
-- ====================================================
--Study: Gas Condensate Core Flooding Test
--Author: Chunmei Shi
--Simulator: E300(2005a)
-- ====================================================
--Constant Pressure Drop Flow
```

—–Berea Sandstone with Length=27.4 *cm* and Diameter=5.06 *cm*.

```
-- ====================================================
RUNSPEC
-- ====================================================
OIL GAS
FULLIMP
WELLDIMS
10 50 3 3 5 10 5 4 3 0 /
DIMENS 51 1 1 /
NSTACK 50 /
ISGAS
--Units
LAB
--Number of components: implies compositional run COMPS
```

2 /

MISCIBLE

/

FMTOUT

UNIFOUT

−− ==

GRID

−− ==

INIT

DX

51∗0.51837 /

DY

51∗4.48 /

DZ

51∗4.48 /

−− Porosity and permeability

− − − (Rock)

BOX

− − − IX1−IX2 JY1−JY2 KZ1−KZ2

1 51 1 1 1 1 /

INCLUDE ′Perm.txt′/

ENDBOX

− − − TOP Specification

− − − IX1-IX2 JY1-JY2 KZ1-KZ1

−− 1 1 1 1 1 1 /

TOPS

51∗1 /

ENDBOX

−− ==

PROPS

−− ==

−− Properties section: PVT data

EOS

PR /

−− Names of Components

CNAMES

C1

nC4

/

−− Miscibility exponent

MISCEXP

0.000000001 /

−− Component Critical Temperatures (K)

TCRIT

190.5611111

425.2

/

−− Component Critical Pressures (atm)

PCRIT

45.44

37.46953

/

−−Component Critical Volumes($m^3/kg-mole$)

−− set by user

VCRIT

0.098

0.255

/

−− Component acentric factor

ACF

0.013

0.201

```
/
−−−Peneleux Correction (Shift parameters)
SSHIFT
0.
0.
/
−− Component Molecular Weight g/mol
MW
16.04
58.12
/
−− Binary interaction parameters
BIC
0.0
/
STCOND
15.0
1.0
/
−− Reservoir temperature: Deg C / K
RTEMP
−−20 / 293.15K
20 / 293.15K
−− Rock and fluid properties
ROCK
132.7 0.00000000001 /
−−−Relative Permeability Functions
INCLUDE KrgoGC2.dat
/
−−−Miscibility surface tension reference
MISCSTR
```

12.3048 /

/

−−Surface tension with respect to pressure

STVP

300 12.3048

400 11.1124

500 9.9551

600 8.837

700 7.7623

800 6.7356

900 5.7616

1000 4.8454

1100 3.9918

1200 3.2063

1300 2.4941

1400 1.8605

1500 1.311

1600 0.8507

1700 0.4848

1800 0.2181

1850 0.1234

1900 0.0552

1925 0.0311

1950 0.0139

1975 0.0035 /

/

−−Specify miscibility variation with surface tension

FVST

0.0035 0.441977

0.0139 0.507334

0.0311 0.549881

0.0552 0.582353

0.1234 0.631138

0.2181 0.668126

0.4848 0.723684

0.8507 0.765544

1.311 0.799379

1.8605 0.827857

2.4941 0.852479

3.2063 0.874164

3.9918 0.893531

4.8454 0.911015

5.7616 0.92693

6.7356 0.941521

7.7623 0.954974

8.837 0.967438

9.9551 0.979032

11.1124 0.989859

12.3048 1.0 /

/

—— ===

SOLUTION

—— ===

PRESSURE

——Pressure (atm)

51*132.7 /

SGAS

1.0 50*1.0 /

XMF

51*0.85 51*0.15 /

YMF

51*0.85 51*0.15 /

```
-- ==================================================
SUMMARY
-- ==================================================
RUNSUM
RPTONLY
---Output Well properties for the producer
INCLUDE 'WOUTPUT_BINARY.txt'/
-- Output grid properties for specified grid blocks
INCLUDE 'BPRES.txt'/
INCLUDE 'BSOIL.txt'/
INCLUDE 'BXMF1.txt'/
INCLUDE 'BXMF2.txt'/
INCLUDE 'BYMF1.txt'/
INCLUDE 'BYMF2.txt'/
INCLUDE 'BBOIL.txt'/
INCLUDE 'BBGAS.txt'/
INCLUDE 'BMLSC2.txt'/
INCLUDE 'BMLST.txt'/
INCLUDE 'BVMF.txt'/
/
-- ==================================================
SCHEDULE
-- ==================================================
WELLSPEC
INJ1 G1 1 1 3* /
PROD1 G2 50 1 3* /
/
WELLCOMP
INJ1 1 1 1 1 1* 0.15875 5* /
PROD1 50 1 1 1 1* 0.15875 5* /
/
```

−− Specify compositions of inj gas stream

WELLSTRE

LEANGAS 0.85 0.15 /

/

WCONINJE INJ1 GAS AUTO BHP 2∗ 133.3701 /

/

WINJGAS

INJ1 STREAM LEANGAS/

/

WCONPROD

PROD1 OPEN BHP 5∗ 68.72642 /

/

TUNING

.000277 0.05 0.0000277 /

/

TSTEP

60∗0.0166667 60∗0.5 /

END

Appendix B

Field Scale MultiComponent Simulation Input File

```
-- ================================================
--Study: Gas Condensate Flow Behavior Study
--by Chunmei Shi on Oct 1st, 2007
--2 components; Peng-Robinson EoS with correction
--Grid dimensions 36x1x4, RADIAL
--Fully implicit solution method; FIELD units; 3-stage separator
--Simulator: E300(2005a)
-- ================================================
RUNSPEC
-- ================================================
RADIAL
--Request the FIELD unit set
FIELD
--Water is present
WATER
--FULLIMP solution method
FULLIMP
--Nine components in study ( plus water )
```

COMPS

9 /

−−−Peng-Robinson equation of state to be used

EOS

PR /

DIMENS

36 1 4 /

TABDIMS

1 1 40 40 /

−−−Is a gas condensate study

ISGAS

MULTSAVE

0 /

−− ==

GRID

−− ==

−−−Basic grid block sizes

INRAD

0.3/

/

DR

0.630957 0.794328 1.000000 1.258925 1.584893 1.995262 2.511886 3.162278 3.981072

5.011872 6.309572 7.943282 10.00000 12.58925 15.84893 19.95262 25.11886 31.62278

39.81072 50.11872 63.09573 79.43282 100.0000 125.8925 158.4893 199.5262 251.1886

316.2278 398.1072 501.1872 630.9573 794.3282 1000.000 1258.925 1584.893 1995.262

0.630957 0.794328 1.000000 1.258925 1.584893 1.995262 2.511886 3.162278 3.981072

5.011872 6.309572 7.943282 10.00000 12.58925 15.84893 19.95262 25.11886 31.62278

39.81072 50.11872 63.09573 79.43282 100.0000 125.8925 158.4893 199.5262 251.1886

316.2278 398.1072 501.1872 630.9573 794.3282 1000.000 1258.925 1584.893 1995.262

0.630957 0.794328 1.000000 1.258925 1.584893 1.995262 2.511886 3.162278 3.981072

5.011872 6.309572 7.943282 10.00000 12.58925 15.84893 19.95262 25.11886 31.62278

39.81072 50.11872 63.09573 79.43282 100.0000 125.8925 158.4893 199.5262 251.1886
316.2278 398.1072 501.1872 630.9573 794.3282 1000.000 1258.925 1584.893 1995.262
0.630957 0.794328 1.000000 1.258925 1.584893 1.995262 2.511886 3.162278 3.981072
5.011872 6.309572 7.943282 10.00000 12.58925 15.84893 19.95262 25.11886 31.62278
39.81072 50.11872 63.09573 79.43282 100.0000 125.8925 158.4893 199.5262 251.1886
316.2278 398.1072 501.1872 630.9573 794.3282 1000.000 1258.925 1584.893 1995.262/
/
PORO
144*0.13 /
PERMX
36*13 36*4 36*2 36*15 /
PERMY
36*13 36*4 36*2 36*15 /
PERMZ
36*13 36*4 36*2 36*15 /
EQUALS
DTHETA 360 /
DZ 30 1 36 1 1 1 2 /
DZ 50 1 36 1 1 3 4 /
TOPS 7340 1 36 1 1 1 1 /
TOPS 7370 1 36 1 1 2 2 /
TOPS 7400 1 36 1 1 3 3 /
TOPS 7450 1 36 1 1 4 4 /
/
−− ===
PROPS
−− ===
NCOMPS
9 /
EOS
PR /

−− Peng-Robinson correction

PRCORR

−− Standard temperature and pressure in Deg F and PSIA

STCOND

60.0 14.7 /

−− Component names

CNAMES

CO2 N2 C1 C2 C3 C4-6 C7+1 C7+2 C7+3 /

−− Critical temperatures Deg R

TCRIT

548.46000 227.16000 343.08000 549.77400 665.64000 806.54054 838.11282 1058.03863

1291.89071 /

−− Critical pressures PSIA

PCRIT

1071.33111 492.31265 667.78170 708.34238 618.69739 514.92549 410.74956 247.56341

160.41589 /

−− Critical Z-factors

ZCRIT

.27408 .29115 .28473 .28463 .27748 .27640 .26120 .22706 .20137 /

−− Acentric factors

ACF

.22500 .04000 .01300 .09860 .15240 .21575 .31230 .55670 .91692 /

−− Molecular Weights

MW

44.01000 28.01300 16.04300 30.07000 44.09700 66.86942 107.77943 198.56203 335.19790

/

−− $Omega_A$ values

OMEGAA

.4572355 .4572355 .5340210 .4572355 .4572355 .4572355 .6373344 .6373344 .6373344

/

−− $Omega_B$ values

OMEGAB

.0777961 .0777961 .0777961 .0777961 .0777961 .0777961 .0872878 .0872878 .0872878

/

−− Default fluid sample composition

−− composition not varying with depth

ZMFVD

1.00000 .01210 .01940 .65990 .08690 .05910 .09670 .04745 .01515 .00330

10000.00000 .01210 .01940 .65990 .08690 .05910 .09670 .04745 .01515 .00330 /

−− Boiling point temperatures Deg R

TBOIL

350.46000 139.32000 201.06000 332.10000 415.98000 523.33222 689.67140 958.31604

1270.40061 /

−− Reference temperatures Deg R

TREF

527.40000 140.58000 201.06000 329.40000 415.80000 526.05233 519.67000 519.67000

519.67000 /

−− Reference densities LB/FT^3

DREF

48.50653 50.19209 26.53189 34.21053 36.33308 37.87047 45.60035 50.88507 55.89861

/

−− Parachors (Dynes/cm)

PARACHOR

78.00000 41.00000 77.00000 108.00000 150.30000 213.52089 331.78241 516.45301 853.48860

/

−− Binary Interaction Coefficients

BIC

.0200

.1000 .0360

.1300 .0500 .000000

.1350 .0800 .000000 .000

.1277 .1002 .092810 .000 .000

.1000 .1000 .130663 .006 .006 .0
.1000 .1000 .130663 .006 .006 .0 .0
.1000 .1000 .130663 .006 .006 .0 .0 .0 /
—— Reservoir temperature in Deg F
RTEMP 200.0 /
——Water saturation functions
SWFN
0.16 0 50
0.20 0.002 32
0.24 0.010 21
0.28 0.020 15.5
0.32 0.033 12.0
0.36 0.049 9.2
0.40 0.066 7.0
0.44 0.090 5.3
0.48 0.119 4.2
0.52 0.150 3.4
0.56 0.186 2.7
0.60 0.227 2.1
0.64 0.277 1.7
0.68 0.330 1.3
0.72 0.390 1.0
0.76 0.462 0.7
0.8 0.540 0.5
0.84 0.620 0.4
0.88 0.710 0.3
0.92 0.800 0.2
0.96 0.900 0.1
1.00 1.000 0.0 /
——Gas saturation functions
SGFN

0.00 0.000 0.0

0.04 0.038 0.0

0.08 0.070 0.0

0.12 0.106 0.0

0.16 0.141 0.0

0.20 0.177 0.0

0.24 0.217 0.0

0.28 0.260 0.0

0.32 0.300 0.0

0.36 0.349 0.0

0.40 0.400 0.0

0.44 0.450 0.0

0.48 0.505 0.0

0.52 0.562 0.0

0.56 0.620 0.0

0.60 0.680 0.0

0.64 0.740 0.0

0.68 0.740 0.0

0.72 0.740 0.0

0.76 0.740 0.0

0.80 0.740 0.0

0.84 0.740 0.0 /

−−Oil saturation functions

SOF3

0.00 0.000 0.000

0.04 0.000 0.000

0.08 0.000 0.000

0.12 0.000 0.000

0.16 0.000 0.000

0.20 0.000 0.000

0.24 0.000 0.000

0.28 0.000 0.000

0.32 0.000 0.000

0.36 0.000 0.000

0.40 0.000 0.000

0.44 0.000 0.000

0.48 0.005 0.005

0.52 0.012 0.012

0.56 0.024 0.024

0.60 0.040 0.040

0.68 0.082 0.082

0.72 0.112 0.112

0.76 0.150 0.150

0.80 0.196 0.196

0.84 0.256 0.256 /

−−Rock and water pressure data

ROCK

3550 0.000004 /

PVTW

3550 1.0 0.000003 0.31 0.0 /

−−Surface density of water

DENSITY

1* 63.0 1* /

−− ===

SOLUTION

−− ===

−−Equilibration data - initial pressure 3500 psi at 7500

EQUIL

7500 3550 7500 0 7500 0 1 1 0 /

RPTRST

PRESSURE SOIL YMF VOIL /

RPTSOL

PRESSURE SOIL /

FIELDSEP

1 80 815 /

2 80 65 /

3 60 14.7 /

/

−− ==

SUMMARY

−− ==

−−ALL

RUNSUM

RPTONLY

−−Output Well properties for the producer

INCLUDE ′WOUTPUT_MULlTICOMP.txt′/

−−saturation and composition history for layer 4

INCLUDE ′BSOIL.txt′/

INCLUDE ′BXMF.txt′/

INCLUDE ′BYMF.txt′/

BVMF

1 1 4 /

/

−− ==

SCHEDULE

−− ==

−−Define separator ; third stage represents stock tank

SEPCOND

SEP FIELD 1 80 815 /

SEP FIELD 2 80 65 /

SEP FIELD 3 60 14.7 /

/

−−Define injection and production wells

WELSPECS

–I FIELD 1 1 7330 GAS/

P FIELD 1 1 7400 GAS/

/

WSEPCOND

P SEP /

/

COMPDAT

−−I 1 1 1 2 1∗ 1 /

P 1 1 3 4 1∗ 1 /

/

−−Well P set to target gas rate of 10000, with min bhp of 500 psi

WCONPROD

P OPEN GRAT 1∗ 1∗ 10000 2∗ 500 /

/

TSCRIT

0.001 0.00001 1 /

TSTEP

0.00002 /

/

TSTEP

365 /

/

END

Appendix C

Field Scale Binary Simulation Input File

```
−− ===============================================
−−Study: Gas Condensate Flow Behavior Study
−−by Chunmei Shi on Oct 1st, 2007
−−9 components; Peng-Robinson EoS with correction
−−Grid dimensions 36x1x4, RADIAL
−−Fully implicit solution method; FIELD units; 3-stage separator
−−Simulator: E300(2005a)
−− ===============================================
RUNSPEC
−− ===============================================
RADIAL
−−Request the FIELD unit set
FIELD
−−Water is present
WATER
−−FULLIMP solution method
FULLIMP
−−Two components in study ( plus water )
```

COMPS

2 /

−−−Peng-Robinson equation of state to be used

EOS

PR /

DIMENS

36 1 4 /

TABDIMS

1 1 40 40 /

−−−Is a gas condensate study

ISGAS

MULTSAVE

0 /

−− ===

GRID

−− ===

−−−Basic grid block sizes

INRAD

0.3/

/

DR

0.630957 0.794328 1.000000 1.258925 1.584893 1.995262 2.511886 3.162278 3.981072

5.011872 6.309572 7.943282 10.00000 12.58925 15.84893 19.95262 25.11886 31.62278

39.81072 50.11872 63.09573 79.43282 100.0000 125.8925 158.4893 199.5262 251.1886

316.2278 398.1072 501.1872 630.9573 794.3282 1000.000 1258.925 1584.893 1995.262

0.630957 0.794328 1.000000 1.258925 1.584893 1.995262 2.511886 3.162278 3.981072

5.011872 6.309572 7.943282 10.00000 12.58925 15.84893 19.95262 25.11886 31.62278

39.81072 50.11872 63.09573 79.43282 100.0000 125.8925 158.4893 199.5262 251.1886

316.2278 398.1072 501.1872 630.9573 794.3282 1000.000 1258.925 1584.893 1995.262

0.630957 0.794328 1.000000 1.258925 1.584893 1.995262 2.511886 3.162278 3.981072

5.011872 6.309572 7.943282 10.00000 12.58925 15.84893 19.95262 25.11886 31.62278

39.81072 50.11872 63.09573 79.43282 100.0000 125.8925 158.4893 199.5262 251.1886
316.2278 398.1072 501.1872 630.9573 794.3282 1000.000 1258.925 1584.893 1995.262
0.630957 0.794328 1.000000 1.258925 1.584893 1.995262 2.511886 3.162278 3.981072
5.011872 6.309572 7.943282 10.00000 12.58925 15.84893 19.95262 25.11886 31.62278
39.81072 50.11872 63.09573 79.43282 100.0000 125.8925 158.4893 199.5262 251.1886
316.2278 398.1072 501.1872 630.9573 794.3282 1000.000 1258.925 1584.893 1995.262/
/
PORO
144*0.13 /
PERMX
36*13 36*4 36*2 36*15 /
PERMY
36*13 36*4 36*2 36*15 /
PERMZ
36*13 36*4 36*2 36*15 /
EQUALS
DTHETA 360 /
DZ 30 1 36 1 1 1 2 /
DZ 50 1 36 1 1 3 4 /
TOPS 7340 1 36 1 1 1 1 /
TOPS 7370 1 36 1 1 2 2 /
TOPS 7400 1 36 1 1 3 3 /
TOPS 7450 1 36 1 1 4 4 /
/
−− ==
PROPS
−− ==
NCOMPS
2 /
EOS
PR /

−− Peng-Robinson correction

PRCORR

−− Standard temperature and pressure in Deg F and PSIA

STCOND

60.0 14.7 /

−− Component names

CNAMES

C1 C4 /

−− Critical temperatures Deg R

TCRIT

343.08000 755.1 /

−− Critical pressures PSIA

PCRIT

667.78170 543.45 /

−− Critical Z-factors

ZCRIT

.28473 0.27717 /

−− Acentric factors

ACF

.01300 0.1956 /

−− Molecular Weights

MW

16.04300 58.124 /

−− $Omega_A$ values

OMEGAA

.4572355 .4572355 /

−− $Omega_B$ values

OMEGAB

.0777961 .0777961 /

−− Default fluid sample composition

−− composition not varying with depth

ZMFVD

1.00000 0.8500 0.1500

10000.00000 0.8500 0.1500 /

−− Boiling point temperatures Deg R

TBOIL

200.88 484.02 /

−− Reference temperatures Deg R

TREF

201.06 527.4 /

−− Reference densities LB/FT^3

DREF

26.53189 35.69 /

−− Parachors (Dynes/cm)

PARACHOR

77.00000 187.2 /

−− Binary Interaction Coefficients

BIC

.0000

/

−− Reservoir temperature in Deg F

RTEMP 60.0 /

−−Water saturation functions

SWFN

0.16 0 50

0.20 0.002 32

0.24 0.010 21

0.28 0.020 15.5

0.32 0.033 12.0

0.36 0.049 9.2

0.40 0.066 7.0

0.44 0.090 5.3

0.48 0.119 4.2

0.52 0.150 3.4

0.56 0.186 2.7

0.60 0.227 2.1

0.64 0.277 1.7

0.68 0.330 1.3

0.72 0.390 1.0

0.76 0.462 0.7

0.8 0.540 0.5

0.84 0.620 0.4

0.88 0.710 0.3

0.92 0.800 0.2

0.96 0.900 0.1

1.00 1.000 0.0 /

−−Gas saturation functions

SGFN

0.00 0.000 0.0

0.04 0.038 0.0

0.08 0.070 0.0

0.12 0.106 0.0

0.16 0.141 0.0

0.20 0.177 0.0

0.24 0.217 0.0

0.28 0.260 0.0

0.32 0.300 0.0

0.36 0.349 0.0

0.40 0.400 0.0

0.44 0.450 0.0

0.48 0.505 0.0

0.52 0.562 0.0

0.56 0.620 0.0

0.60 0.680 0.0

0.64 0.740 0.0

0.68 0.740 0.0

0.72 0.740 0.0

0.76 0.740 0.0

0.80 0.740 0.0

0.84 0.740 0.0 /

−−−Oil saturation functions

SOF3

0.00 0.000 0.000

0.04 0.000 0.000

0.08 0.000 0.000

0.12 0.000 0.000

0.16 0.000 0.000

0.20 0.000 0.000

0.24 0.000 0.000

0.28 0.005 0.005

0.32 0.012 0.012

0.36 0.024 0.024

0.40 0.040 0.040

0.44 0.060 0.060

0.48 0.082 0.082

0.52 0.112 0.112

0.56 0.150 0.150

0.60 0.196 0.196

0.68 0.315 0.315

0.72 0.400 0.400

0.76 0.513 0.513

0.80 0.650 0.650

0.84 0.800 0.800 /

−−−Rock and water pressure data

ROCK

3550 0.000004 /

PVTW

3550 1.0 0.000003 0.31 0.0 /

−−−Surface density of water

DENSITY

1∗ 63.0 1∗ /

−− ==

SOLUTION

−− ==

−−−Equilibration data - initial pressure 3500 psi at 7500.

EQUIL

7500 3550 7500 0 7500 0 1 1 0 /

FIELDSEP

1 80 815 /

2 80 65 /

3 60 14.7 /

/

−− ==

SUMMARY

−− ==

−−−ALL

RUNSUM

−−−Field oil production rate and total, GOR and field pressure

WGPR

P /

/

WGPT

/

WBHP

P /

```
/
BPRES
1 1 4 /
/
WZMF
P 2 /
/
BVMF
1 1 4 /
/
BXMF
1 1 4 2 /
/
BYMF
1 1 4 2/
/
-- ================================================
SCHEDULE
-- ================================================
--Define separator ; third stage represents stock tank
SEPCOND
SEP FIELD 1 80 815 /
SEP FIELD 2 80 65 /
SEP FIELD 3 60 14.7 /
/
--Define injection and production wells
WELSPECS
-I FIELD 1 1 7330 GAS/
P FIELD 1 1 7400 GAS/
/
WSEPCOND
```

P SEP /
/
COMPDAT
−−I 1 1 1 2 1∗ 1 /
P 1 1 3 4 1∗ 1 /
/
−−Well P set to target gas rate of 10000, with min bhp of 500 psi
WCONPROD
P OPEN GRAT 1∗ 1∗ 10000 2∗ 500 /
/
TSCRIT
0.001 0.00002 1 /
TSTEP
0.00002 /
/
TSTEP
365 /
/
END

Nomenclatures

BHP = bottom-hole pressure

CO_2 = carbon dioxide

C_1 = methane

C_2 = ethane

C_3 = propane

iC_4 = i-butane

nC_4 = n-butane

iC_5 = i-pentane

nC_5 = n-pentane

C_6 = hexane

C_7 = heptane

C_8 = octane

C_9 = nonane

C_10^+ = decene and higher

CT_a = air phase CT number

CT_l = liquid phase CT number

CT_{ar} = CT number for air-saturated rock

CT_{lr} = CT number for liquid-saturated rock

CT_{gr} = CT number for gas-saturated rock

CT_{glr} = CT number for the rock saturated with the mixture of liquid and gas

CVD = Constant volume depletion

N_2 = nitrogen

Mw = molecular weight

p_c = critical pressure (psi or atm)

S_c = condensate saturation

S_{cc} = critical condensate saturation

S_g = gas saturation

T_c = critical temperature(^oC or ^oF)

$WGPT$ = well total gas production (mscf or scc)

$WBHP$ = well bottom hole pressure (psi or atm)

$WGPR$ = gas production rate for a single well (mscf/day)

ϕ = porosity

μ_g = the attenuation coefficients for the core fully saturated with gas

μ_l = the attenuation coefficients for the core fully saturated with liquid

μ_r = the attenuation coefficients for the rock matrix

Bibliography

Abel, W., Jackson, R., and Wattenbarger, R. (1970). "Simulation of a Partial Pressure Maintenance Gas Cycling Project with a Compositional Model, Carson Creek Field, Alberta". *JPT* January, pp 38–46.

Afidick, D., Kaczorowski, N., and Bette, S. (1994). "Production Performance of a Retrograde Gas: A Case Study of the Arun Field". In *SPE Asia Pacific Oil and Gas Conference*, Melbourne, Australia. SPE 28749.

Akin, S. and Kovscek, A. (2003). "Computed Tomography in Petroleum Engineering Research". *Geological Society* speical publications, pp 22–38.

Allen, F. and Roe, R. (1950). "Performance Characteristics of a Volumetric Condensate Reservoir". *Petroleum Transactions, AIME*, pp 83–90.

Aly, A., El-Banbi, A., Holditch, S., M.Wahdan, N.Salah, Aly, N., and Boerrigter, P. (2001). "Optimization of Gas Condensate Reservoir Development by Coupling Reservoir Modeling and Hydraulic Fracturing Design". In *SPE Middle East Oil Show and Conference*, Bahrain. SPE 68175.

Ayala, L., Ertekin, T., and Adewumi, M. (2007). "Study of Gas/Condensate Reservoir Exploitation Using Neurosimulation". *Petroleum Transactions, AIME* April.

Aziz, R. (1985). "Deliverability Projection Model for Overpressured Gas-Condensate Reservoirs". In *SPE Middle East Technical Conference and Exhibition*, Bahrain. SPE 13706.

Barnum, R., Brinkman, F., Richardson, T., and Spillette, A. (1995). "Gas Condensate Reservoir Behavior: Productivity and Recovery Reduction Due to Condensation". In *SPE Annual Technical Conference and Exhibition*, Dallas, TX. SPE 30767.

Bengherbia, M. and Tiab, D. (2002). "Gas-Condensate Well Performance Using Compositional Simulator: A Case Study". In *SPE Gas Technology Symposium*, Calgary, Canada. SPE 75531.

Bette, S., Hartman, K., and Heinemann, R. (1991). "Compositional modelling of interfacial tesion effects in miscible displacement processes". *Journal of Petroleum Science and Engineering*, pp 1–14.

Bittencourt, A. (1997). *"Optimizing Hydrocarbon Field Development Using a Genetic Algorithm Based Approach"*. Ph.D. thesis, Stanford University.

Clark, T. (1985). "The Application of a 2-D Compositional, Radial Model to Predict Single-Well Performance in a Rich Gas Condensate Reservoir". In *SPE Annual Technical Conference and Exhibition*, Las Vegas, NV. SPE 14413.

Coats, K. (1980). "An equation of state compositional model". *Journal of Petroleum Science and Engineering* October, pp 363–367.

Dempsey, B., Taki, H., and Druyff, J. (2001). "Case History of Hydraulic Fracture Optimization in Tight Gas Wells with Water Production in the Wind River Basin, Wyoming". In *SPE Production and Operations Symposium*, Oklahoma City, OK. SPE 67300.

Duggan, J. (1972). "The Anderson 'L'-an Abnormally Pressured Gas Reservoir in South Texas". *JPT* February, pp 132–138.

Engineer, R. (1985). "Cal Canal Field, California: Case History of a Tight and Abnormally Pressured Gas Condensate Reservoir". In *SPE 1985 California Regional Meeting*, Bakersfield, CA. SPE 13650.

Fevang, O. (1995). *"Gas Condensate Flow Behavoir and Sampling"*. Ph.D. thesis, University of Trondheim.

Fevang, O. and Whitson, C. (1996). "Modeling Gas-Condensate Well Deliverability". *SPE Reservoir Engineering*, pp 221–230.

Fussell, D. (1973). "Single-Well Performance Predictions for Gas Condensate Reservoirs". *JPT* July, pp 860–870.

Hartman, K. and Cullick, A. (1994). "Oil Recovery by Gas Displacement at Low Interfacial Tension". *Journal of Petroleum Science and Engineering*, pp 197–210.

Hinchman, S. and Barree, R. (1985). "Productivity Loss in Gas condensate Reservoirs". In *SPE Annual Technical Conference and Exhibition*, Las Vegas, NV. SPE 14203.

Holland, J. (1975). *"Adaptation in Natural and Artificial Systems"*. MIT Press, Cambridge, MA.

Hurst, W. and Leeser, R. (1962). "Aspects of Gas Deliverability". In *Economics and Valuation Symposium*, Dallas, TX. SPE 262.

Iverson, W. and Surdam, R. (1995). "Tight Gas Sand Production from the Almond Formation, Washakie Basin, Wyoming". In *SPE Rocky Mountain Regional/Low-Permeability Reservoirs Symposium*, Denver, CO. SPE 29559.

Kleinsteiber, S., Wendschlag, D., and Calvin, J. (1983). "A Study for Development of a Plan of Depletion in a Rich Gas Condensate Reservoir: Anschutz Ranch East Unit, Summit County, Utah, Uinta County, Wyoming". In *SPE Annual Technical Conference and Exhibition*, San Francisco, CA. SPE 12042.

Lee, S. (1989). "Capillary-Gravity Equilibria for Hydrocarbon Fluids in Porous Media". In *SPE Annual Technical Conference and Exhibition*, San Antonio, TX. SPE 19650-MS.

Lin, Z. and Finley, R. (1985). "Reservoir Engineering Properties and Production Characteristics of Selected Tight Gas Fields, Travis Peak Formation, East Texas Basin". In *SPE low Permeability Gas Reservoirs Symposium*, Denver, CO. SPE 13901.

McCain, W. (1990). *"The Properties of Petroleum Fluids"*. PennWell Books, Tulsa, OK, 2nd edition.

Moses, P. (1986). "Engineering Applications of Phase Behavoir of Crude Oil and Condensate Systems". *JPT* July, pp 715–725.

Parakh, S. (2007). *"Experimental Investigation of Enhanced Coal Bed Methane Recovery"*. Master's thesis, Stanford University, Stanford, CA.

Peaceman, D. (1996). "Calculation of Transmissibilities of Gridblocks Defined by Arbitrary Corner Point Geometry". In *SPE e-library (unpublished, but available from SPE e-library)*. SPE 37306.

Reid, R., Prausnitz, J., and Sherwood, T. (1977). *"The Properties of Gases and Liquids"*. McGraw-Hill, New York, 3rd edition.

Riemens, W. and de Jong, L. (1985). "Birba Field PVT Variations Along the Hydrocarbon Column and Confirmatory Field Tests". In *SPE Middle East Oil Technical Conference*, Bahrain. SPE 13719.

Roussennac, B. (2001). *"Gas Condensate Well Test Analysis"*. Master's thesis, Stanford University, Stanford, CA.

Schulte, A. (1980). "Compositional Variation within a Hydrocarbon Column Due to Gravity". In *SPE Annual Technical Conference and Exhibition*, Dallas, TX. SPE 9235.

Shi, C., Horne, R., and Li, K. (2006). "Optimizing the Productivity of Gas-Condensate Wells". In *SPE Annual Technical Conference and Exhibition*, San Antonio, TX. SPE 103255.

Vinegar, H. and Wellington, S. (1987). "Tomographic imaging of three-phase flow experiments". *Rev. Sci. Instrum.* January.

Vo, D., Jones, J., and Raghavan, R. (1989). "Performance Prediction for Gas Condensate Reservoirs". *SPE Formation Evaluation* December, pp 576–584.

Wheaton, R. and Zhang, H. (2000). "Condensate Banking Dynamics in Gas Condensate Fields: Compositional Changes and Condensate Accumulation Around Production Wells". In *SPE Annual Technical Conference and Exhibition*, Dallas, TX. SPE 62930.

Whitson, C. (2005). "Khuff Gas Condensate Development". In *International Petroleum Technology Conference*, Doha, Qatar. IPTC 10692.

Yuan, S., Ye, J., and Sun, Z. (2003). *"Theory and Practices in Gas-Condensate Reservoir Development"*. China Petroleum Industry Press, Beijing, China.

Zhou, Y., Wang, C., and Firor, R. (2003). "Analysis of Permanent Gases and Methane with the Agilent 6820 Gas Chromatograph". *Agilent Technologies, publication 5988-9260EN, www.agilent.com/chem.*